Author:
Jensen, Torsten T

Title:
The Crystallisation and Excitonic Luminescence of Molecular Crystals

The Crystallisation and Excitonic Luminescence of Molecular Crystals

Torsten Thomas Jensen

Supervisor: Dr Simon Hall

A thesis submitted to the University of Bristol in accordance with the requirements for award of the degree of Doctor of Philosophy in the Faculty of Science

Word count: Thirty thousand

Abstract

The optoelectronic properties of organic molecular crystals are dependent on the electronic properties of both the constituent molecules and the structure that the molecules adopt, which is in turn affected by the charge distribution across the molecule. Tailoring of these properties may then be utilised in the creation of devices such as transistors, LEDs and solar cells. In this thesis, three studies into the crystallisation and optical properties of organic molecular crystals are presented. The first study concerns the growth of the aromatic molecule bis(4-bromophenyl)fumaronitrile via physical vapour transport, which resulted in the crystallisation of a novel polymorph. This structure has weaker red-shifted fluorescence emission relative to the conventional form owing to π-stacking and molecular conformational differences and crystallises on higher temperature substrates, due to its greater thermodynamic stability over the conventional form. The second study elucidates the mystery as to why crystals of the polyaromatic hydrocarbon coronene grown in a laboratory and karpatite, a naturally forming mineral composed of crystalline coronene, fluoresce different colours when exposed to ultraviolet light. The differences are found to be due to the morphologies of each, with the nano-thick crystalline layers of karpatite preventing the formation of excited dimers and therefore resulting in emittance at lower wavelengths. The third study examines the crystallisation propensity of persulfurated coronene, a sulphur-decorated planar organic molecule, which was unable to be crystallised via physical vapour transport and solution-based growth methods, with electron diffraction tomography showing that no crystallinity exists within molecular aggregates down to the nanoscale. Extensive simulations on monomers, dimers and trimers of persulfurated coronene revealed that the homogeneous charge distribution across the molecule results in a strong preference for face-face over edge-face intermolecular interactions, rendering crystal structure formation unfeasible.

Dedication and Acknowledgements

The last four years working in Simon's group on this work have definitely been some of the best of my life so far, owing to everyone I've gotten to know over this period. Although it wasn't always smooth sailing, the people who I had the pleasure of working and surrounding myself with outside of work helped calm the waters greatly and kept me going until the very end. Firstly, to Simon: your enthusiasm and willingness to throw yourself at any scientific challenge or curiosity kept me engaged with the work throughout the project. Your outgoing, warm demeanour meant that I knew that I'd picked the right supervisor from our first meeting. Secondly, to everyone in the Complex Functional Materials Group, who have been an endless spring of jokes, intellectual discussion, support (academic or otherwise) and new ideas: Jason, Charlie, Vicky, Joe, Spayne, Julie, Emily, Will, Julia, Lui, Omar, Nicole and all the masters students who've worked with us (especially Barney). Thank you to Dr Hazel Sparkes and Dr Natalie Pridmore for your assistance with all things X-ray related. To the CDT-CMP and its staff who were incredibly friendly and helpful. To my parents, who inspired me down this path and helped to keep me going during the last stretch so I could see the thesis through to submission. Lastly to all my friends and bandmates, who have given moral support and good times throughout: Samir, Becky, Amy, Joe, Matt, Josh, Cat, Raph, Jess, Luke, Rick, Dom, Chris, Ben, Jake, Ollie, Francesco, Emma, Drake and many others who've been with me on this journey.

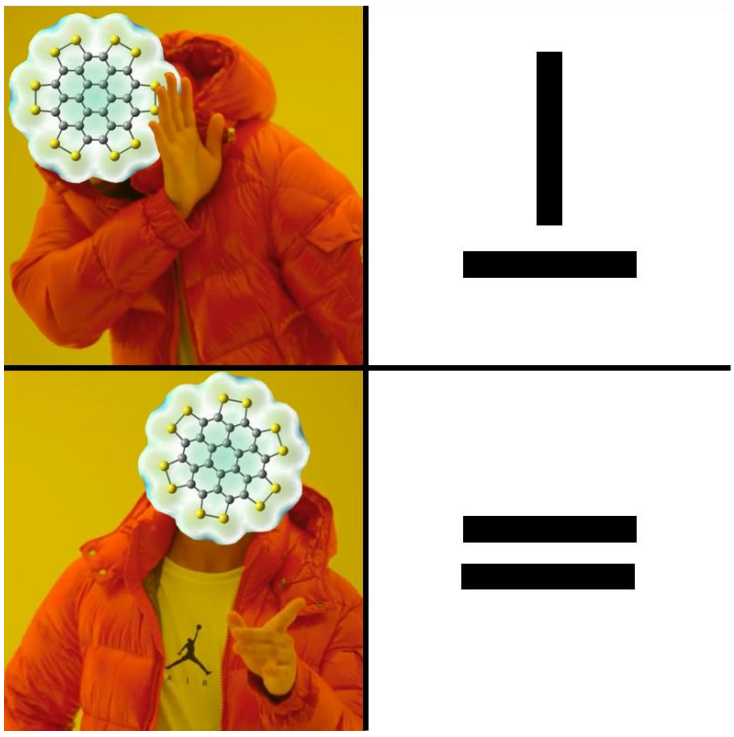

Figure 0.1: The graphical abstract for *An experimental and computational study into the crystallisation propensity of 2nd generation sulflower* (Jensen et al)

Author's Declaration

I declare that the work in this dissertation was carried out in accordance with the requirements of the University's Regulations and Code of Practice for Research Degree Programmes and that it has not been submitted for any other academic award. Except where indicated by specific reference in the text, the work is the candidate's own work. Work done in collaboration with, or with the assistance of, others, is indicated as such. Any views expressed in the dissertation are those of the author.

SIGNED: Torsten Thomas Jensen DATE: 17/03/20

1 Chapter 1: Introduction 1

1.1 Justification/ rationale 1

1.2 Organic Crystals 1

1.2.1 Definition 1

1.2.2 The Unit Cell 2

1.2.3 Intermolecular interactions 5

1.2.4 Nucleation and Growth 6

1.2.5 Polymorphism 8

1.2.6 Electronic Properties 11

1.3 Growth Methods 14

1.3.1 Solution Growth 14

1.3.2 Vapour Phase Growth 15

1.4 Characterisation 16

1.4.1 Structural characterisation 16

1.4.1.1 Single Crystal X-ray diffraction 17

1.4.1.2 Powder X-ray diffraction 17

1.4.1.3 3D Electron Diffraction Tomography 18

1.4.2 Optical characterisation 18

1.4.2.1 Ultraviolet-visible spectroscopy 18

1.4.2.2 Fluorometry 20

1.4.3 Differential Scanning Calorimetry 20

1.4.4 Scanning Electron Microscopy 21

1.5 Structure-Property Modelling 21

1.5.1 Density Functional Theory 22

1.5.1.1 Electrostatic potential surfaces 22

1.5.1.2 Interaction potentials 23

1.5.1.3 Crystal structure prediction 23

1.5.2 Force-Field Calculations 23

2 Chapter 2: Experimental and Computational Techniques 25

2.1 Sample Preparation 25

2.1.1 Synthesis of bis(4-bromophenyl)fumaronitrile 25

2.1.2 Extraction of karpatite from surrounding minerals 25

2.1.3 Solution Crystal Growth 25

2.1.3.1 Bis(4-bromophenyl)fumaronitrile 25

2.1.3.2 Coronene 25

2.1.3.3 Persulfurated coronene 25

2.1.4 Vapour Crystal Growth 26
2.1.4.1 Physical vapour transport growth of bis(4-bromophenyl)fumaronitrile 26
2.1.4.2 Sublimation recrystallisation of karpatite 26
2.1.4.3 Physical vapour transport growth of persulfurated coronene 26
2.2 Structural Characterisation 27
2.2.1 Powder X-ray Diffraction 27
2.2.1.1 Bis(4-bromophenyl)fumaronitrile 27
2.2.1.2 Coronene and karpatite 27
2.2.1.3 Persulfurated coronene 27
2.2.2 Single Crystal X-ray Diffraction 27
2.2.2.1 Bis(4-bromophenyl)fumaronitrile 27
2.3 Optical Characterisation 28
2.3.1 Ultraviolet-Visible Spectroscopy 28
2.3.1.1 Coronene and karpatite 28
2.3.2 Fluorescence Spectroscopy 28
2.3.2.1 Bis(4-bromophenyl)fumaronitrile 28
2.3.2.2 Coronene and karpatite 28
2.4 Differential Scanning Calorimetry 28
2.4.1 Bis(4-bromophenyl)fumaronitrile 28
2.4.2 Persulfurated coronene 28
2.5 Scanning electron microscopy 28
2.6 Computational Analysis 29
2.6.1 Lattice energy calculations of Bis(4-bromophenyl)fumaronitrile 29
2.6.2 ESP calculations on planar aromatic molecules 29
2.6.3 Crystal structure prediction 29
3 Chapter 3: Vapour Phase Growth of Bis(4-bromophenyl)fumaronitrile and Polymorphism 30
3.1 Introduction 30
3.1.1 Bis(4-bromophenyl)fumaronitrile 31
3.2 Results and Discussion 32
3.2.1 A new polymorph of Bis(4-bromophenyl)fumaronitrile 32
3.2.2 Crystal morphology 40
3.2.3 Polymorphism and Fluorescence 41
3.2.4 Physical Vapour Transport and Polymorphism 43
3.3 Summary and Impact 45

4 Chapter 4: The Nanostructural origin of Fluorescence in Karpatite 47

4.1 Introduction 47

4.1.1 Coronene 48

4.1.2 Karpatite 50

4.2 Composition and morphology of karpatite and lab-grown coronene crystals 51

4.2.1 X-ray diffraction and crystal structure 51

4.2.2 Scanning electron microscopy and micro-morphology 52

4.3 Optical properties 53

4.3.1 Absorption and fluorescence of karpatite and lab-grown coronene crystals 53

4.3.2 Recrystallisation of karpatite 54

4.3.3 Theories to the origins of fluorescence 56

4.4 Summary and Impact 59

5 Chapter 5: An Experimental and Computational Study into the Crystallisation Propensity of 2nd Generation Sulflower 60

5.1 Introduction 60

5.1.1 Planar Aromatic Molecules 60

5.1.2 Aromaticity and Aromatic Molecules 62

5.1.3 Crystallisation of Planar Aromatic Molecules 63

5.1.4 Coronene and Functionalised Derivatives 67

5.1.5 Persulfurated Coronene 68

5.2 Experimental Results 69

5.2.1 Crystallisation attempts 69

5.2.2 3D Electron Diffraction Tomography 72

5.2.3 Differential Scanning Calorimetry 73

5.3 Computational Results 73

5.4 Summary and Impact 81

6 Chapter 6: Conclusions and Future Work 83

7 Bibliography 85

1 Chapter 1: Introduction

1.1 Justification/ rationale

Organic crystals have been studied extensively for their semiconducting properties which have led to them being used in a wide array of different electronic and optoelectronic devices including transistors, light emitting diodes, solar cells and lasers[1]. Such devices made using organic crystals provide valuable insight into the fundamental nature of the electronic properties of organic materials, due to the chemical purity and long-range order of crystals. This insight then aids in the development of amorphous thin film devices made from polymers or small molecules, which may supersede inorganics in certain applications including displays, photovoltaics and sensors in the future[2]. The molecular arrangement within crystals will greatly affect their optoelectronic properties, so an understanding of how to optimise these properties through tailoring of the crystal structure and how to produce such structures is imperative to the advancement of the field. The electronic structure of a molecule or a crystal formed of that molecule will determine the arrangement of molecules within the crystal lattice, charge transfer rates between molecules and the optical properties of the crystal.

In this thesis, studies into the crystallisation of the molecules bis(4-bromophenyl)fumaronitrile, coronene and persulfurated coronene are presented, and how the electronic structure either affects or is affected by the conditions under which crystals will form. The first study covers the growth of crystals of bis(4-bromophenyl)fumaronitrile from the gas phase, and how localised conditions within the growth apparatus will affect the structure that the crystal will adopt, resulting in the formation of crystals with differing luminescent properties. The second examines the differences in fluorescence between lab-grown crystals of the polyaromatic hydrocarbon coronene and karpatite, a naturally forming mineral composed of coronene crystals, with the difference found to be due to the micro-morphology of each. Finally, an experimental and computational study is performed on persulfurated coronene and explains how its electronic distribution prevents it from crystallising at all.

1.2 Organic Crystals

1.2.1 Definition

Crystalline matter is fundamentally an ordered state, defined by an individual unit which forms the building blocks of a lattice which extends to a theoretical infinite limit in all directions. Crystals stand in contrast to glasses which are entirely amorphous and have no local or long-range order at the atomic scale, and as a result possess markedly different physical properties. Whereas amorphous materials have visibly uneven surfaces and rounded edges (Unless directed toward particular shapes in formation), crystals naturally have well-defined flat

surfaces and sharp edges, which are a reflection of the parameters of the unit cell as the same order exists within them on any length scale. Crystals can provide a direct link between the microscopic and macroscopic, allowing properties of the bulk to be readily related to the constituents which form them. They have been considered by some to be "supermolecules" by some due to the continuous and directed bonding motifs that propagate through the entire structure[3].

Whereas crystals formed from ionic or covalent bonds are strongly bound and the bonds are highly directional, the molecules in organic crystals are bound by weaker dipoles which form due to the anisotropy and mobility of charge across conjugated molecular segments. These are the basis behind van der Waals forces which are less directionally dependent. This allows for a wide number of different potential crystal structures for even a single molecule and makes organic crystals more brittle and fragile than their ionic or covalently bonded counterparts. The properties of the organic crystal may be tailored by altering the chemical structure of its constituent molecule or molecules. For example, their fluorescence emission energy will decrease as the length of the conjugated region of the molecule is increased[4].

1.2.2 The Unit Cell

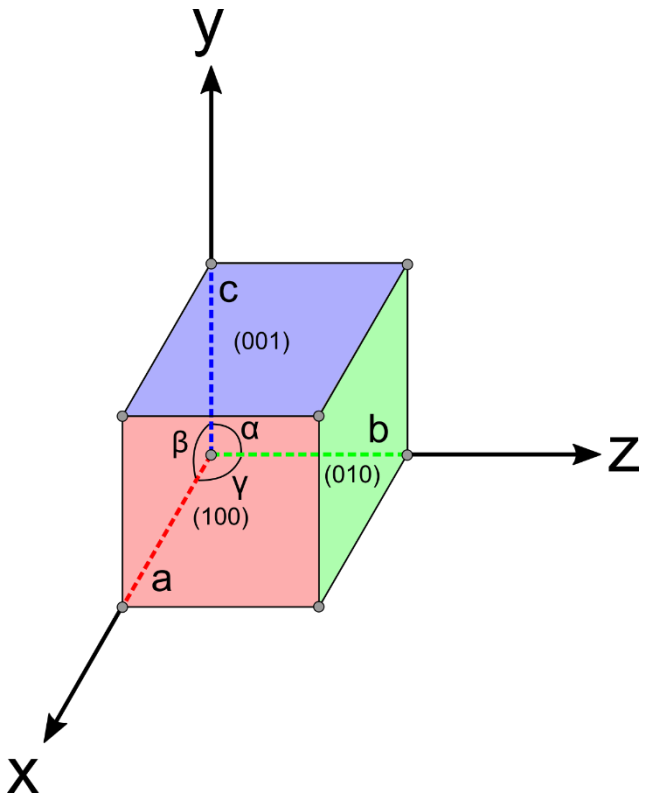

Figure 1.1: Schematic of a crystal unit cell and associated parameters, with faces labelled with the Miller indices of the corresponding crystal plane.

The unit cell is the smallest repeating segment of the crystal which can be used to build the entire structure and may be composed of one or more similar or distinct molecules, atoms or ions. It is a parallelepiped which can be described in six parameters: *a*, *b* and *c* for the length of each side and α, β and γ for the angles between the *b*

and *c* axes, *a* and *c* axes and *a* and *b* axes respectively (figure 1.1). Unit cells are classified according to their symmetry and shape, denoted by the crystal system. Each crystal system has its own conditions on the unit cell parameters which define its shape (table 1.1)[5].

Crystal system	Cell lengths	Cell angles
Cubic	$a = b = c$	$\alpha = \beta = \gamma = 90°$
Tetragonal	$a = b \neq c$	$\alpha = \beta = \gamma = 90°$
Orthorhombic	$a \neq b \neq c$	$\alpha = \beta = \gamma = 90°$
Trigonal	$a = b = c$	$\alpha = \beta = \gamma \neq 90°$
Hexagonal	$a = b \neq c$	$\alpha = \beta = 90°, \gamma = 120°$
Monoclinic	$a \neq b \neq c$	$\alpha = \gamma = 90°, \beta \neq 90°$
Triclinic	$a \neq b \neq c$	$\alpha \neq \beta \neq \gamma$

Table 1.1: The seven crystal systems and their associated lattice parameter conditions

Their internal symmetry is further described by space groups which denote the reflections, inversions and translations of the smallest asymmetric unit necessary to build the entire unit cell. They have the format $Xabc$, where X is the centring of the unit cell, and a, b and c are symmetry operators relating to the a, b and c axes respectively. The centring defines the positions of lattice points in the unit cell: primitive (P) cells have lattice points only on the corners of the cell, body centred (I) cells have lattice points on the corners and one at the exact centre of the cell, face centred (F) have points on the corners with additional points at the centre of each face and base centred (C) have points on the corners with additional points in the centre of two parallel faces of the cell[6]. The effect of different operators that may be applied to the asymmetric unit along each axis are given in table 1.2.

Operator	Notation	Description
Identity	1	Nothing done to an object
Inversion	$\bar{1}$	Inversion through the origin
Rotation	2, 3, 4 or 6 allowed dependent on symmetry	Rotation about the axis
Screw axis	X_Y	Translation of Y/X Rotation of $360/X$
Rotary inversion	$\bar{2}, \bar{3}, \bar{4}, \bar{6}$	Rotation and inversion
Glide plane	a, b, c, n, d, e	Translation in one vector by half the axis length followed by reflection in another

Table 1.2: Space group operators and their effects on the smallest asymmetric unit

In the reduced space group notation, the identity operator is removed as it does not highlight any symmetry. By convention for monoclinic space groups, operators are applied principally to the *b*-axis. For example, the γ-

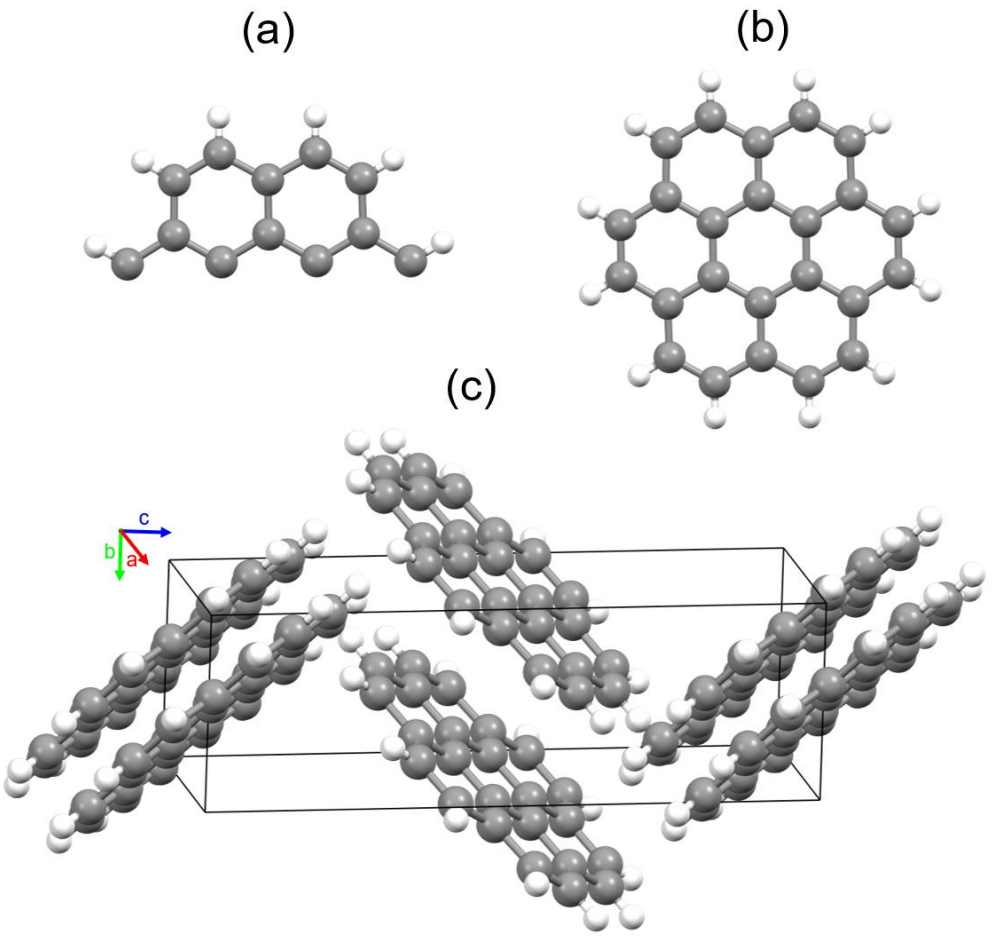

Figure 1.2: a) The asymmetric unit of coronene. Grey spheres are carbon, white spheres are hydrogen. b) The complete coronene molecule. c) The γ-herringbone crystal structure of coronene.

herringbone crystal structure of coronene (Figure 1.2c) has the reduced space group $P2_1/n$ (chapter 4). The P denotes that the unit cell is primitive. The 2_1 is a screw axis operator applied to the asymmetric unit (figure 1.2a), with a translation of $^1/_2$ of the *b*-axis length and a rotation about the *b*-axis of 180°. The n is a glide operator with a translation along the diagonal of the ac plane by half the total distance of this line in the unit cell, with a reflection in the *b*-axis. $P2_1/n$ is a centrosymmetric space group, meaning that the molecule will be reflected about its centre so the asymmetric unit will form the complete molecule in the unit cell (figure 1.2b). The identity operators on the *a* and *c*-axis are not present in the reduced notation. Alongside the reduced space group and unit cell parameters, the crystal system, the unit cell volume and number of complete molecules (Z) in the unit cell are typically provided when describing the unit cell.

Lattice planes bisect the unit cell in a manner that is equivalent in all unit cells of the crystal lattice if extended to the edges of the crystal. They are denoted by the Miller indices *h*, *k* and *l*, which define a set of coordinates *a*/*h*, *b*/*k* and *c*/*l* where the plane intercepts the unit cell axes, notated (*hkl*). If the value of the index is 0, the plane never intercepts the corresponding axis. For example, if a plane has the Miller indices (310), the plane will cross the unit cell boundaries at *a*/3 and *b*. If the plane crosses at a negative lattice value, the index will be written with a bar above the number, for example an intercept at -*a*/3 will be written as $\bar{3}^7$. Lattice planes and their

identification are important in X-ray diffraction (XRD) as the patterns generated from X-rays scattering off of each plane provide information on the interplanar spacing, which can then be used to either generate a complete structure solution of the unit cell, or provide a unique fingerprint which may be compared to the patterns generated from known unit cells for identification, depending on the technique used (section 1.4.1).

1.2.3 Intermolecular interactions

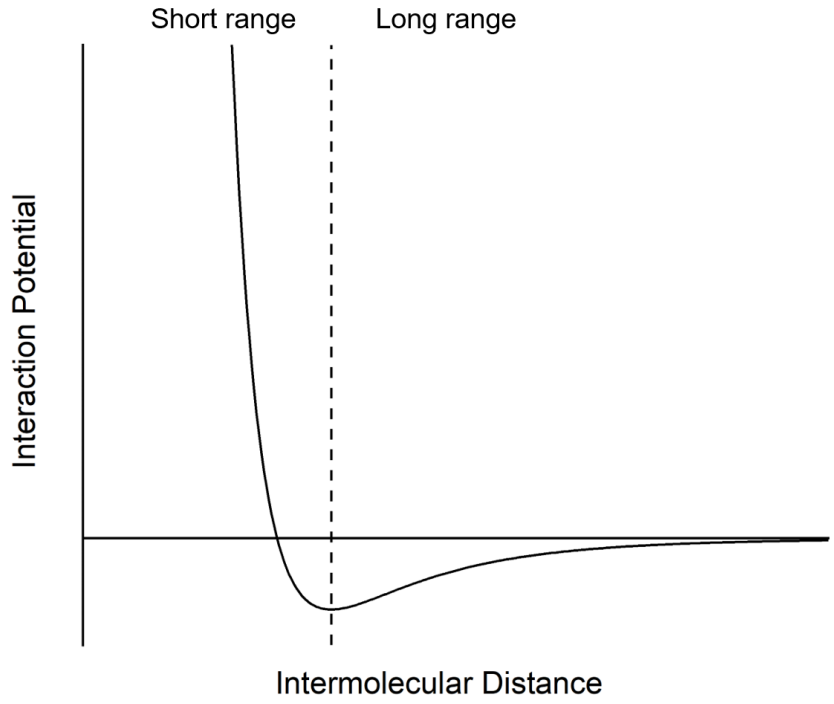

Figure 1.3: Lennard-Jones model of intermolecular interaction

An interaction potential between two molecules such as the Lennard-Jones potential (figure 1.3) has two components: A long-range part in which attractive forces dominate, and a short-range part that becomes highly repulsive at short intermolecular separations. The zero-temperature equilibrium separation distance corresponds to the position of the minimum of the energy well[8]. There are three major contributions to the long-range component, for which the interaction potential correlates with R^{-n}, where R is the intermolecular distance and n is the number of molecules in the immediate vicinity (the coordination number). The first arises due to the electrostatic attraction and repulsion between permanent dipoles in the molecules. The second happens as a result of a permanent dipole in one molecule inducing a temporary dipole in a non-polar region of a neighbouring molecule such that the two regions become attractive. The third is caused by the random movement of electrons within the molecules; their motions will correlate in order to reduce the overall energy of the system, resulting in dipoles which adopt opposite charges and therefore attract. At closer intermolecular intervals, the wavefunctions of these electrons overlap, resulting in a set of exchange forces in which the system

energy increases exponentially as the molecules move closer together. There is an attractive part as electrons can move freely between molecules, increasing their positional uncertainty and lowering the system energy, and a repulsive part due to the Pauli exclusion principle which states that no two electrons with equal spins may occupy the same space, and thus the wavefunctions must adapt which increases the interaction energy. The repulsive contribution is dominant, leading to an overall increased potential at short range[9]. In complex multi-molecular systems with many polar regions and electrons in extensive π-systems, there may be many energetic minima of differing stabilities and energy values, with the number of minima increasing exponentially with the number of molecules in the system. Some minima are meta-stable such that energetic fluctuations such as thermal vibrations may be sufficient to cause the molecules to transfer to a lower energy minimum. Quantum tunnelling may also result in spontaneous transitions past energy barriers into low-energy states[10]. Identifying the number and stability of such minima is imperative to understanding and predicting how molecular aggregates coalesce and form into ordered crystalline states.

1.2.4 Nucleation and Growth

The processes by which molecules coalesce to form crystals involves the collective coordination of potentially billions of molecules to form into an ordered state from a chaotic system in which the molecules are dissipated homogeneously throughout a host medium, such as a solute dissolved in a solvent. The first of these processes is nucleation, the formation of a nucleus (or seed), which is a localised concentration of molecules within the medium. Nuclei act as the centre of crystallisation to which more molecules will aggregate and arrange into a crystal lattice in the right conditions. Nucleation may occur spontaneously or be induced through methods which force molecules into closer proximity such as increasing pressure or applying mechanical shock. These nuclei are at first highly unstable, and many will dissipate before they become the basis of a crystal lattice. However, upon reaching a critical size, the nuclei will become stable and the crystal will grow. Nucleation will only occur spontaneously if the concentration of molecules in the host medium is greater than saturation point of the medium at a specific volume, pressure and temperature, i.e. the solution is supersaturated. Greater degrees of supersaturation will increase the likelihood of spontaneous nucleation. This may be achieved by dissolving enough of a molecule to be crystallised in a solvent in the case of liquid-phase crystallisation (or dispersing the molecule in a specific atmosphere in the gas phase) until the saturation point. The volume or temperature is then lowered through the metastable region (figure 1.4) in which the forces which bind the molecules in a nucleus together are in equilibrium with those that disperse them. At lower temperatures or volumes, the nucleation line is reached and the binding forces dominate, causing spontaneous nucleation and subsequently crystal growth. This will occur until enough molecules have been removed from the solution and it is below the saturation line[11].

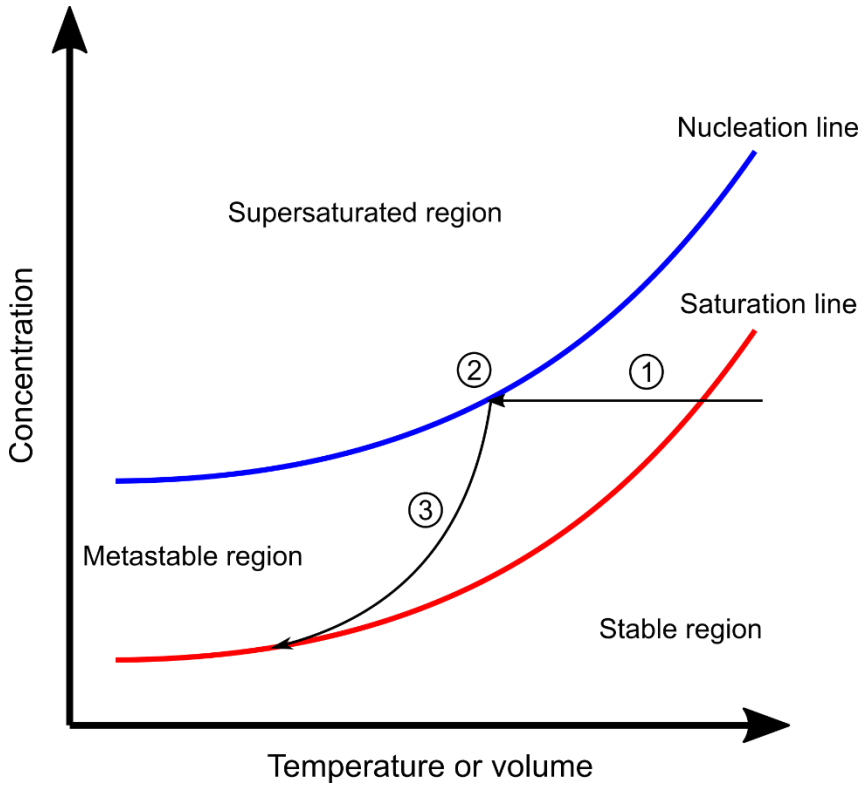

Figure 1.4: Diagram showing the process of nucleation and crystal growth. ① The pressure, temperature or volume of the solution is lowered such that it becomes supersaturated and enters the metastable region of seed formation and dissipation. ② Seeds form spontaneously from the solution . ③ The seeds grow into crystals, reducing the concentration of dissolved molecules until equilibrium is achieved and crystallisation ceases.

Crystal growth occurs when it is more energetically favourable for molecules in proximity to a crystal or seed to form bonds with molecules on the surface of the structure than remain in the host medium. The free energy of a molecule joining to a particular site on the crystal surface depends on the number of bonds that are formed as the molecule adheres to that particular site. In the terrace step kink (TSK) model of crystal growth, for a simple cubic lattice with a coordination number of six there are six different types of site to which the molecule may attach (figure 1.5). A greater number of neighbouring molecules reduces the free energy of the system to a greater degree. Therefore, the growth of crystal layers proceeds laterally via the addition of molecules to kinks, with successive layers forming upon completion. This is true for lattice types with any coordination number as the kink site will always have half the number of neighbouring molecules relative to the bulk. Defects such as screw dislocations will arise as imperfections in layer formation will create greater numbers of kink sites which will cause spiral rather than layered growth. If a critical degree of driving force during growth such as supersaturation is achieved, layers will form uniformly rather than laterally (figure 1.6), meaning that screw dislocations will not occur, and the crystal will possess fewer defects[12].

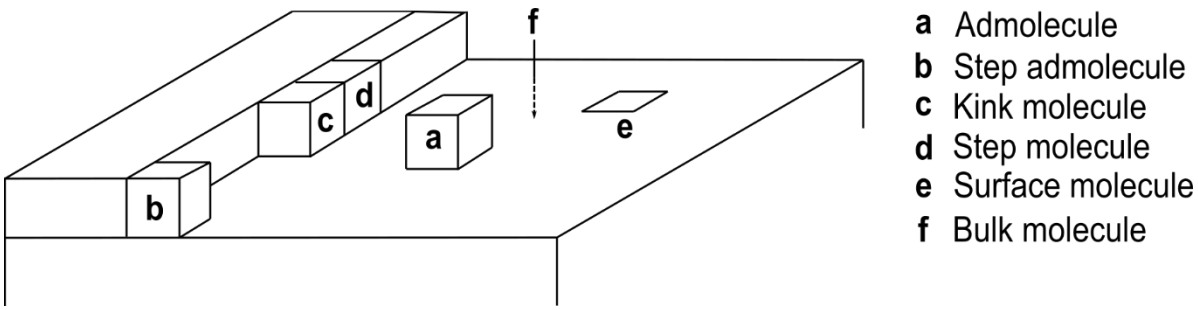

Figure 1.5: Molecular positions of the TSK model for a simple cubic lattice.

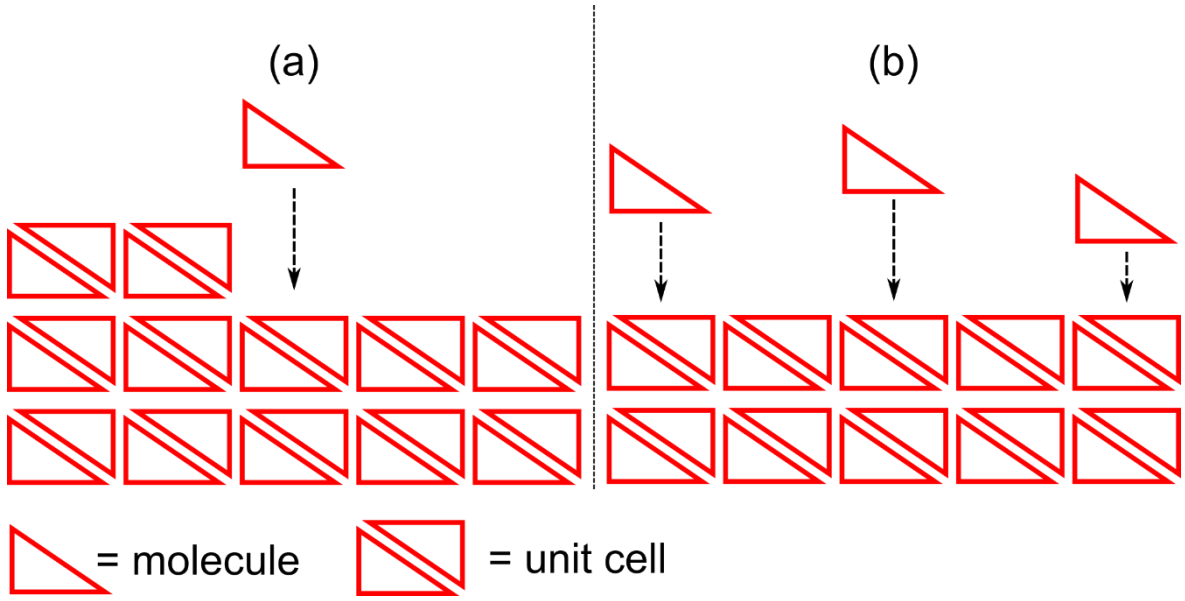

Figure 1.6: 2D schematic of two different modes of crystal growth. a) lateral and b) uniform growth.

The rate of layer formation on a particular crystallographic plane will be inversely proportional to the density of lattice points on the plane, with low density faces growing faster. However, these will eventually be overlapped by slower-forming high density faces, meaning that slower forming planes will dominate growth and define the eventual shape of the crystal. It is therefore possible to predict the shape a crystal will adopt based upon the parameters of the unit cell and its symmetry operators. However, limitations arise as different factors during growth will affect how the layers form. For example, when growing from a solution the solvent may preferentially adsorb onto particular crystal planes, meaning that energy must be applied to break the solvent-crystal bond and therefore addition of solute molecules to that plane will be suppressed[13].

1.2.5 Polymorphism

Polymorphism is a term used to describe the capability of molecules to exist in multiple arrangements or conformations (intramolecular arrangements) in the solid state, resulting in two or more different crystal structures which are described as polymorphs of each other. It appears to be a trait of many (if not all) molecules capable of crystallisation; A screen of 245 molecules performed in 2007 found that 50% had recorded polymorphs, with 90% having multiple solid forms including solvates and amorphous phases[14]. In 1965, it was remarked by Walter McCrone that "'It is at least this author's opinion that every compound has different

polymorphic forms and that, in general, the number of forms known for a given compound is proportional to the time and money spent in research on that compound."[15] Organic systems are particularly prone to exhibiting multiple different forms, due to the weak and non-directional forces which hold molecules together in the crystal lattice, which allow for many different potential unit cell arrangements. These weak bonds also facilitate the transition between forms during or after growth. Whilst polymorphs may be composed of exactly the same substance at a molecular level, each may be considered to be a unique material as their electronic and physical properties can differ greatly. An oft-cited example of an organic polymorphic system is the molecule 5-Methyl-2-[(2-nitrophenyl)amino]-3-thiophenecarbonitrile (ROY), which has to-date ten known polymorphs. Each possesses a different isomer in the unit cell in which the bond between the nitrophenyl and thiophene groups is rotated by a specific angle, resulting in crystals with different unit cell dimensions, melting point, colour, hardness and shape[16].

The polymorph that molecules adopt is dependent on the conditions under which the crystal grown or is subject to post-growth. For example, different crystal structures may manifest if the crystal is grown in two different solvents, dependent on the nature of the solvent-solute interaction, which in turn directs the intermolecular bonding between solute molecules[17]. The experimental parameters of growth will also determine the polymorph produced: a method that maintains equilibrium to as great an extent as possible such as a slow cooling or evaporation of a saturated solution, or a sublimation performed in which the substrate is close in temperature to the sublimed material will encourage the formation of the most thermodynamically stable form. This is the polymorph with the lowest free energy, equal to the difference in energy between the crystal structure and the energy possessed by each constituent molecule if isolated. However, in reaching such a state, the crystal will transition through a number of less stable structures, as per Ostwald's Rule of Stages. This states that during crystallisation, the system initially adopts the most kinetically accessible form i.e. the least thermodynamically stable, before lower energy structures precipitate in a stepwise manner until equilibrium is reached[18] (figure 1.7). If the system of growth is pushed far from equilibrium, for example if crystallisation occurs rapidly, the crystal is kinetically "locked" into one of these intermediate states and further energy must be applied in order to cause the crystal to overcome the kinetic barrier and relax into a more stable form. This may occur spontaneously over time due to thermal fluctuations, with many known cases of instantaneous polymorphic transformation post-growth.[19] It is possible for multiple polymorphs to grow concomitantly if the growth conditions are such that the nucleation rates of those polymorphs are nearly equal[20].

The substrate upon which the crystal grows may also affect the polymorph formed. This may be a crystal of the desired polymorph itself; if introduced to a supersaturated solution of the base molecule as a seed, that crystal will grow, directing growth toward that specific form as it becomes more energetically favourable to continue the structure rather than for another form to grow spontaneously from the solution. The growth surface may also be used to induce heterogeneous nucleation. If it is a crystal with unit cell parameters similar to those of a potential structure of the molecule, it reduces the interfacial free energy required for the crystallisation of that structure on the surface and alters the polymorphic outcome. This is utilised in epitaxial growth, which has been

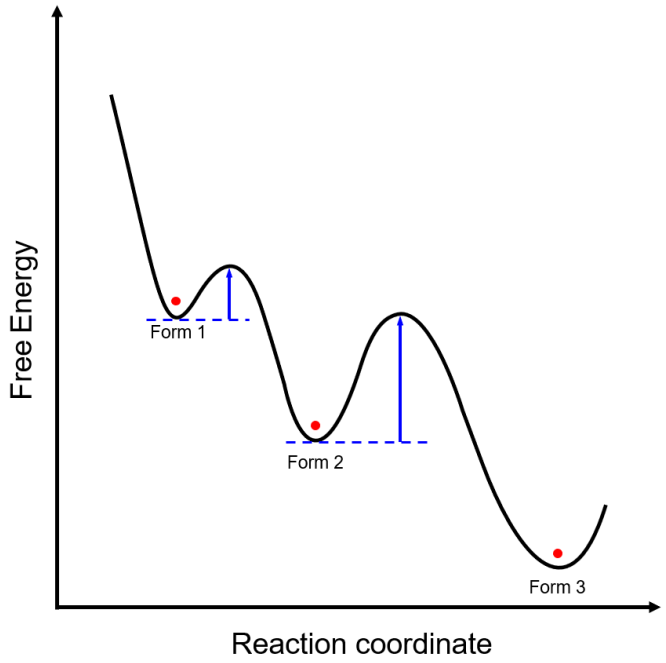

Figure 1.7: Energy diagram of the polymorphs that a crystal may transition through during growth. Initially form 1 will grow, followed by a transition to form 2 and finally to form 3 if the energy barriers (blue arrows) are overcome. This may occur either during or after growth.

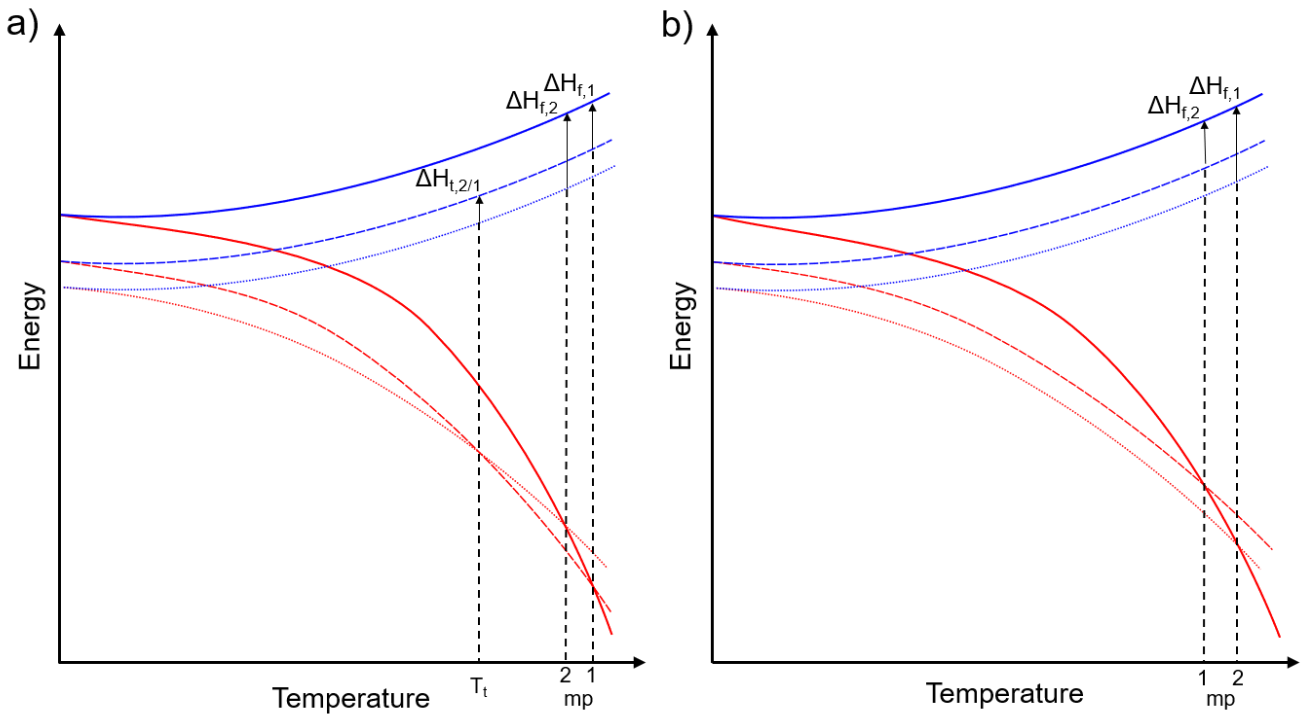

Figure 1.8: Free energy (G) and enthalpy (H) curves as a function of temperature for two polymorphs (form 1 and form 2) and the liquid phase of a) an enantiotropic system and b) a monotropic system. Blue lines: enthalpy, red lines: free energy. Solid: liquid phase, dashed: form 1, dotted: form 2. In the enantiotropic system, the crystal will transition from form 2 to form 1 (if not already in form 1) at T_t, before melting at mp 1. In the monotropic system, the crystal will remain in the same form until melting at mp 1 or 2 dependent on the polymorph.

used to grow metastable forms of organic crystals which could not otherwise be produced[21]. Polymorphic selectivity of pharmaceutical crystals via epitaxial growth has also been demonstrated, with a computationally predicted structure (form V) being grown for the first time from a surface of dihydrocarbamazepine form II

owing to the similarity in lattice parameters of the carbamazepine polymorph and the surface which it formed on[22]. Desired forms of pharmaceuticals have also been grown from gold surfaces via lattice matching[23].

The most thermodynamically stable polymorph of a crystal may change as local ambient conditions such as temperature or pressure are varied. Each polymorph has a differing free energy response to changes in temperature. As such, there may be a point at which one polymorph becomes more stable as the crystal is heated or cooled past a specific temperature as the response curves meet, resulting in a transition to the newly more stable (lower energy) form. In the case illustrated in figure 1.8a, the crystal may exist initially in form 2, before transitioning to form 1 as it is heated past the transition temperature (T_t). If this temperature is below the melting point of the crystal, it is said to be enantiotropic. If there are no points where the response curves meet, or the crossover point is beyond the melting point of the crystal (the transition temperature to the liquid phase), no temperature-mediated polymorphic change occurs, and the crystal is monotropic (figure 1.8b). The corresponding enthalpies of fusion (ΔH_f) or transition (ΔH_t), are the energy differences between enthalpy curves at the respective temperatures of phase change. Such a phase diagram may be more complex for a real system with several polymorphs which may be enantiotropic or monotropic with respect to each other[24].

1.2.6 Electronic Properties

Although there are several million reported organic compounds[25], not all will exhibit interesting electronic phenomena such as fluorescence and conductivity. In any organic molecule composed simply of single bonds, electrons are restricted to their associated carbon atom, and make good insulators such as polymers like polystyrene or polypropylene[26]. However, with molecules that contain alternating single and double bonds between their carbon atoms, there is overlap between p-orbitals and the bonds become π conjugated, delocalising electrons over the entire conjugated segment. Such segments possess bonding and anti-bonding orbitals, with the former entirely occupied by electrons and the latter entirely empty when all electrons are in the ground state. Electrons in the highest occupied molecular orbital (HOMO) may be promoted to the lowest unoccupied molecular orbital (LUMO) when excited with sufficient energy via a photon (photoexcitation) or some other means, and de-excite with the emission of a photon of energy equal to the HOMO-LUMO gap (photoemission), resulting in fluorescence. The difference between the HOMO and LUMO energy levels is the bandgap of the molecule. A longer conjugated segment increases the area over which the electrons occupying the π orbitals are delocalised, reducing the HOMO-LUMO gap and lowering photon emission wavelengths as electrons de-excite[27].

If electrons are injected into the molecule, the additional charge causes a vibrational relaxation, lowering the LUMO level and creating a polaron as nearby molecules are polarised by the negative charge. If an electron is removed from the HOMO, a positive vacancy appears in the HOMO and acts as a quasiparticle called a hole. This will then create a positive polaron. When an electron is promoted to the LUMO or some higher excited state, the electron and hole become coulombically bound together, reducing the HOMO-LUMO gap and creating a neutral quasiparticle called an exciton (figure 1.9). Excitons are mobile and can transfer between

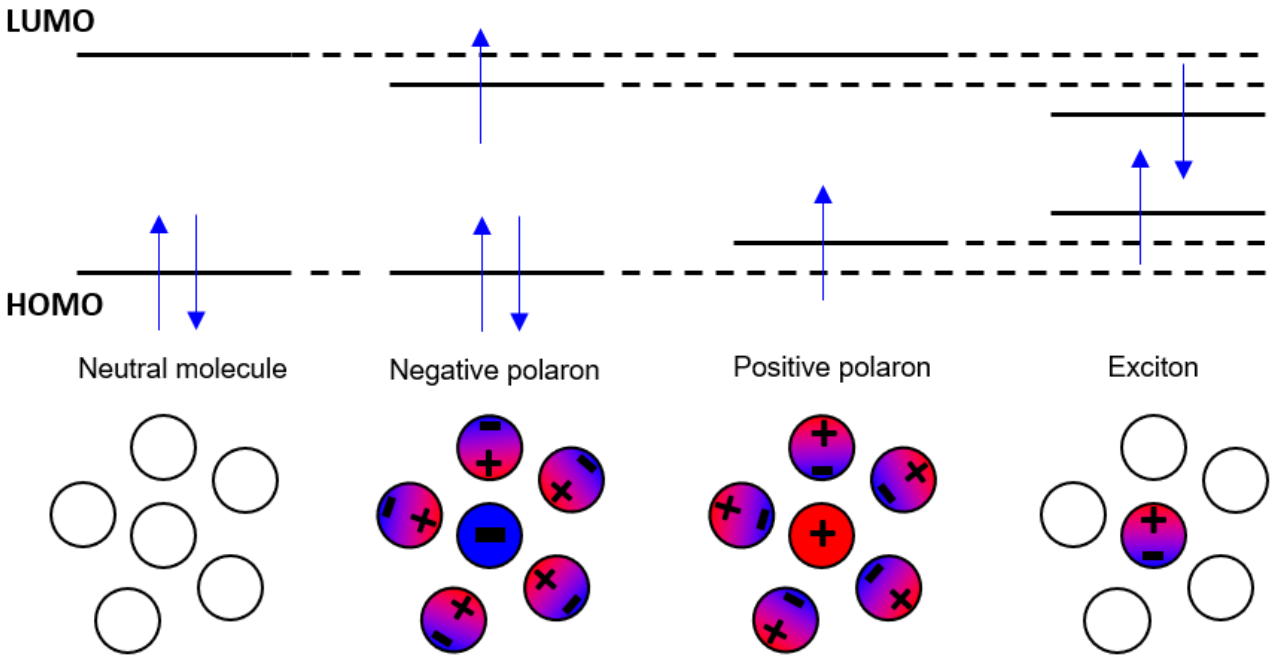

Figure 1.9: Energy levels, occupied states and polarisation as a result of neutral and excited states within organic semiconductors. Reproduced from Forget and Chénais (2013)[4]. Circles represent individual molecules.

adjacent molecules via two processes: long-range and short-range. In the long-range mechanism, Förster resonant energy transfer (FRET), the exciton transfers its energy to an electron in another molecule via dipole-dipole coupling to form another exciton, with non-radiative relaxation of the original exciton. The interaction distance is on the order of several nanometres. The short-range mechanism, Dexter transfer, happens between adjacent molecules and is a result of quantum tunnelling (hopping) of excited states across intermolecular gaps. The likelihood of this happening is dependent on the hopping distance, with greater overlap between the electronic clouds of functional groups of neighbouring molecules increasing the chance of hopping[28]. Excitons will eventually recombine, with the emission of a photon. Exciton transfer may also cause quenching of the excited state via singlet-singlet annihilation (chapter 3), in which its energy is released via non-radiative means such as heat. Therefore, in situations in which the density of fluorescent molecules is increased such as in a crystal or via greater concentration in a solvent, the quantum efficiency (a ratio of the number of photons used to excite the molecules and the number that are emitted) decreases as more excited states are quenched[29]. In the solid state, photons of shorter wavelengths can be reabsorbed, further reducing the quantum efficiency of fluorescence[30].

The absorption profile of a molecule, the intensity of light absorbed as a function of the wavelength of incident light, will often lie between 300 and 500 nm and exhibit several broad peaks with overlapping tails. The peaks are centred around the energy gap between the HOMO level (S_0) and the excited anti-bonding orbital states (S_n) with the lowest energy being the LUMO (S_1) (figure 1.10a). The broad, continuous nature of the peaks lies in the many vibrational modes (v_n) of the molecule which are coupled to the electronic states, greatly increasing the number of available energy levels and expanding the peak widths from tens to hundreds of nanometres

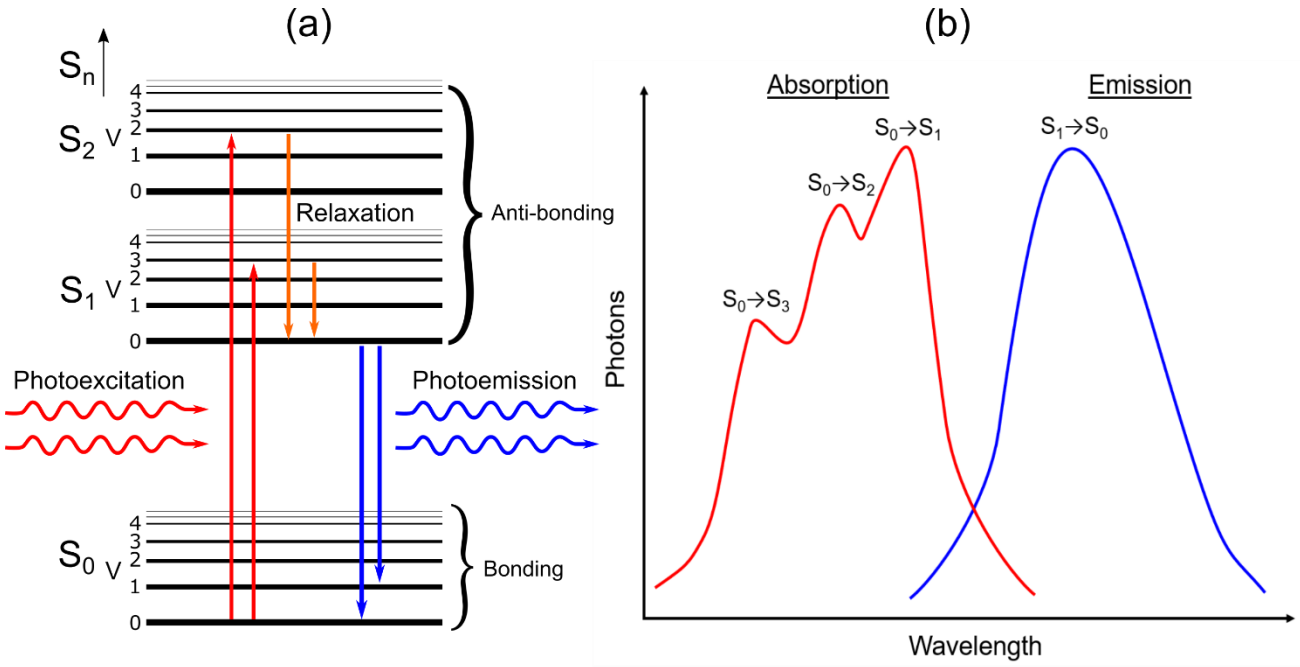

Figure 1.10: a) Jablonski diagram illustrating excitation, relaxation and emission pathways of electrons under photoexcitation. b) A typical absorption and emission spectrum of an organic molecule.

(figure 1.10b). Electronic transitions to and from the lowest vibrational states of bands may be referred to as 0–0 transitions and have the same energy in both absorption and fluorescence. Higher anti-bonding orbital states may be obscured by the vibrational modes of lower energy states, meaning that promotion to these higher states will not be apparent in the absorption spectrum. The fluorescence profile is similar, but with only a single, broad peak that is red-shifted relative to the absorption spectrum. The red (Stokes) shift is due to the Franck-Condon Principle, related to the relative timescales of relaxation of the electron and the atomic nucleus. As a molecule absorbs a photon, the molecular structure is excited and an electron is promoted from S_0 to a vibronic mode of S_1 or some higher level. The electron then rapidly decays non-radiatively to the lowest vibrational state of the S_1 level and relaxes to the S_0 level, emitting a photon while the molecule is still in an excited state. The minimum of the S_1 level lies at a higher normalised nuclear coordinate, such that it is above a higher vibrational mode of S_0. Therefore, the electron relaxes to a higher vibronic mode of S_0 before decaying to the ground state, and the photon emitted has lower energy and is thus red-shifted relative to the absorbed photon (Figure 1.11). The lifetime of electrons in the S_1 state is longer than in any higher S_n state, meaning that any electron excited to these levels will decay to S_1 before a photon is emitted. This results in there typically being only one peak in the fluorescence spectrum of a molecule[31].

The absorption and fluorescence spectra of organic crystals look broadly the same as those of the individual constituent molecules. However, as aggregation increases the likelihood of excited states being quenched, crystallisation will typically cause a reduction in the quantum efficiency of fluorescence. Exceptions lie in some structures in which there is little or no overlap in electronic wavefunctions between adjacent molecules, leading to the opposite effect. These structures are said to exhibit aggregation induced emission (AIE)[32]. The extent of intermolecular π-π overlap will also determine the area over which electrons are delocalised, reducing the

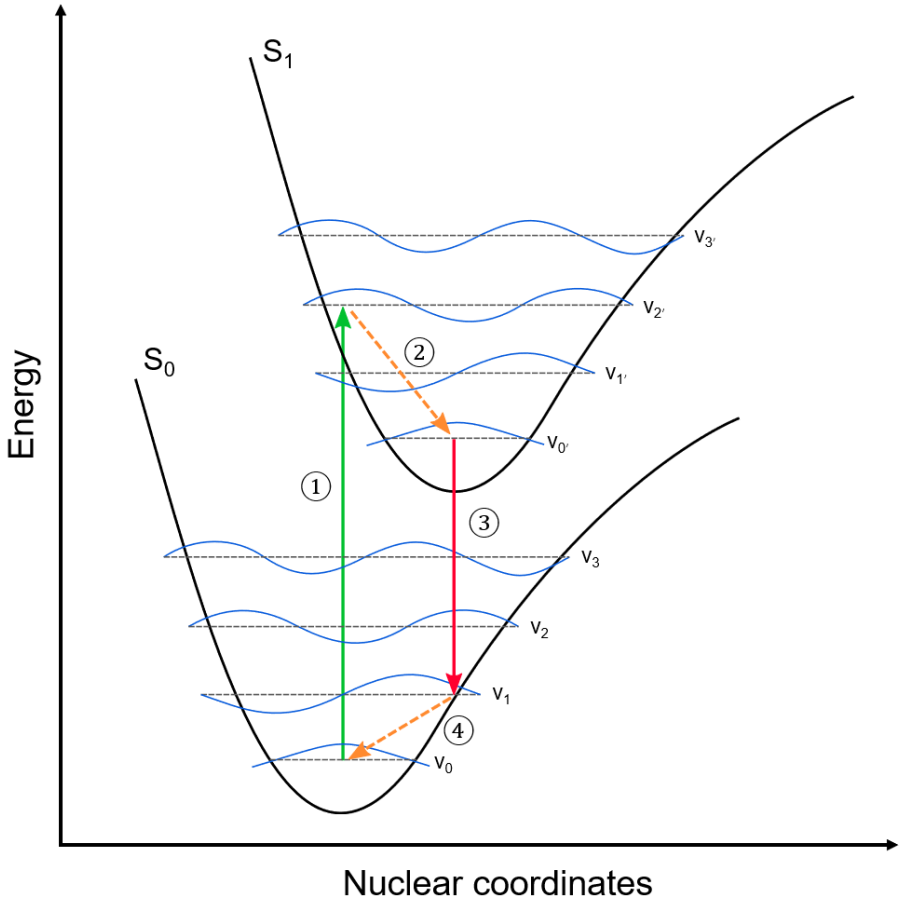

Figure 1.11: Illustration of the Frack-Condon principle. ① A photon is absorbed and an electron is promoted from S_0 to a vibronic mode of S_1. ② The electron decays non-radiatively to the ground state of S_1. ③ The electron relaxes to a vibronic mode of S_0, with the emission of a photon of lesser energy (greater wavelength) than was absorbed initially. ④ The electron decays non-radiatively to the ground state of S_0.

HOMO-LUMO gap as delocalisation increases. Therefore, the proximity of fluorophores (fluorescence-active functional groups) to others in the crystal lattice will determine both the colour and emission of the crystal. As a result, each polymorph of a molecule will have unique optical properties which may be used to identify which has been grown if XRD is not available.

1.3 Growth Methods

1.3.1 Solution Growth

The majority of crystals formed from organic molecules may be grown from solution, due to the solubility of these molecules in organic solvents. Solution growth is based on the principle that the saturation point of a solute in a solvent varies with temperature or volume (section 1.2.4). Therefore, by saturating the molecule to be crystallised in a solvent either at a specific temperature and cooling the solution down or reducing the volume of solvent (usually via evaporation), supersaturation is achieved and crystals spontaneously nucleate and grow from the solution. Selection of the correct solvent for this purpose is important; the solubility of the molecule of the solvent must vary sufficiently with temperature of growing via cooling to ensure that a high supersaturation is maintained during growth. Different techniques may be used to increase the degree of

supersaturation, which will affect the size and quality of crystals produced. This may be achieved by adding a solvent to the solution in which the molecule is not soluble in (an antisolvent) to the solution, either directly or through a vapour: a saturated solution is left to evaporate in an atmosphere of the antisolvent, and as the solvent evaporates the antisolvent vapour will diffuse into the solution, leading to supersaturation. The length of time over which the crystallisation takes place will also affect the quality of crystals produced, with longer growth periods producing larger, higher quality crystals[33]. Rapid growth may cause trapping of solvent molecules in the crystal lattice during formation or the crystallisation of a different polymorph as a metastable form grows and cannot transition to a more stable configuration (section1.2.5). Solutions may be left for weeks to evaporate before crystals are collected. A trade-off must be considered between quality and the timescale over which the growth takes place.

1.3.2 Vapour Phase Growth

Some molecules, in particular hydrocarbons with high molecular weights, may be insoluble in most solvents or produce poor-quality crystals when grown from solution. Crystallisation from the gas phase is an alternative method of growth which does not involve the use of solvents. A powdered sample is heated to its sublimation point, which will cause a transition directly from solid to a vapour. The vapour will deposit on cooler surfaces, forming crystals in the process. Sublimation is often carried out in a vacuum, as lower temperatures may be used to sublimate the growth material. This also prevents the inclusion of airborne impurities during growth. In the simplest growth setup, the powder is placed in a sealed chamber containing a cooled surface. The chamber is then evacuated and heated to the sublimation point of the powder, after which crystals grow on the cooled surface. This may also serve to purify the material, as impurities of differing molecular weights will crystallise in different regions of the apparatus. To exploit the purification properties of sublimation growth to its maximum potential, the physical vapour transport (PVT) method was developed (figure 1.12). In this setup, the starting material is placed at one end of a glass or quartz tube and heated to the sublimation point of the compound. An

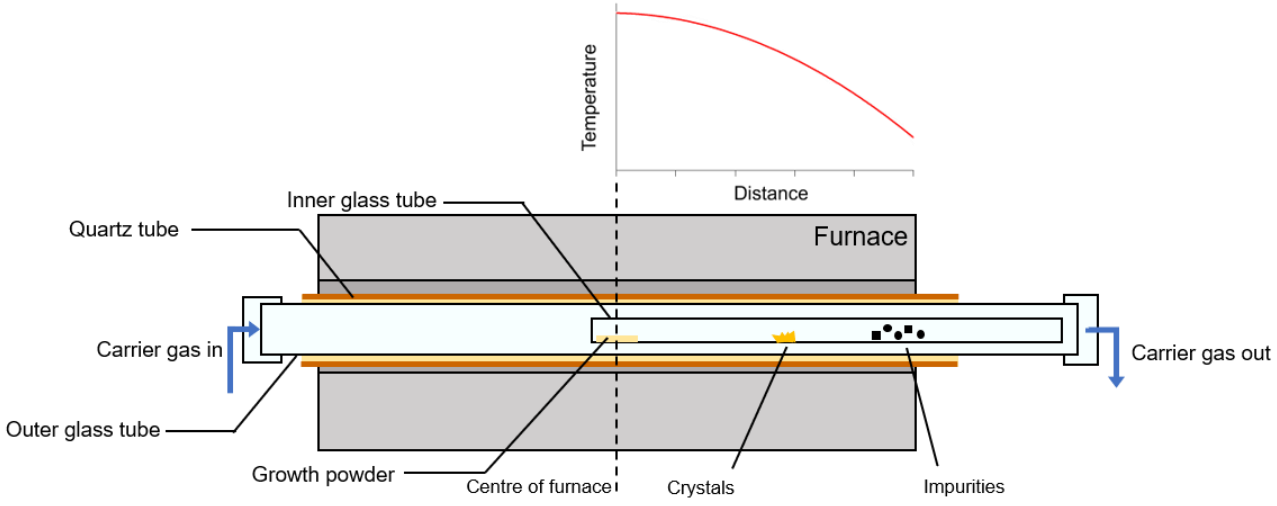

Figure 1.12: Schematic of a PVT growth setup in a single-zone furnace

inert gas such as nitrogen or helium which does not react with the sample is passed from the end containing the material and expelled at the opposite opening. A temperature gradient is established across the tube, with the sublimated material transported by the gas, condensing and nucleating on the inner walls of the tube due to the lower temperature of the glass substrate. The temperature gradient results in the purification of the material; heavy impurities either travel a shorter distance along the tube before condensing or remain at the position of the source material, and light impurities condense at a lower temperature, further along the tube from the desired crystals[34]. This method can be used to reliably produce large, pure single crystals over a short period of time, without solvent inclusion into the crystal structure which may occur in solution growth. PVT may also be carried out in a vacuum, with growth material deposited in an ampoule which is then sealed and placed in the furnace. The small volume of the ampoule results in concentration of the growth material, leading to greater crystal sizes. However, this will also result in any impurities in the powder crystallising with the desired growth material. A variation of this technique is the use of a semi-closed ampoule with a small orifice which will allow impurities to escape the ampoule, along with some of the growth material[35]. PVT may also be carried out in multi-zone furnaces which allow for greater control of the temperature of the growth region.

1.4 Characterisation

1.4.1 Structural characterisation

The principle for identifying and characterising a crystal structure is to identify the positions of atoms in the unit cell. Several techniques are available to achieve this which utilise the ordered nature of molecules in the crystal lattice. In a single crystal, atoms lie on series of equally spaced planes which can be constructed in any direction (section 1.2.2). These planes can thus be treated as lines in a diffraction grating if a probe of wavelength λ comparable to the plane spacing is used. As the wave is incident on the atomic planes, it is reflected and constructively or destructively interferes with adjacent waves dependent on the whether they are in or out of phase. This results in a series of diffraction spots where the angle θ between lines from the sample and central spot, and from the sample to either adjacent spot (equal to the incident angle of the wave on the plane) can be related to the spacing between planes d and the number of spots n from the centre by Bragg's law:

$$n\lambda = 2d\sin\theta$$

Diffraction spots appear only at points at which this condition is satisfied; under any other incident angle the reflected waves destructively interfere such that there is zero intensity at the point of measurement. This is visualised in figure 1.13 which illustrates how a two waves incident on atoms separated by d will be in phase on reflection when n is 2. By scanning over a range of θ on the sample, Bragg's law is satisfied for different planes within the crystal lattice, producing a pattern that is specific to the atomic arrangement and can therefore be used to either identify the positions of atoms in the unit cell or generate a "fingerprint" of the material which can be compared to the known patterns of materials, dependent on the method used[36].

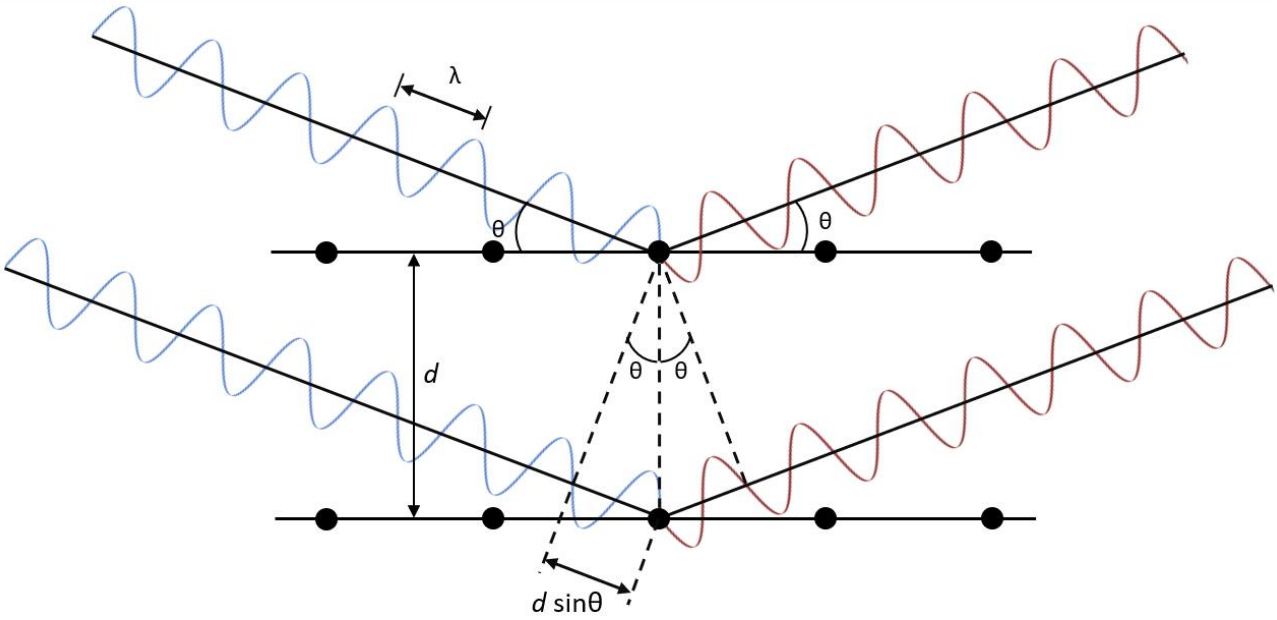

Figure 1.13: two-dimensional representation of Bragg's law between two planes in a crystal

1.4.1.1 Single Crystal X-ray diffraction

Single crystal X-ray diffraction (SC-XRD) is the standard method of unit cell characterisation, allowing for full structure solutions. The probe used is X-ray radiation, which is generated by firing electrons from a heated tungsten filament at a metal target. X-rays are then produced by displacing electrons from the inner shell of a metal atom, causing an electron in a higher shell to fall to the vacant state and release a photon of a specific wavelength. Copper or molybdenum targets are normally used, with the Kα transition from a copper target producing X-rays with wavelengths of 1.54184 Å, and Kα molybdenum transitions producing 0.71073 Å radiation. A crystal is positioned in the X-ray beam, with a photographic film behind the crystal to capture the reflected X-rays. The beam generates a two-dimensional pattern of diffraction spots, which is then expanded to three dimensions by taking scans at different crystal rotations. A computer then uses the spots to construct a probable unit cell and crystal symmetry. This process can take up to 12 hours dependent on crystal quality. Perfect single crystals that are approximately spheres of diameter 0.2 mm are ideal for SC-XRD, with defects such as twinning (in which two separate crystals grow from the same plane) reducing the accuracy of the calculated atomic positions and thus requiring more data to be collected for a full structure solution[37].

1.4.1.2 Powder X-ray diffraction

Powder X-ray diffraction (pXRD) utilises X-rays generated via the same methods as SC-XRD, but a powdered sample is used instead of a single crystal. This allows for quick analysis of samples in which growing perfect single crystals is difficult, with experiments typically taking between one and two hours to complete. The powder consists of many randomly oriented crystallites, with the assumption of complete isotropy of crystal planes in any direction. An X-ray beam is directed at the sample over a range of 2θ, with a photographic film moved accordingly to capture the reflected X-rays. The result is a pattern of rings of constant intensity, with the distance of the rings from the central point of reflection determined by the interplanar spacings of the crystal.

The X-ray intensity is measured in a line from near the centre ($2\theta = 0$) to the edge of the pattern, generating a series of peaks which can be ascribed to reflections from planes of equivalent reciprocal lattice vector magnitudes[38]. However, full structural solution is not possible without much complexity[39] as no information on the direction of planes is given. Nevertheless, the pattern generated will be unique to each crystal and can thus be compared to other patterns to identify the crystal structure if it is already known. Thorough crushing of sample for pXRD is required, as preferential orientation causes differences in peak magnitude as some planes become over-represented in the pattern, which can lead to misidentification of the material or structure.

1.4.1.3 3D Electron Diffraction Tomography

Electron diffraction tomography (EDT) utilises the duality of electrons as both particles and waves with wavelengths of around 0.025 Å when incident on the sample. This greatly reduced wavelength when compared to X-rays allows for structural analysis of crystals smaller than one micron, but their matter interaction is approximately 10^3 times stronger, leading to sample destruction under extended exposure. EDT is used with samples under a transmission electron microscope (TEM) to identify individual crystallites and provides information on their space group and orientation with respect to the beam. A recently developed technique utilising a rotating TEM grid and low-dose electron beam allows for complete structural solutions on nano-sized crystals without their destruction, meaning that unit cells may be determined from samples where growth of single crystals of sizes on the order of 100 μm cannot be achieved[40].

The elementary composition of a region of the sample may also be measured via energy-dispersive X-ray (EDX) analysis. In this mode, characteristic X-rays are detected which are emitted as a result of the electron beam scattering electrons in lower energy orbitals of atoms on the sample surface, causing electrons at higher energy levels to fall into the lower level and release a photon. This photon has energy equal to the difference in energy between the two orbitals, which is characteristic of the element that the photon originated from. The distribution of detected X-ray energies therefore gives the proportion of each element present in the investigated region[41].

1.4.2 Optical characterisation

1.4.2.1 Ultraviolet-visible spectroscopy

Ultraviolet-visible spectroscopy (UV-Vis) (figure 1.14) is crucial tool in quantitatively determining the optical behaviour of organic samples and their electronic structure. UV-Vis measures the relative intensity of light absorbed by a sample over a range of wavelengths (the absorption spectrum) between the ultraviolet and visible regions of the electromagnetic spectrum (typically 190 – 750 nm dependent on the spectrometer used) either dissolved in a solvent or in the solid state. This is achieved by firing a beam of light of known wavelength at the sample and measuring either the light transmitted through it if it is translucent or measuring the light reflected from its surface if it is opaque. In order to generate light for this purpose, a tungsten lamp is used when measuring in the visible range down to approximately 350 nm, with a deuterium lamp for lower wavelengths down to 160 nm. The light produced this way is passed through a filter followed by a monochromator resulting in a beam with a narrow, well-defined spectral profile at a desired wavelength which is pointed at the sample.

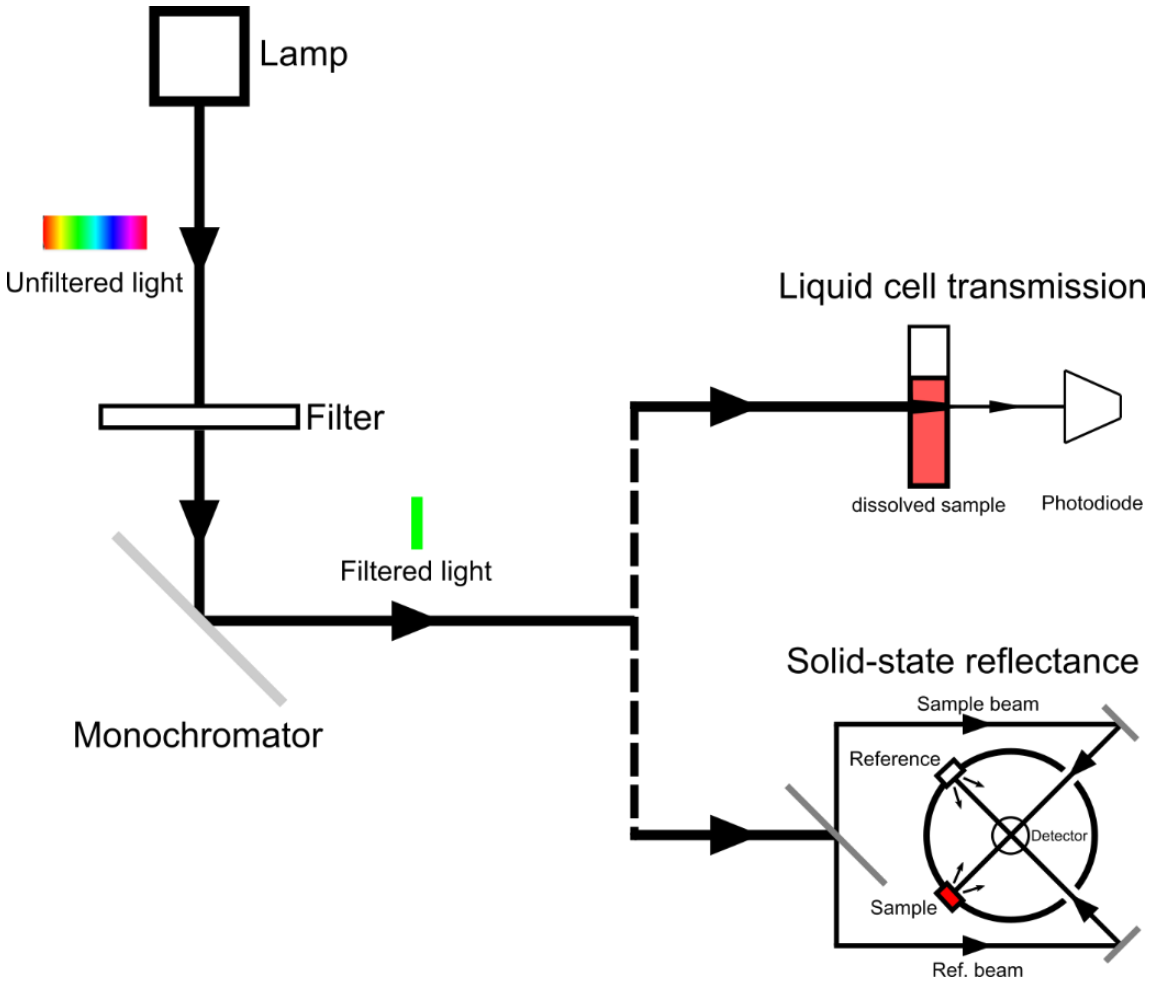

Figure 1.14: UV-Vis schematic for liquid cell and diffuse reflectance measurements.

The total light reflected or transmitted is then measured using a photodiode and used to generate a spectrum as the spectrometer scans through the desired range of wavelengths. The profile of a reference is first measured which is subtracted from the profile of the sample in order to ensure that the profile contains features which are exclusive to the sample[42].

Liquid cell measurements, in which the sample is dissolved in a known solvent, can provide information on the electronic structure of individual molecules (monomers) if the sample is sufficiently dilute, or there are no solvent-solute interactions. It can also measure the effects of molecule aggregation as concentration is increased or determine the onset of crystallisation in a supersaturated solution. The spectrometer is run in transmittance mode for these measurements, in which the percentage of light which passes through the sample relative to the incident light intensity is recorded. The reference used is a quartz vial of the solvent without any dissolved sample. Solid samples are typically opaque, meaning that the proportion of light reflected from the sample must instead be utilised. The reflected light is collected via an integrating sphere which detects light scattered non-symmetrically to the normal line (diffuse reflectance) and compares the intensity to that of a beam of equal intensity to the one incident on the sample scattered from a perfectly white reference by the same angle. To

obtain the equivalent absorption spectrum from diffuse reflectance data, procession with the Kubelka-Munk equation is required:

$$\frac{k}{s} = \frac{(1 - R_\infty)^2}{2R_\infty}$$

where k is the absorption coefficient, s is the scattering coefficient and R_∞ is the relative reflectance ($R_{\text{sample}}/R_{\text{reference}}$)[43]. Sample molecules in the solid state are more concentrated, leading to greater degrees of delocalisation and therefore typically resulting in absorption bands at higher wavelengths (section 1.2.6).

1.4.2.2 Fluorometry

Fluorometry measures the fluorescence emission profile of a sample over a range of wavelengths from the visible spectrum to the near infra-red. Samples comprised of small organic molecules typically emit between 400 nm and 600 nm, with emittance at higher wavelengths possible due to factors such as excited-state intramolecular proton-transfer causing exacerbated Stokes shifts[44]. Light is generated and filtered to produce light beams of controllable, well-defined wavelengths for fluorometry analysis in the same manner as UV-Vis. Fluorometers can be run in two modes: an emission mode in which the sample is excited at a particular wavelength and the light produced is measured by scanning over a particular region of the electromagnetic spectrum, and an excitation mode in which the emission at a specific wavelength is measured and the relative intensity of light is tracked as the sample is excited over a range of wavelengths. The emission or excitation wavelength chosen is based on where the sample emits or absorbs the strongest, as the resulting spectra will have the greatest intensity and therefore produce well-defined peaks with minimal noise contribution. Comparing absolute intensities between solid samples via this technique is difficult as the intensity is dependent on non-intrinsic sample properties such as the number of exposed emitting molecules on its surface[45].

1.4.3 Differential Scanning Calorimetry

Differential scanning calorimetry (DSC) is a widely used analytical technique which determines the temperature at which phase changes occur and the energy required for such changes to occur in a material. This will include melting, boiling, freezing, condensing, subliming, deposition, glass transitions, crystallisation or crystal structure transitions. Each of these phase changes will result in the release of energy as the sample moves to a lower energy state (exothermic) or the intake of energy from surroundings as energy is required in the formation of the resulting phase (endothermic). A differential scanning calorimeter measures the changes in free energy of a sample relative to a reference via the energy required to heat or cool it over a set range of temperatures. The sample is enclosed in a hermetically sealed heat-conductive pan, with a similar pan containing no sample used as reference. When measuring the phase changes of organic crystals, several temperature sweeps from low temperature to high and back again are then typically carried out with limits based on the melting point of the crystal. The melting point is determined by extrapolating the linear portion of the exothermic transition to the baseline when there is equilibrium between the sample and reference. The point of freezing is determined in the

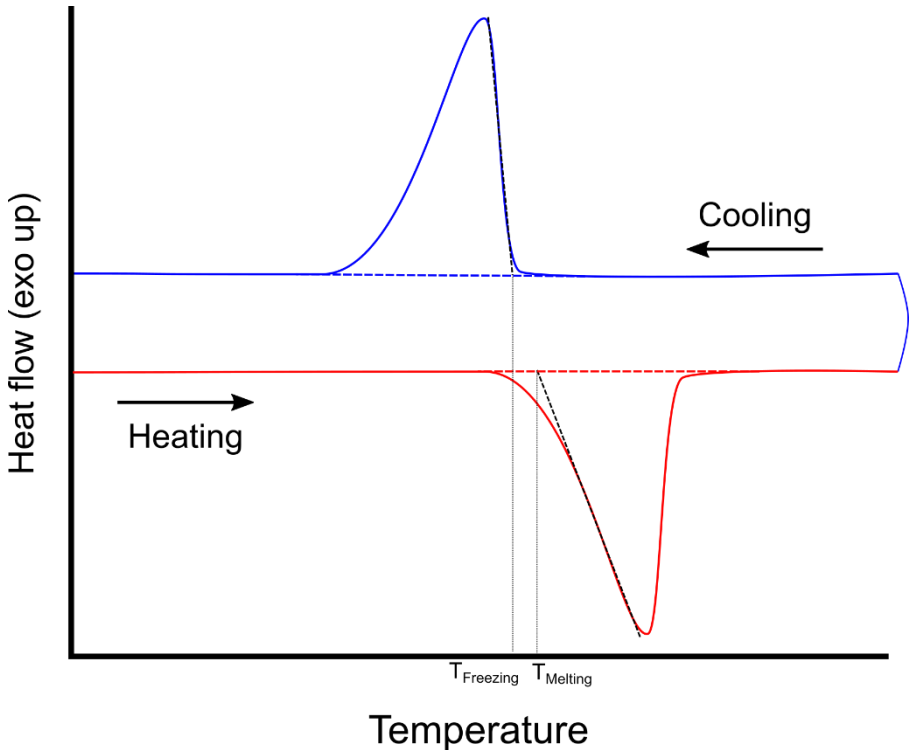

Figure 1.15: Melting and freezing of a crystal over a DSC temperature cycle

same manner from the associated exothermic transition (figure 1.15). The relative stabilities of two crystals may be determined by comparing the latent heat of melting of each, calculated by integrating the area under the exothermic melting peak. The crystal with a greater latent heat of melting requires more energy to melt a specific amount of material and is therefore more stable[46].

1.4.4 Scanning Electron Microscopy

Scanning electron microscopy (SEM) is used to image microstructure and morphology of crystals. This is achieved using a beam of electrons which interact with atoms on the surface of the sample, scattering electrons from outer orbitals which are then detected by a scintillator. As electrons are used to build the image rather than light, the resolution is not restricted by the diffraction limit, allowing for the visualisation of features on a sample at greater magnification than could be seen with an optical microscope[47]. As with TEM, EDX may also be used with SEM to identify the atomic composition on a particular region of the sample.

1.5 Structure-Property Modelling

The use of simulations and computer-generated models of real systems form an important part of the study of material properties. These methods may be used complementarily to experimental tests to advance understanding of the fundamental processes which result in observed phenomena, or to predict behaviour of systems under particular conditions to guide future experiments. The computational methods used in the following chapters are outlined here.

1.5.1 Density Functional Theory

Density functional theory (DFT) is a computational technique used to study the electronic structure of atoms and molecules, taking into account the quantum behaviour of electrons described by the Schrödinger equation. Solving this equation for even single molecules is non-trivial as all interactions for individual electrons and nuclei with all others must be calculated. DFT simplifies by calculating electrons collectively as density rather than individually, massively reducing the number of calculations required and therefore making simulation of complex condensed matter systems at the atomic scale feasible using modern computers[48]. It is therefore widely used across many different disciplines to predict chemical and physical properties, with a high number of practical applications including tailoring catalysts for reactions[49] and modelling planetary composition[50]. Within the field of small organic molecules, DFT can simulate their band structure, geometries, conformational energies, electronic distribution, NMR spectrum and optical absorption and emission[51]. DFT may be used to calculate the lattice energy of a crystal, i.e. the energy required to separate a mole of a crystal into gaseous molecules. This may then be used to establish the relative stabilities of two polymorphs or determine how factors such as different functional groups will affect the stabilities of crystals[52].

1.5.1.1 Electrostatic potential surfaces

Electrostatic potential (ESP) is a measure of the potential present at any point around a molecule as a result of static concentration of charge. It is calculated from the coulomb interaction of the local charge density a point $\mathbf{r}$, $\rho(\mathbf{r})$, and the charge on the nucleus Z_A, at a position R_A. Summing over all nuclei A and integrating over all volume elements $d\mathbf{r}$, the equation has the form

$$V(\mathbf{r}) = \sum_A \frac{Z_A}{|R_A - \mathbf{r}|} - \int \frac{\rho(\mathbf{r}')d\mathbf{r}'}{|\mathbf{r}' - \mathbf{r}|}$$

The potential calculated in this way is in atomic energy units (hartrees). In order to represent the charge distribution around a molecule, it is convenient to define a surface of constant $\rho(\mathbf{r}')$ and display the potential on a tight packed grid around the surface. An isovalue of 0.0004 e.Å^{-3} is typically used, allowing for the reflection of important features of the molecule such as π-conjugation and lone pairs, whilst being in a region in which the perturbation of density via an external charge causes minimal alteration to the surface. It is therefore indicative of the potential a molecule Y would experience when approaching a molecule X for which the ESP surface has been calculated. Whilst dispersion forces cannot by illustrated via a static surface, information is provided on van der Waals interactions such as hydrogen bonding which are principally driven by electrostatics[53]. From the ESP surface of benzene (figure 1.16), it would be expected that the positive edge of the molecule would interact with the electron-rich core of another. This can be seen in its crystal structure, in which neighbouring molecules are perpendicular to each other[54].

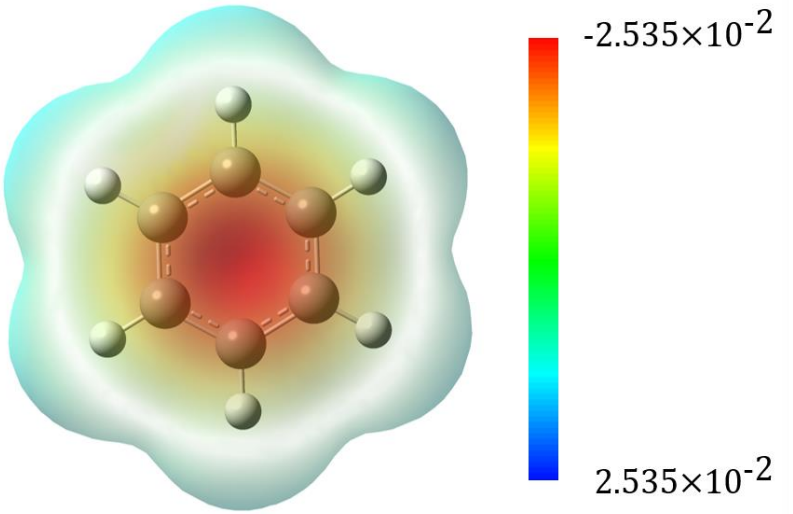

Figure 1.16: ESP surface of a benzene molecule, showing the concentration of charge toward the centre of the molecule. Units in eV.

1.5.1.2 Interaction potentials

When two molecules approach each other, the cumulative effect of attractive and repulsive forces is given by the interaction potential, which is a combination of the interaction energies between nuclei and electrons with those of the approaching molecule. Its value is dependent on the distance between and orientations of the molecules, and the resultant forces between permanent and induced dipoles. When this value is at a minimum, the molecules are at their most stable configuration and will remain in place without external influence. By calculating its value for different molecular conformations, their relative stabilities may be established, providing information on preferred arrangements. Calculating the interaction potential between molecules placed at each point on a grid on a two-dimensional surface generates a potential landscape showing the position of thermodynamically stable minima and thus how clusters of molecules would likely form in solution before nucleation[55].

1.5.1.3 Crystal structure prediction

Crystal structure prediction (CSP) is a DFT method of predicting stable polymorphs of molecules by simulating many different potential unit cell configurations and calculating their lattice energies in order to find energetic minima which molecules are likely to adopt. Those which are predicted to be more stable are in general more likely to be grown through experimental methods. CSP is used principally in the pharmaceutical industry in which polymorph screening for structures with desired properties is paramount[56].

1.5.2 Force-Field Calculations

Through minimisation of the single-point energy, the most stable configuration of one or more molecules may be computed via DFT. However, these calculations rapidly become computationally expensive as the electron density must be recalculated on each step towards minimisation. Another method of calculating molecular

dynamics is to treat the collective effect of electrons as a static potential with terms that vary according to semi-empirical methods. The resultant interaction potential can be separated into electrostatic, repulsion and dispersion components, with their associated fields and parameters[57]. This is therefore faster to simulate than via standard DFT methods as the potential surface doesn't need to be recalculated on each iteration. However, force-field calculations assume that molecules are rigid bodies and therefore the rotation of any bonds able to do so will not be considered.

2 Chapter 2: Experimental and Computational Techniques

This chapter provides details on the experimental and computational methods used in the following research chapters.

2.1 Sample Preparation

2.1.1 Synthesis of bis(4-bromophenyl)fumaronitrile

Synthesised as previously reported[58]. 2-(4-Bromophenyl)acetonitrile (0.1 mol) and iodide (0.1 mol) were dissolved in diethyl ether (400 mL) under an inert nitrogen atmosphere. The reaction was cooled to -78 °C and sodium methoxide (0.2 mol) was dissolved in dry and cold methanol, before being added drop-wise to the solution over 30 minutes. The solution was left in a dry ice bath for 2 hours and then an ice bath for the following 3 hours. After this, the solution was stirred for 3 hours at 10 °C before quenching with 3-6% hydrochloric acid. The solution was filtered, and the filtrate was washed with a cold methanol-water solution. The product was purified using silica gel column chromatography and were separated using methanol, and recrystallized.

2.1.2 Extraction of karpatite from surrounding minerals

The naturally formed karpatite was reclaimed by gentle excavation of the soft crystalline region, embedded in surrounding quartz, using a PTFE coated spatula to avoid metallic contamination. The pale-yellow flakes were separated from any debris under an optical microscope, with no further purification being performed.

2.1.3 Solution Crystal Growth

2.1.3.1 Bis(4-bromophenyl)fumaronitrile

A saturated solution of Br-FN in dichloromethane (3 ml) was left to evaporate in an atmosphere of methanol. Crystals spontaneously nucleated from the solution and were collected after a Ten-Day Interval when the solvent had completely evaporated.

2.1.3.2 Coronene

Coronene was synthesised using (97%) purchased from Sigma-Aldrich UK and twice purified by sublimation under vacuum after recrystallization from toluene. The resulting crystals were yellow needles of various lengths up to a maximum of 5 mm.

2.1.3.3 Persulfurated coronene

Solvent crystallisation was first attempted via a number of common solvents. Previous work established the solubility of PSC in N-Methyl-2-Pyrrolidone (NMP)[59], with a solubility test finding it to be soluble to 2 mg per ml. However, under cooling of a saturated solution at 60 °C to -10 °C, all material remained in solution.

Evaporation was not feasible due to the high boiling point of NMP. Crystallisation was attempted in solvents with similar polarities to NMP: DMF, DMSO, toluene, ethyl acetate and THF. PSC was found to be soluble to less than 1mg per ml in all solvents tested.

Dropcasting: PSC powder was added to 3 ml of NMP at 60 °C beyond the point at which no more could be dissolved and left for 48 hours such that saturation could be attained. The solution was then pipetted onto a cooled microscope slide at -10 °C.

2.1.4 Vapour Crystal Growth

2.1.4.1 Furnace temperature measurement

A thermocouple was attached to a pole which was inserted into the glass tube inside the tube furnace, such that the thermocouple was positioned at the centre of the furnace, with a carrier gas flowing through the tube. Temperature measurements were then taken stepwise from the centre to the edge of the glass tube in increments of 1 cm.

2.1.4.2 Physical vapour transport growth of bis(4-bromophenyl)fumaronitrile

A glass tube (inner diameter 39.5 mm) containing an inner growth tube (inner diameter 17 mm) with bis(4-bromophenyl)fumaronitrile powder placed at one end was inserted into a quartz tube. This was then inserted into a Carbolite CTF horizontal tube furnace such that the powder was positioned at the centre of the furnace. Nitrogen gas was passed through the glass tube at a flow rate between 0.1 and 0.6 L/ min. The temperature of the central point of the furnace was set to 240 °C. Crystals formed on the inner walls of the growth tube after 5 hours at distances between 120 and 300 mm from the powder.

2.1.4.3 Sublimation recrystallisation of karpatite

Powdered karpatite crystals were placed at the base of a round-bottomed flask with a glass finger held with a weak force and cooled by running water positioned above. Air in the chamber was evacuated and the flask was heated to 220 °C. After 24 hours all powder had sublimated and crystals had grown on the surface of the cold finger.

2.1.4.4 Physical vapour transport growth of persulfurated coronene

PSC powder was positioned at the centre of a tube furnace in a glass tube heated to 250 °C, with a temperature of 100 °C at either end with an approximately consistent temperature gradient between the centre and edge. Nitrogen gas was passed through the tube at a flow rate of 0.2 L/ min. All sample had either decomposed or sublimated within an hour. This was repeated in a 15 cm long vacuum sealed glass ampoule positioned at the centre of the furnace, giving the same result.

2.2 Structural Characterisation

2.2.1 Powder X-ray Diffraction

All pXRD data in this work was collected on a Bruker D8 powder diffractometer using Cu Kα radiation (wavelength = 1.5418 Å) with a PSD LynxEye Detector.

2.2.1.1 Bis(4-bromophenyl)fumaronitrile

Data were collected on crystals of bis(4-bromophenyl)fumaronitrile at 300 K over a 2θ range of 5 to 50° with a step size 0.0114° and a hold time of 1 s. Samples were mounted on a low-background sample holder with silicon wafer.

Low temperature pXRD: A scan from 7 to 40 2θ with a step size of 0.01968 over 41.25 minutes was taken at 300 K. The sample was cooled to 12 K with an Oxford Cryosystems PheniX cryostat as rapidly as possible and was held at 12 K for 15 minutes, after which a scan with the same parameters was taken. The sample was then heated back to 300 K and another scan was taken.

2.2.1.2 Coronene and karpatite

Data were collected on coronene and karpatite crystals over a 2θ range of 5 to 50° with a step size of 0.0411° and a hold time of 1.5 s. Both crystals were subject to a gentle crushing prior to analysis to assure that they remained on the sample holder. Both samples were mounted on a low-background sample holder with silicon wafer.

2.2.1.3 Persulfurated coronene

pXRD data of as-received PSC powder were collected with a chromium-plated copper sample holder over 5-50° 2θ. This was also performed on aggregates formed via Dropcasting. An Oxford Cryosystems PheniX stage was used to collect XRD scans of the as-received powder at 12 K and again at 300 K after warming over a 2θ range of 5-50°.

2.2.2 Single Crystal X-ray Diffraction

2.2.2.1 Bis(4-bromophenyl)fumaronitrile

Single crystal X-ray diffraction data (SC-XRD) for form 1 and 2 were collected on a Bruker Apex II CCD diffractometer using Mo Kα radiation (λ = 0.71073 Å) at a temperature of 100 K. Intensities were integrated in SAINT and absorption corrections based on equivalent reflections were carried out using SADABS. The structure was solved using Superflip and refined against F2 in ShelXL[60] using Olex2[61]. All of the non-hydrogen atoms were refined anisotropically, while all of the hydrogen atoms were located geometrically and refined using a riding model. Crystallographic data for form 1 and 2 have been deposited with the Cambridge Crystallographic Data Centre as supplementary publication CCDC 1568482 and 1563251 respectively.

2.3 Optical Characterisation

2.3.1 Ultraviolet-Visible Spectroscopy

2.3.1.1 Coronene and karpatite

UV-vis spectroscopy was taken using a Perkin-Elmer Lambda 25 UV/vis spectrophotometer. Samples in solution were dissolved at a known concentration, and dispensed into a 1 cm path-length, quartz cuvette and tested for absorption between 280 and 360 nm. UV reflectance was obtained in the solid state by mounting the crystalline sample on a barium sulphate substrate behind a quartz window. Using $BaSO_4$ as a reference, the diffuse reflectance of the sample was recorded. This reflectance was converted to analogous solid absorption using the Kubelka-Munk function

2.3.2 Fluorescence Spectroscopy

2.3.2.1 Bis(4-bromophenyl)fumaronitrile

Measurements were obtained from an Agilent Cary Eclipse Fluorescence Spectrometer after mounting crystalline samples on the end of a quartz plate using paraffin oil. The quartz plate, cut at an 8° angle, allowed for emitted light to be detected but not directly reflect the incident beam.

2.3.2.2 Coronene and karpatite

Measurements were obtained after mounting crystalline samples on the end of a quartz plate using paraffin oil. The quartz plate, cut at an 8° angle, allowed for emitted light to be detected but not directly reflect the incident beam. Initial excitation wavelengths were informed by solid state UV-Vis results after which emission peaks were identified.

2.4 Differential Scanning Calorimetry

2.4.1 Bis(4-bromophenyl)fumaronitrile

DSC data were collected with a TA-Instruments Q100 DSC. 5.3 mg of each sample was hermetically sealed in an aluminium pan and equilibrated at 190 °C, before being subject to a temperature ramp from 190 °C to 240 °C at a rate of 10.00 °C min^{-1}, then ramped back down to 190 °C at the same rate.

2.4.2 Persulfurated coronene

2.8 mg of powdered PSC sample was hermetically sealed in an aluminium pan and subject to a heating and cooling cycle between -70 °C and 300 °C, and from 300 °C to -70 °C at a rate of 10 °C per minute.

2.5 Scanning electron microscopy

All Scanning Electron Microscopy (SEM) samples were prepared by mounting on 7 mm aluminium stubs using a sticky carbon pad. These were then sputter coated with a 15 nm of silver. Images were acquired using a JEOL

JSM 6330F high-resolution SEM with a field emission gun and captured using a range of working distances and accelerating voltages.

2.6 Computational Analysis

2.6.1 Lattice energy calculations of Bis(4-bromophenyl)fumaronitrile

Lattice energy calculations were performed in a developer version of the CRYSTAL14 program package[62], with a screened exchange hybrid functional (HSE-3c)[63]. The Brillouin zone was sampled with γ-centred grid with 3x3x3 and 6x3x2 k-points for form 1 and form 2, respectively. Standard thresholds were applied for self-consistent field convergence, geometry optimization and integral screening. The experimental unit cell was used, and atomic positions were relaxed within space group constraints.

2.6.2 ESP calculations on planar aromatic molecules

All electrostatic potential calculations in this chapter were performed via DFT with a B3LYP functional and 6-31G (d,p) basis set. Single point energy calculations were performed with a dispersion-corrected B3LYP functional (TD-B97D) and 6-31(g) basis set.

2.6.3 Crystal structure prediction

Sulflower and persulfurated coronene were first geometry minimised in the gas phase at the PBEPBE/6-311+G(d,p) level of theory using Gaussian[64], and atomic point charges extracted. The global search was performed using CrystalPredictor II[65], with 500K minimisations. Dispersion–repulsion contributions towards the lattice energy were estimated by using a Buckingham exp-6 function with the potential parameters for Carbon[66] and Sulphur[67] from the FIT set of Williams and co-workers. Following analysis and clustering, DMACRYS[68] was used to refine the lowest energy 1000 structures in each investigation, at the same level of theory. The lattice energies reported in the landscapes are given per formula unit.

3 Chapter 3: Vapour Phase Growth of Bis(4-bromophenyl)fumaronitrile and Polymorphism

The work in this chapter was published in part in the Royal Society of Chemistry journal CrystEngComm on the 10th October 2017[69]. I wrote the paper used in this chapter. I performed solvent and vapour phase crystal growths, UV-Vis, fluorometry, pXRD, SC-XRD and SEM. Synthesis of bis(4-bromophenyl)fumaronitrile was performed at first by Jason Potticary and Lui Terry, then by Barnaby Smith. DSC was performed by George Whittell and DFT lattice calculations were performed by Jan Gerit Brandenburg. SC-XRD refinement was performed by Hazel Sparkes.

3.1 Introduction

Physical Vapour Transport (PVT) is a technique commonly used to grow large single crystals of organic molecules. The size and purity of crystals crown via this method when compared to those produced via solution-based methods often makes this growth technique preferable within the field of organic crystal semiconductor devices in which large (~ cm) sized crystals are desired, and the inherent purification of the sample which takes place during vapour growth ensures very few impurities are present in the crystals when compared to those grown from solution[2]. This is particularly advantageous for the fabrication of optoelectronic devices with organic crystals as the emitting medium, in which high purity is critical due to the effect that even trace amounts of impurities can have on the electronic properties of the bulk[70]. Furthermore, it does not require the use of potentially harmful solvents and allows for the growth of molecules which may be insoluble or barely soluble in any solvent[71]. There are also cases in which entirely different crystal structures have been grown from the vapour phase to those that had been formed from other methods of growth[72]. Crystals of the organic semiconductor rubrene are typically grown via PVT. Rubrene possesses the highest known carrier mobility amongst all organic materials having been measured up to 43 $cm^2V^{-1}s^{-1}$ [73]. Whereas solution growth of rubrene yields crystals below 0.5 cm^3 in volume after four weeks[74], PVT can produce plate-like crystals typically 1 cm along each of the long axes and 20 μm in the short axis, which appear after only 1 hour of growth

One phenomenon which has been observed in the PVT growth of crystals from several different molecules is the emergence of multiple polymorphs within different regions within the growth apparatus, with each polymorph preferentially growing within a particular temperature region[75,76,77] . These polymorphs have differing colours and fluorescence emission profiles as a result of their unique packing structures which determine the extent of π-π overlap between adjacent molecules (section 1.2.6). However, the kinetic mechanisms that give rise to the preferential growth of one polymorph over another have not been fully investigated. By elucidating this mechanism and how it relates to properties of the resulting crystals such as

crystal stability and fluorescence, the tailored growth of polymorphs with optimal properties for optoelectronic devices may be achieved. Such knowledge could aid in ensuring that desired polymorphic forms may be produced consistently, or potentially lead to the discovery of new forms if the growth conditions are carefully considered.

3.1.1 Bis(4-bromophenyl)fumaronitrile

Bis(4-bromophenyl)fumaronitrile (henceforth referred to as Br-FN) is an aromatic molecule with two bromine-substituted aromatic rings linked by a fumaronitrile bridge (figure 3.1a). It is used as a precursor for bis(4-(N-(1-naphthyl)phenylam-ino)phenyl)-fumaronitrile (NPAFN) and N-methyl-3,4-bis(4-(N-(1-naphthyl)phenylamino)phenyl)maleim-ide (NPAMLMe), efficient emitters for non-doped red organic light-emitting diodes[58]. It has also garnered attention for forming single crystals which fluoresce intensely under exposure to ultra-violet light, with comparatively weak emission in solution. This phenomenon has been denoted "aggregation induced emission" (AIE) and is the opposite to what is typically observed with organic molecules, in which fluorescence intensity decreases with aggregation as a result of greater intermolecular π-π overlap quenching excited states (aggregation caused quenching, ACQ). However, for molecules which possess one or more fluorophores attached via rotatable single bonds, such as the bromophenyl groups on Br-FN, the rotation of these bonds causes excited states to annihilate non-radiatively. In a dilute solution with little to no aggregation, there are no restrictions on torsional movement and the molecule is rendered non-luminescent. In the solid state, the physical constraint of bond movement can therefore block the non-radiative decay channel, and activate fluorescence[32].

The extent of π-π overlap between neighbouring aromatic rings is determined by both distance and the angle between them, with parallel rings causing maximal overlap[78]. In the crystal structure of crystals of Br-FN formed from solution growth (henceforth denoted form 1), there are two conformationally identical molecules which are rotated around a central axis by 180 ° relative to each other (figure 3.1b). The phenyl rings of each molecule are twisted with respect to each other and near-perpendicular with an angle of 97.82° between the mean planes calculated through the carbon atoms of the phenyl rings and a (phenyl)C-C=C-C(N) torsion angle of ~ 8°. The cyano groups force the aromatic rings out of plane, preventing intermolecular π-π stacking as the planes of aromatic rings in neighbouring molecules lie at 82.18° relative to each other (figure 3.1c). This therefore reduces the probability of the transfer of excited states between adjacent fluorophores and inhibits loss of fluorescent photons in two principle ways. If transfer occurs from an excited host molecule to an

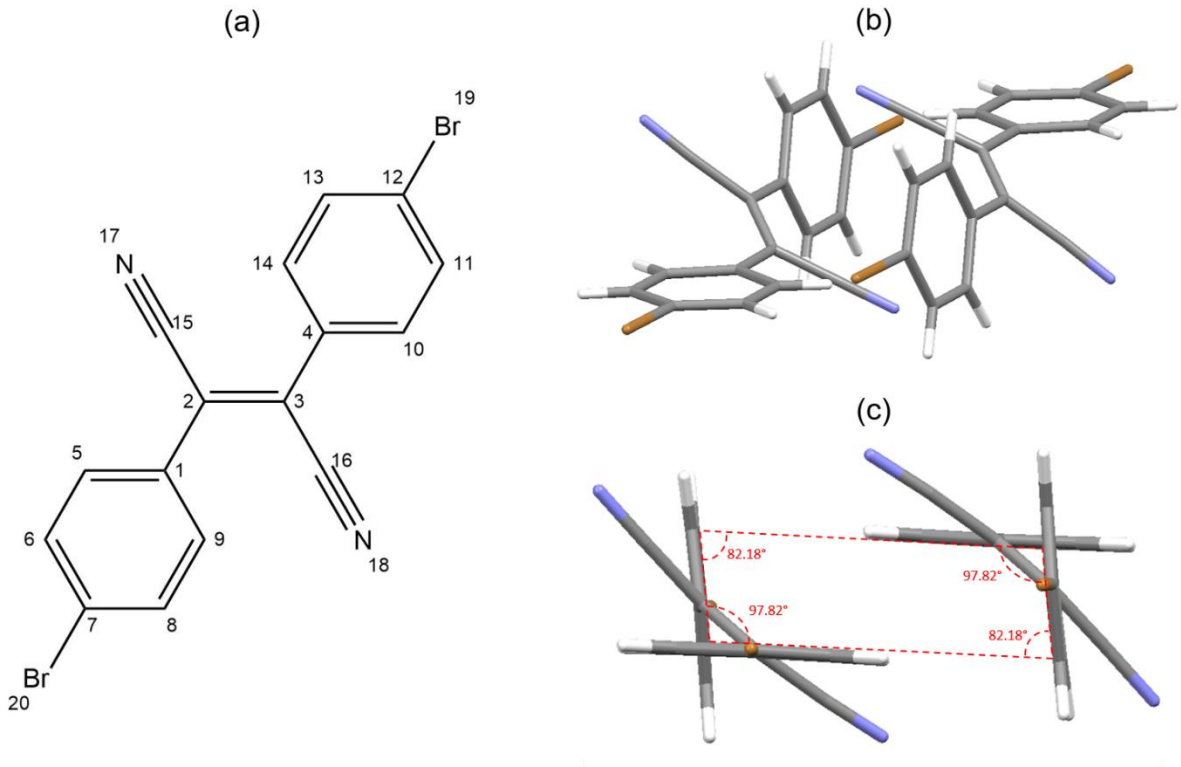

Figure 3.1: a) Chemical structure of BrFN with numbered atoms. b) The unit cell of BrFN form 1, which contains two molecules. c) The unit cell as viewed down the long axis of each molecule with angles between aromatic rings.

adjacent guest molecule which is also in an excited state, singlet-singlet annihilation may happen in which the transferred energy from the host molecule promotes the guest molecule from a state S_1 to a higher state S_n. The guest then rapidly decays non-radiatively back to S_1, resulting in loss of excited state and therefore reducing quenching. The second is the formation of excimers, excited states delocalised over two molecules which quench fluorescent photons due to their wide absorption bands[4]. Without these quenching mechanisms, quantum efficiency of fluorescence is greater, and crystals visibly fluoresce more intensely under exposure to UV light when compared to those which do not exhibit AIE[32]. Prior to this research, form 1 was the only documented polymorph of Br-FN in the Cambridge Crystallographic Data Centre (CCDC), with crystals having been exclusively grown via solution-based methods[58, 79].

3.2 Results and Discussion

3.2.1 A new polymorph of Bis(4-bromophenyl)fumaronitrile

Growth of Br-FN crystals was performed via PVT in order to produce crystals of sufficient size and quality to examine its fluorescence properties. In doing so, two distinct growth regions appeared in the PVT growth tube: an area with yellow-green needles (figure 3.2c, d) closest to the Br-FN growth powder which itself was placed at the hottest area of the tube at the centre of the furnace, followed by an area of translucent white block-like crystals similar to those grown from solution (figure 3.2a, b) at lower temperature, with a clearly defined

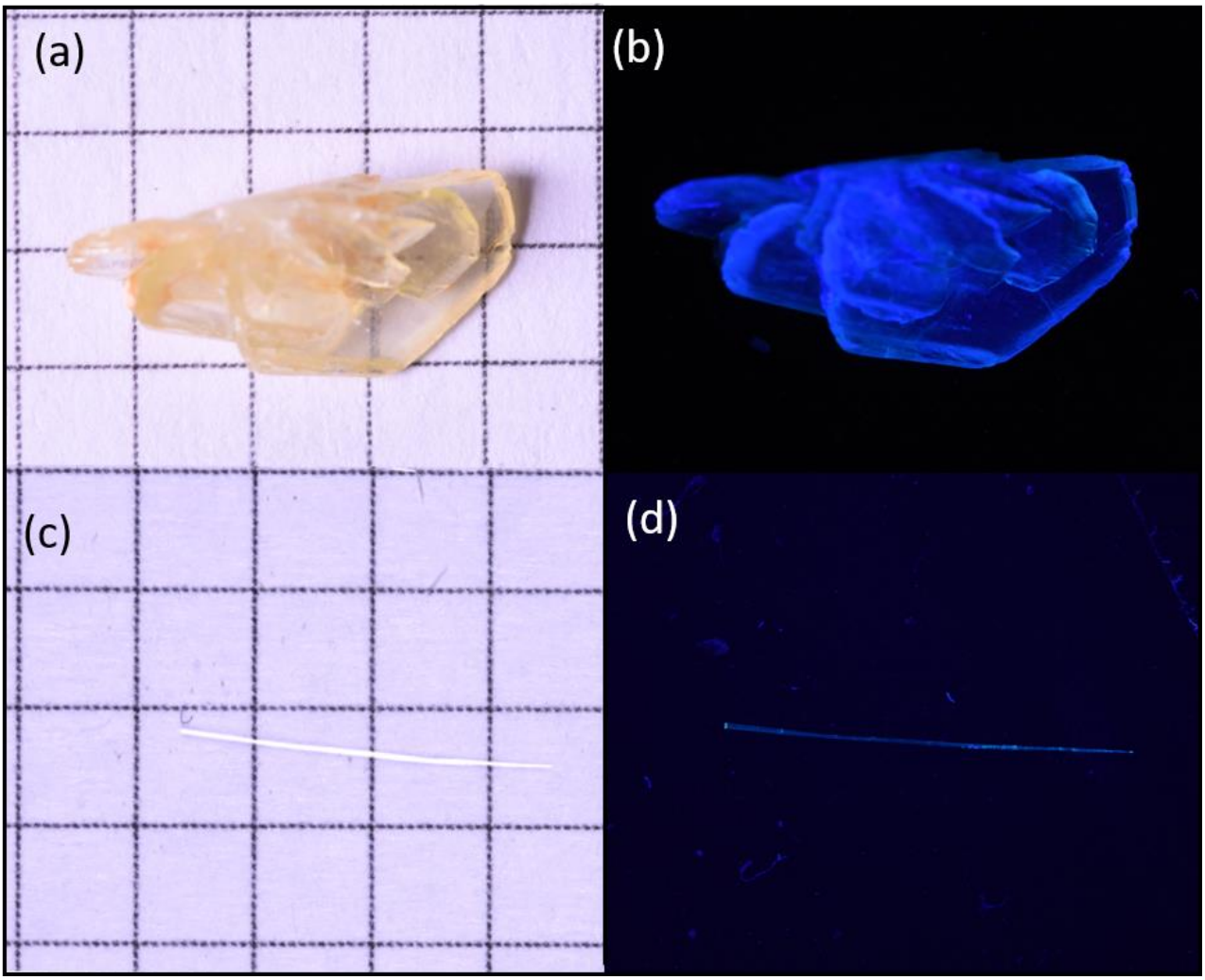

Figure 3.2: Top row: Form 1 crystals grown from solution under a) lab light and b) 365 nm UV light. Bottom row: Form 2 crystal under c) laboratory light and d) 365 nm UV light. Squares are 5 mm ^{2}.

transition between the two regions (figure 3.3). The first region appears between 120 and 140 mm from the centre of the furnace, which was at a temperature range of 214 to 204 °C during growth. The second region is 140 to 200 mm from the furnace centre, which was between 204 and 168 °C during growth (figure 3.4). These growth regions were consistent as the carrier gas flow rate was varied between 0.1 and 0.6 L/ min, indicating that the glass tube substrate that the crystals are forming upon is affecting the colour and shape of the crystals. Under exposure to 365 nm UV light, the yellow crystals in zone 1 exhibit blue-green fluorescence, in contrast to the comparatively intense blue fluorescence from zone 2.

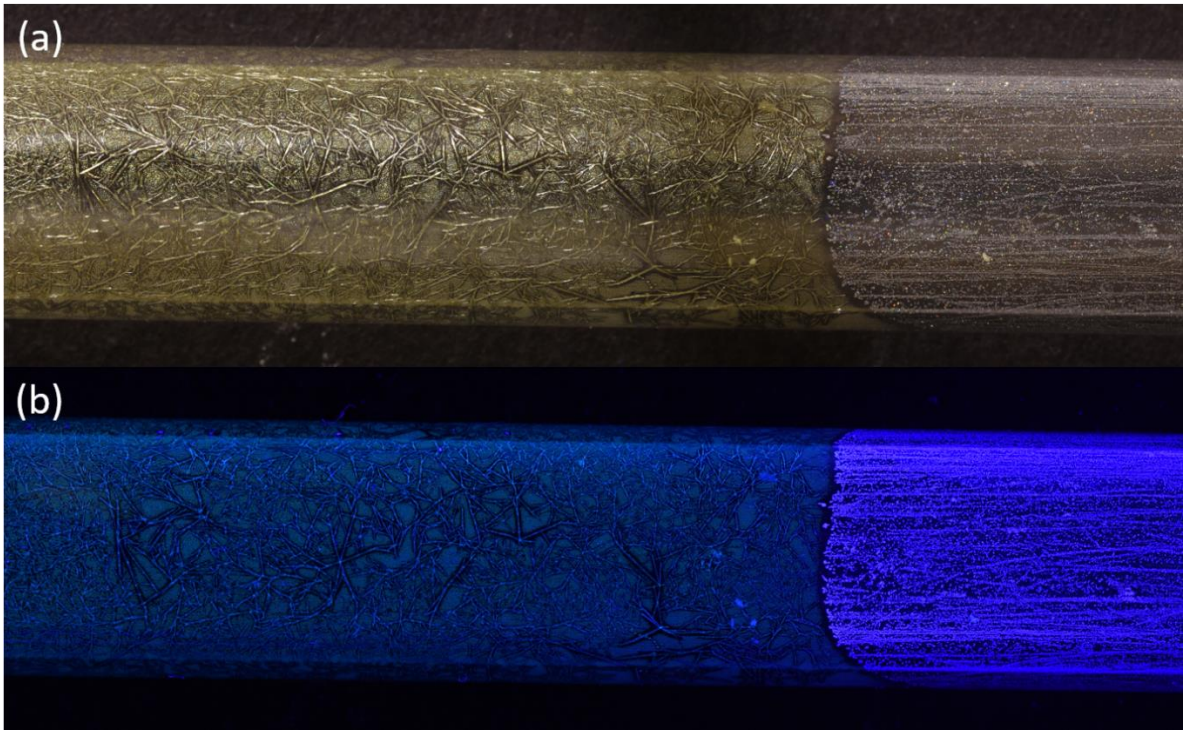

Figure 3.3: A picture of a glass tube used in the PVT growth of Br-FN showing the transition between growth zones, a) under laboratory light and b) under 365 nm UV light.

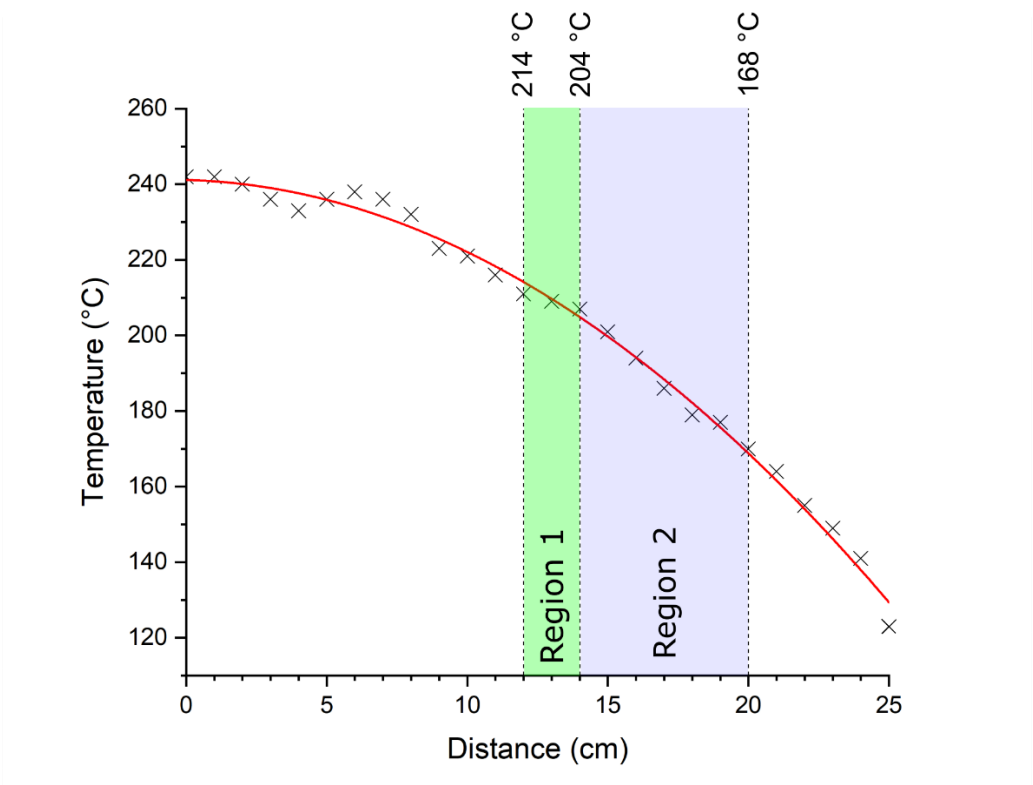

Figure 3.4: The temperature profile of the PVT growth tube in the furnace, from the centre of the furnace (0 cm) to the end of the tube (25 cm). Black crosses are experimentally measured temperatures (section 2.1.4.1), red line is a polynomial fit to the data. The regions in the tube of the two growth zones are indicated.

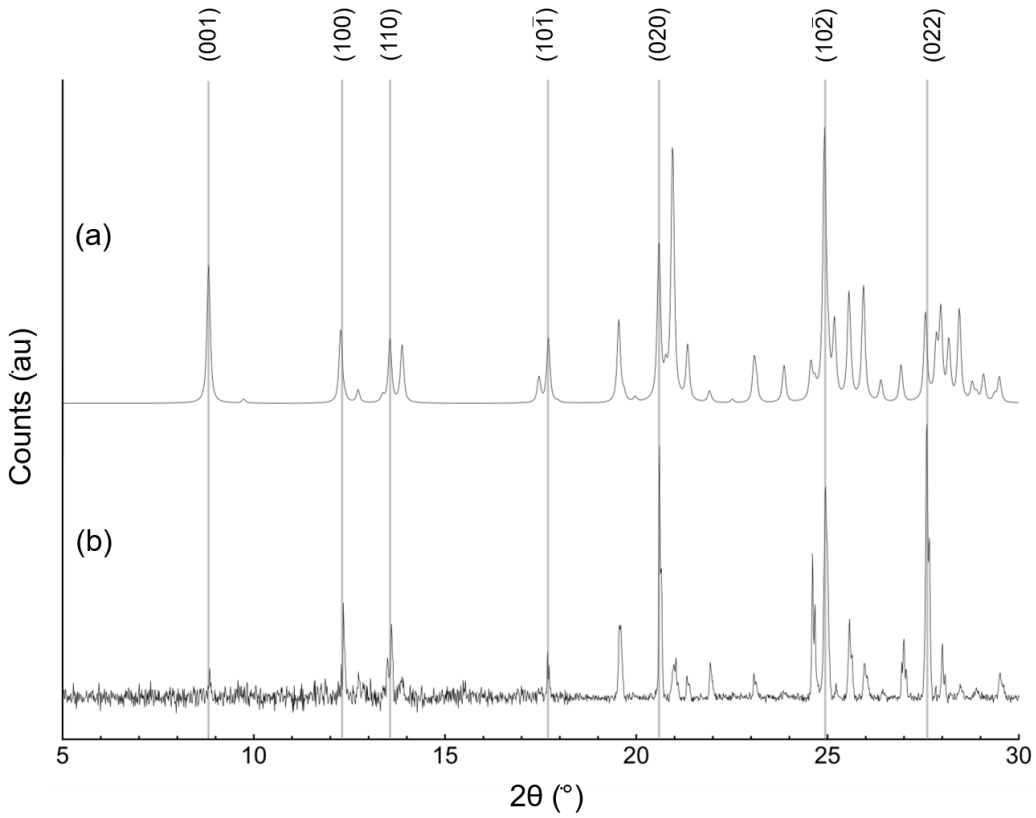

Figure 3.5: a) A ideal powder pattern generated from the crystallographic information file of the form 1 unit cell. b) pXRD data of crystals extracted from region 1. Major reflections labelled. All peaks from pXRD data match the target phase.

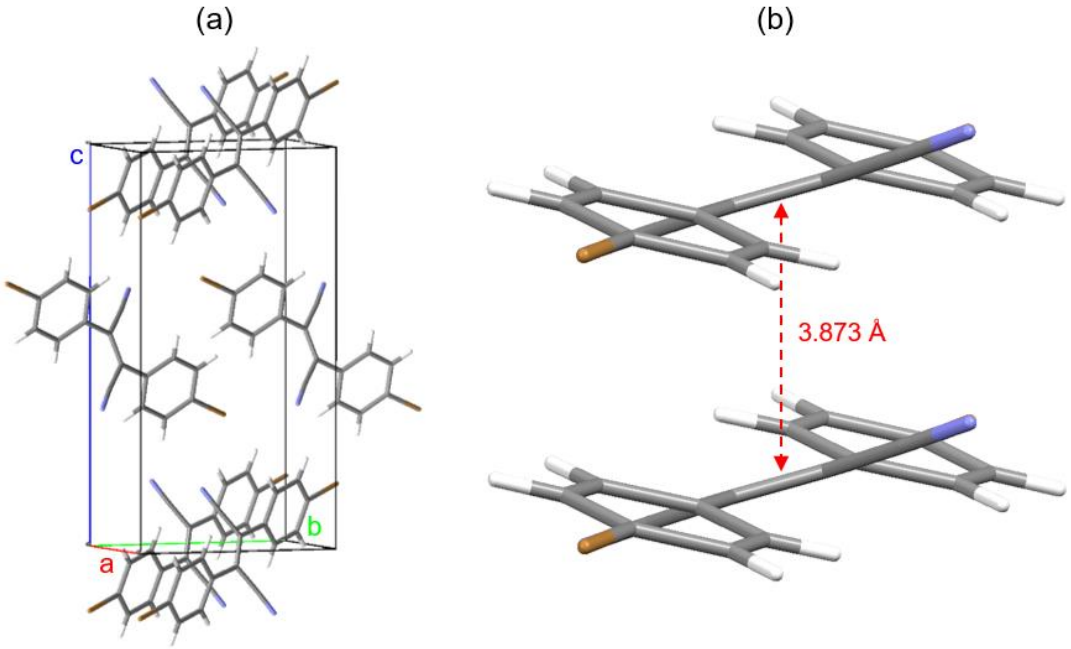

Figure 3.6: a) The unit cell of form 2 Br-FN crystals b) Stacking configuration of Br-FN molecules in form 2 down the a-axis.

	Form 1	Form 2
Crystal system	Triclinic	Triclinic
Space group	P -1	P -1
a/Å	7.9926(9)	3.87260(10)
b/Å	9.4626(12)	10.7671(4)
c/Å	10.6914(15)	16.5188(6)
α/ Å	92.131(11)	90.217(3)
β/°	110.063(10)	93.186(3)
γ/°	74.017(10)	98.738(2)
Volume/Å^3	728.699	679.68(4)
Z	2	2
Temperature/ K	100	100

Table 3.1: Unit cell parameters of form 1 and form 2 of Br-FN

Comparisons between the powder pattern extracted from SC-XRD data of solvent-grown crystals, and pXRD data of the crystals extracted from zone 2 exhibited peaks in the same 2θ positions, indicating that crystals from zone 2 possess the same crystal structure as those grown via solution-based methods. A systematic shift of the measured pattern to lower 2θ by 0.02° relative to the single crystal data was accounted for, which occurs as single crystal measurements were taken at a temperature of 100K, resulting in slight contraction of the unit cell (figure 3.5). Single-crystal XRD on the green rod-like crystals from zone 2 revealed an entirely different crystal structure distinct from the known form (figure 3.6). This structure also possesses a space group of P -1, but has contrasting lattice parameters (table 3.1): whereas the axis lengths of the known form are similar in magnitude, the *a*-axis of the unit cell in the zone 2 crystals is far shorter than the *b* and *c*-axis, resulting in a smaller unit cell volume. This new polymorph contains two molecules in the unit cell (Z = 2) but the asymmetric unit consists of two half molecules (Z' = 2 x 0.5). It was found that this structure was an entirely new, undocumented polymorph of Br-FN, which is henceforth denoted form 2.

Form	Ring 1	Ring 2	Centroid-centroid distance (Å)	Offset distance (Å)
1	C1-C6	C1^1-C6^1	3.70	1.50
	C9-C14	C9^2-C14^2	4.07	1.25
2	C1-C6	C1^3-C6^3	3.87	1.39
	C1-C6	C1^4-C6^4	3.87	1.39
	C9-C14	C9^3-C14^3	3.87	1.64
	C9-C14	C9^4-C14^4	3.87	1.64

^{1} = - *x*, 1-*y*, -*z*, ^{2} = 1-*x*, -*y*, 1-*z*, ^{3} = -1+*x*, +*y*, +*z*, ^{4} = 1+*x*, +*y*, +*z*

Table 3.2: π-π stacking distances

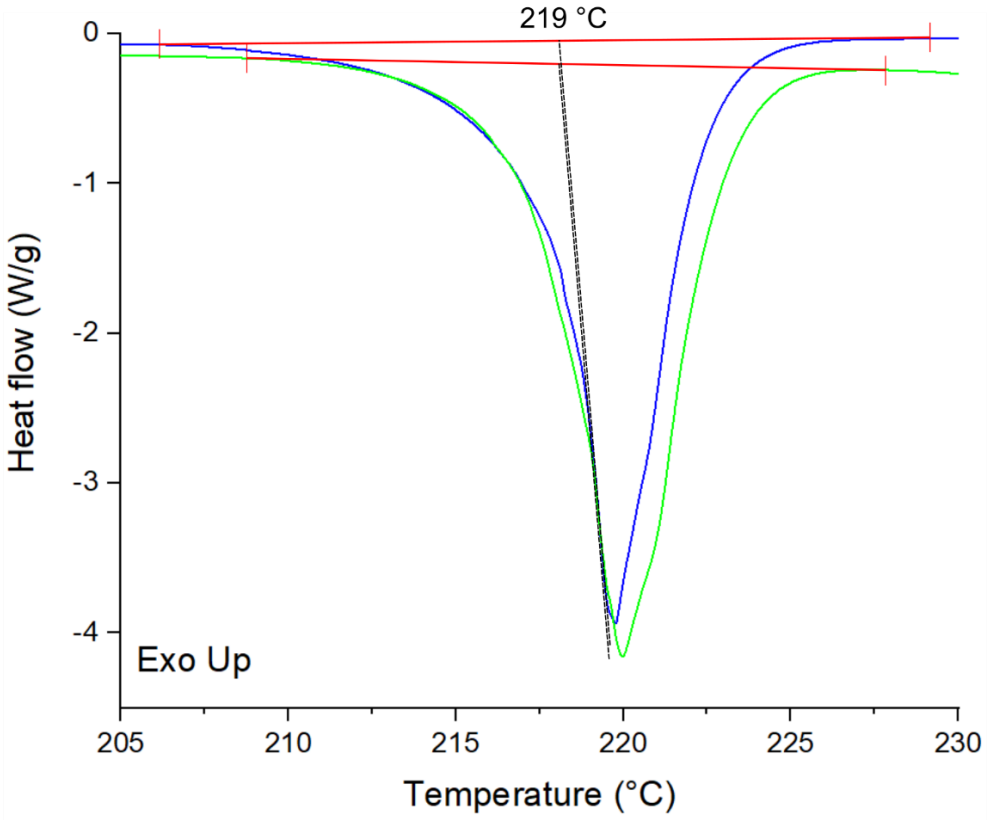

Figure 3.7: DSC data of form 1 (blue line) and form 2 (green line) from heating between 190 °C and 240 °C.

Comparisons between the two forms reveal a starkly different molecular arrangement of Br-FN. In form 1, the phenyl rings of each molecule are twisted with respect to each other and near-perpendicular with an angle of 97.83° between the mean planes calculated through the carbon atoms of the phenyl rings and a (phenyl)C-C=C-C(N) torsion angle of ~ 8°, whereas in the new polymorph (form 2) the rings are parallel with (phenyl)C-C=C-C(N) torsion angles of ~2 / -2°. The Br-FN molecules are parallel down the short (*a*) axis with each atom separated by 3.873 Å. As a result, form 2 displays extensive intermolecular π-π stacking interactions (table 3.2). In form 1 each of the two phenyl rings form one π-π interaction to symmetry related phenyl rings on different molecules, creating chains through the structure in approximately the [101] direction. However, in form 2 the parallel orientation of the phenyl rings with respect to each other enables both phenyl rings on each unique molecule to interact with pairs of phenyl rings on parallel molecules above and below, creating π-π stacks in approximately the [100] direction (*a*-axis), which is aligned with the long axis of the needles. The layered structure is similar to those seen in other derivatives of diphenyl fumaronitriles, such as bis(4-methoxyphenyl)fumaronitrile[58], whereas the conventionally obtained structure, form 1, is distinctly nonplanar.

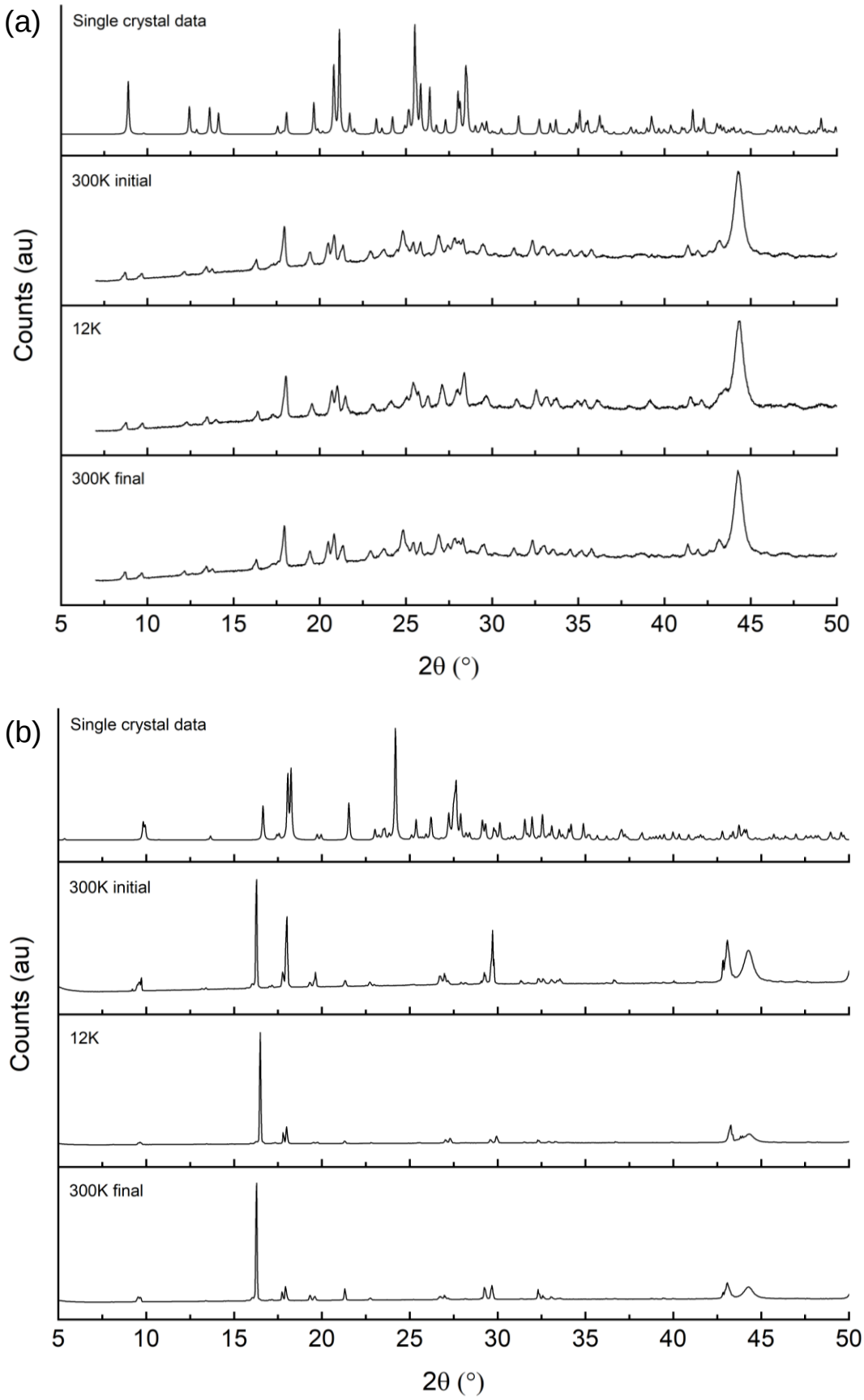

Figure 3.8: Low temperature pXRD of a) form 1 and b) form 2 crystals. From top to bottom: idealised powder pattern extracted from single crystal data, a pattern measured at 300K before cooling, a pattern measured at 12K and a pattern measured after heating back to 300K. All peaks match the respective target phase.

DSC analysis (figure 3.7) reveals that no phase change occurs between the two polymorphs over the temperature range of 300 K to their measured melting points of 492 K. The melting points of the two polymorphs were measured to be equal within error margins, therefore any difference in lattice energy is beyond the detection limits of the DSC apparatus. Low temperature pXRD performed on powder of form 1 and form 2 (figure 3.8) also indicate that there is no phase change between 300 K and 12 K, as the peak positions of patterns measured at 12K are similar to those measured at both 300K and a pattern extracted from single crystal data of each respective crystal. There is a slight peak shift to lower angles in the 300K patterns relative to the single crystal data which becomes less pronounced in the low-temperature measurements. This is due to contraction of the crystal lattice at low temperature. The pattern of form 2 taken at 12K has an intensified peak at 16° 2θ relative to the initial pattern taken at 300K. This discrepancy was retained as the powder was heated back to 300K. This is likely due to the shattering of crystallites upon cooling.

From the DSC and low-temperature pXRD data, it is evident that the polymorphs are monotropic in the temperature range 12 – 493 K. This would therefore suggest the presence of a large potential barrier separating the energy minima of each polymorph. The peaks were integrated to calculate the heat of melting of each polymorph. Form 1 requires 90.57 J/ g (35.14 kJ/ mol) to melt the crystal, whereas form 2 requires 97.97 J/ g (38.01 kJ/ mol), indicating that form 2 requires more energy to melt and is therefore the more stable of the two polymorphs. To further examine the relative stabilities of the two polymorphs, static (0 K) lattice energy values for both polymorphs were calculated via DFT. The values generated for form 1 and form 2 were -148.3 kJ/mol and -151.3 kJ/mol, respectively. This was confirmed by PBE-D3[80, 81] single-point energies on the HSE-3c structures, evaluated in a projector augmented plane wave basis set with energy cut-off of 800 eV with the VASP 5.4 code[82] yielding -150.2 kJ/mol for form 1 and -153.8 kJ/mol for form 2. The differences between the experimental and theoretical data arise as the energy required for complete separation of a molecule from the lattice is calculated (the heat of vaporisation) rather than the heat of melting. The accuracy of the HSE-3c functional is to within approximately 5 kJ/ mol for absolute lattice energies of organic compounds, so both polymorphic forms are equally stable within error values, with a slight tendency of form 2 to be more stable, agreeing with empirical data. Form 2 has a 20 kJ/mol higher stabilization from London dispersion forces making it competitive to form 1 and resulting in closer packing, evident in the smaller unit cell volume (Table 3.1). The similarity in lattice energies would explain how both polymorphs may form under similar growth conditions.

3.2.2 Crystal morphology

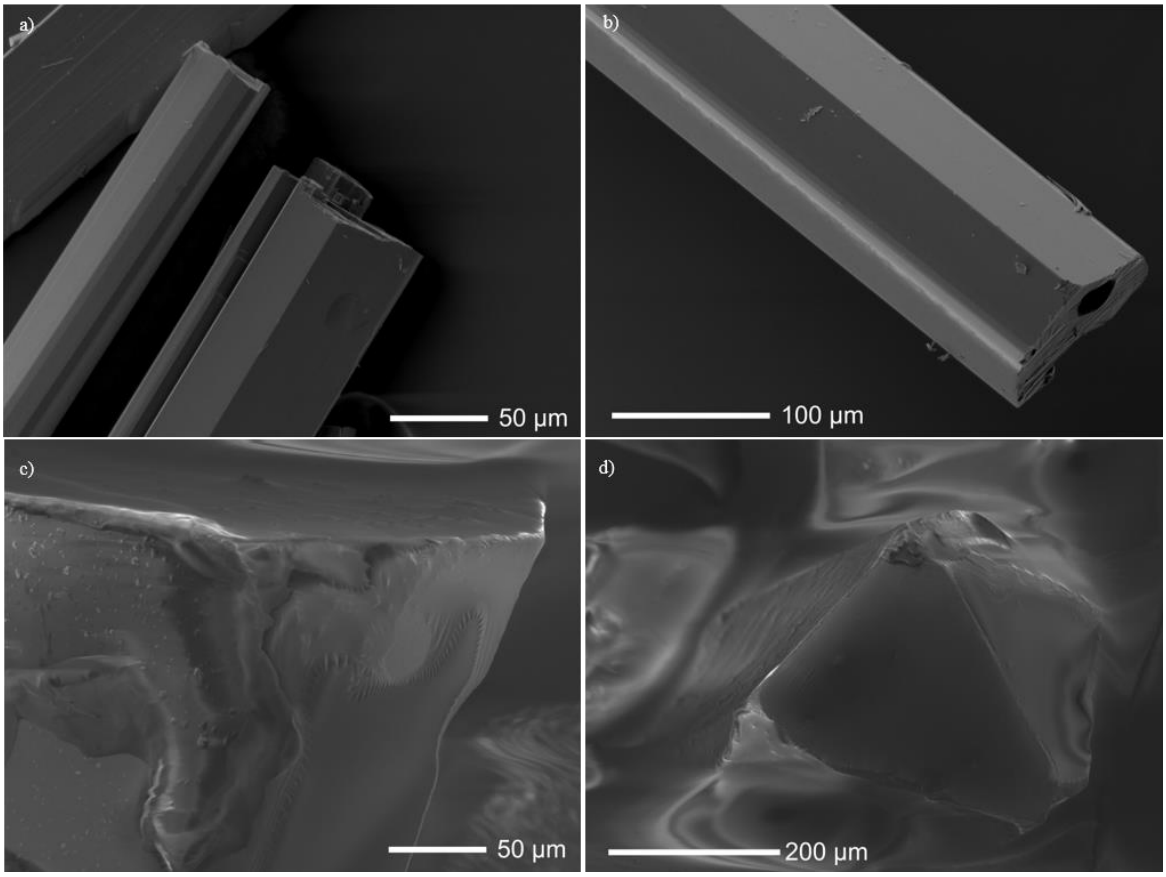

Figure 3.9: SEM images of PVT-grown Br-FN crystals (a, b) and solution-grown crystals (c, d)

Whilst solution-grown form 1 crystals are translucent and have a three-dimensional block-like morphology with rough, uneven faces observable under SEM, the PVT-grown form 2 crystals are thin rods between approximately 5 mm and 17 mm in length and 50 µm in diameter, with smooth, parallel faces (figure 3.9). The shape of the unit cell is often a reflection of the morphology of the bulk crystal. Bravais and Friedel noted that the distance between the centre of a crystal and a plane expressed on its surface was inversely proportional to the plane spacing, due to the greater ease of adding thinner planes to the crystal lattice[83]. Given the much shorter length of the *a*-axis compared with the b- and c-axes in form 2 (table 3.1), it therefore stands to reason that form 2 would grow into prismatic crystals with the *a*-axis forming the long axis of the crystal, which was confirmed in the SC-XRD data analysis. The unit cell parameters of form 1 are closer in value, resulting in all axes being expressed approximately equally and encouraging a three-dimensional block-like morphology. Simulations were performed using the Bravais-Friedel-Donnay-Harker (BFDH) method, which predicts the growth rates of different crystallographic planes based on lattice parameters of the unit cell and the symmetry operator information, and therefore the resulting shape of the crystal[84, 85]. These simulations accurately predict the block-like and rod-like morphology for form 1 and 2 respectively (figure 3.10).

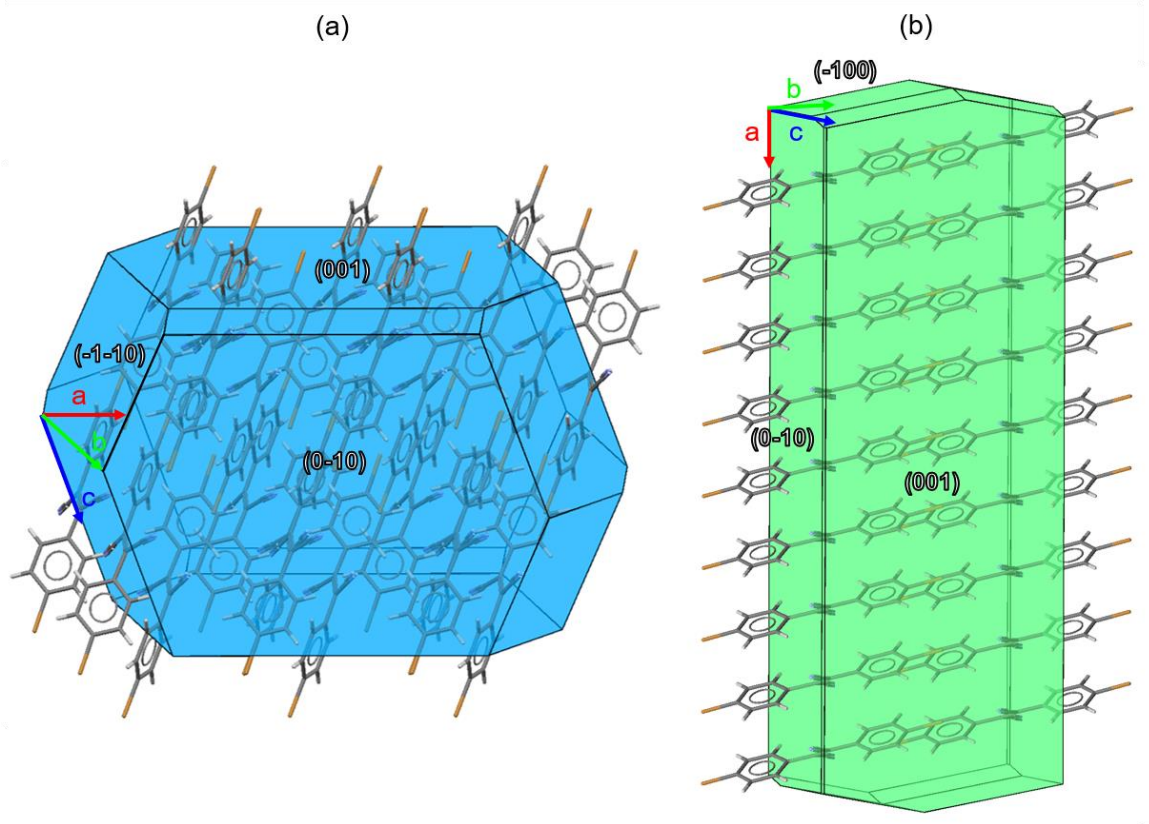

Figure 3.10: Predicted morphologies of a) form 1 and b) form 2 Br-FN crystals using the BFDH method, with unit cell axis directions and the planes of prominent faces labelled.

3.2.3 Polymorphism and Fluorescence

Fluorescence excitation and emission measurements were carried out on crystals of form 1 and form 2 (figure 3.11). Form 1 has a broad excitation spectrum with a maximum at 328 nm, and approximately retains excitation intensity down to 350 nm, at which point there is a near-linear decrease until 308 nm, with a further region of even intensity before a sharp drop-off at 280 nm. The two regions in which the intensity remains approximately similar may be ascribed to excitations of electrons from the S_0 (ground) state to the S_1 and S_2 states and their associated vibronic bands. The fluorescence spectrum exhibits a single, broad peak archetypal of organic crystals as excited states relax to the lowest vibronic band of the S_1 excited state before decaying to a band in the S_0 state (section 1.2.5). The fluorescence from crystals of form 2 was less intense than form 1, resulting in an excitation and emission spectrum with greater noise. There is a maximum centred on 425 nm in the excitation spectrum, with a sharp drop-off as the excitation wavelength is lowered until 375 nm, at which point the intensity increases until 330 nm, with a region of approximately equal excitation to the measurement limit of 250 nm. The features between 450 and 375 nm, and from 375 to 250 nm, may similarly be due to excitation to the S_1 band and the S_2 band respectively. The fluorescence spectrum has a single broad peak similar to form 1, but it is at higher wavelength and centred on 476 nm.

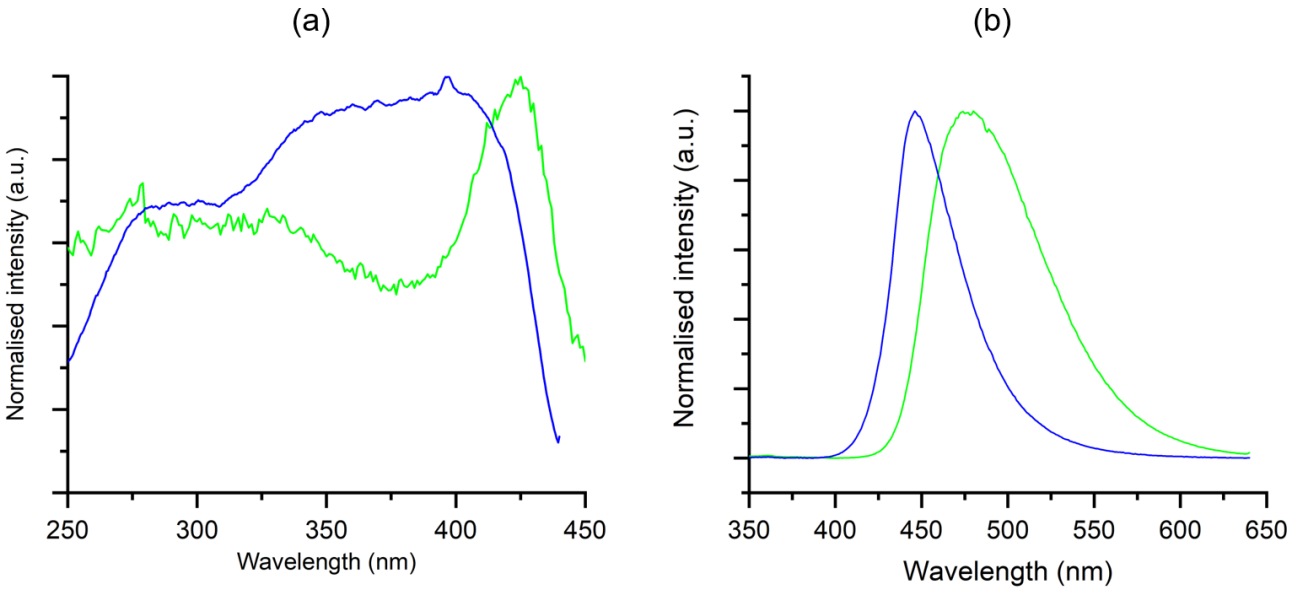

Figure 3.11: a) fluorescence excitation and b) fluorescence emission spectrum of form 1 (blue line) and form 2 (green line) Br-FN crystals. Form 1 emission measurements taken by exciting at 397.4 nm and excitation measurements by measuring emittance at 446.2 nm. Form 2 emission measurements taken with 425.3 nm excitation, and excitation measurements with 472.9 nm emission.

As described in section 3.1.3, Br-FN form 1 crystals exhibit intense fluorescence as the non-radiative decay pathways for excited states are suppressed due to little π-π overlap between adjacent molecules in the crystal lattice. Form 2 has a greater degree of intermolecular overlap of π-bonds due to the parallel stacks of aromatic rings which permeate the entire crystal lattice (figure 3.6). This therefore lowers the fluorescence intensity as mobile excited states are quenched due to singlet-singlet annihilation. The π-system of form 2 will also delocalise electrons over a greater area, reducing their energy. This is evident in the red-shifted emission relative to form 1. Another factor which will determine the delocalisation of electrons within a crystal lattice is the molecular conformation. Planarity is a requirement of conjugation, so a twisted conformation will isolate molecules to the molecular species on one side of the twist, increasing their confinement and therefore their energy. Forms 1 and 2 are conformational polymorphs, i.e. all molecules in each structure have the same intramolecular bond angles and may be substituted with any other molecule in its respective crystal lattice. In form 1 the aromatic rings are near-perpendicular, preventing conjugation across the entire molecule. In form 2, the rings are parallel allowing for delocalisation of charge carriers over the molecular structure (figure 3.12). This is reflected in calculations of the energy levels of the HOMO and LUMO of each molecular conformation (table 3.3), which show that the bandgap is of lower energy relative to form 1, resulting in red-shifted emission.

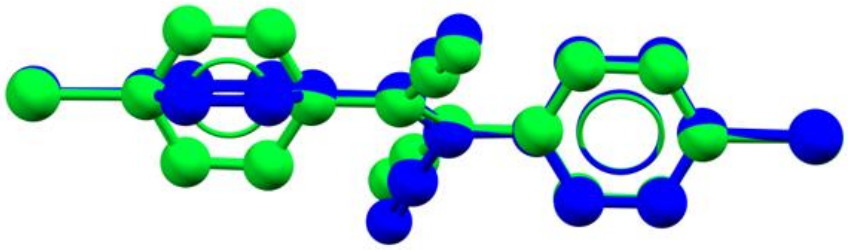

Figure 3.12: The confirmations adopted by Br-FN molecules in form 1 (blue) and form 2 (green) overlapped.

	Energy level (eV)	
	Form 1 conformation	Form 2 conformation
HOMO	-6.13	-3.69
LUMO	-3.74	-2.00
Bandgap	2.39	1.69

Table 3.3: Calculated energy levels of the molecular conformations of form 1 and 2 Br-FN crystals

3.2.4 Physical Vapour Transport and Polymorphism

From the regions of the growth tube in which each polymorph of Br-FN forms when growing crystals via PVT and the relative stabilities of each polymorph, it appears that a higher temperature substrate is causing the more stable polymorph to form. In order to further test the hypothesis, PVT was carried out in a furnace with three zones 20 cm apart which allowed for control of the temperature in each zone, such that the temperature of the growth region could be controlled independently of the temperature at which the Br-FN powder was sublimated. The temperature varies approximately linearly between the centre of each zone. A nitrogen gas flow of 0.1 L/ min was used to carry the Br-FN vapour to the lower temperature zones, where it crystallised (figure 3.13). In order to rule out the possibility that the fine structure on the surface of the glass growth tube was affecting which polymorph would form when performing the initial growth in the single-zone furnace, a different glass tube was used for these experiments. In the first instance, the sublimation zone temperature (zone 1) was set to 200 °C, zone 2 to 150 °C and zone 3 to 110 °C. Form 2 crystals grew exclusively between 7 and 13 cm from the sublimation zone, corresponding to glass tube temperatures of approximately 180 °C and 170 °C respectively. Form 1 crystals grew between 15 cm and 24 cm from the sublimation zone, corresponding to temperatures of approximately 165 °C and 140 °C. There was a 2 cm region between 13 and 15 cm from the sublimation zone in which both forms grew concomitantly. In the second instance, the sublimation zone temperature remained at

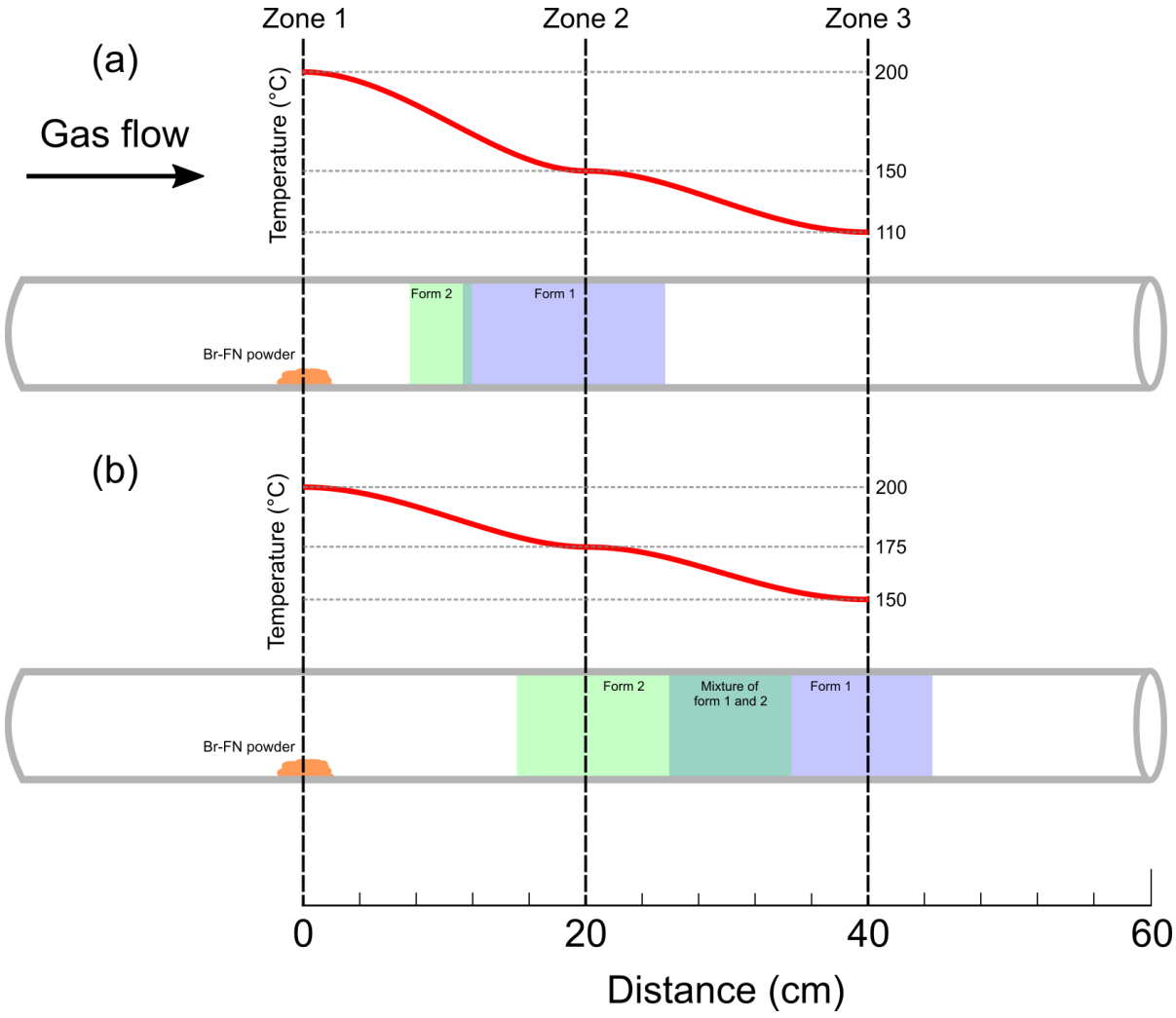

Figure 3.13: Regions of crystal growth when growing Br-FN via PVT in a three-zone furnace. a) Centre of each zone set to 200 °C, 150 °C and 110 °C. b) Centre of each zone set to 200 °C, 175 °C and 150 °C

200 °C but zones 1 and 2 were set to 175 °C and 150 °C respectively. This led to crystals forming further down the tube, with form 2 crystals between 16 cm (~180 °C) and 26 cm (~170 °C), and form 1 crystals between 36 cm (~155 °C) and 45 cm (~145 °C) from the sublimation zone. The concomitant growth region was much larger in this instance, with both polymorphs forming in a region between 25 cm (~170 °C) and 34 cm (~160 °C). In both instances, the more stable form 2 formed at higher temperature and the less stable form 1 at lower temperature, matching with what had been observed in the initial growth performed in a single-zone furnace. Furthermore, the temperatures at which each polymorph forms are similar in both single-zone and three-zone furnace experiments, indicating that the temperature of the substrate on which the crystal forms is the determining factor in which polymorph grows.

Similar conclusions were drawn from the PVT growth of the organic molecule 7,14-bis((trimethylsilyl)ethynyl)dibenzo[b,def]-chrysene (TMS-DBC), with the authors denoting a high temperature and low temperature polymorph based on the region of formation[75]. This was also observed in the vapour crystal growth of two thieno[3,2-b]thiophene-thiazolo[5,4-d]thiazole oligomers[86], with both exhibiting polymorphism

dependent on the temperature of the substrate. In the growth of 2,5-diphenyl1,4-distyrylbenzene, anthracene, tetracene and pentacene crystals by Wang et al (2014)[87], those that grew at higher temperature were found to show greater disorder, with lower temperatures producing higher quality crystals. It was therefore inferred that the high temperature glass substrate was introducing energy into the crystals as they form, causing the release of the binding energy of intermolecular interactions and disrupting the growth process such that perfect single crystals could not form. This was then further explored in the doping of tetracene molecules into anthracene crystals, in which the crystal lattice disturbance as a result of elevated temperatures allowed for greater incorporation of anthracene molecules into the tetracene lattice. It is therefore possible that high temperature substrates can alter the crystal lattice during growth. Shen et al (2018)[88] observed that the polymorph formed of 5-methoxy-salicylaldhyde azine could be controlled when grown via sublimation onto a quartz substrate by altering the temperature of the substrate. An orange polymorph would form exclusively at temperatures below 180 °C and a red polymorph at temperatures above 200 °C, with a mixture of both between 180 and 200 °C. DFT lattice energy calculations found that the orange polymorph was the most kinetically favourable polymorph, and the red polymorph was the more thermodynamically favourable. As the kinetically favourable polymorph is always first to grow (section 1.2.6), it was therefore speculated that the thermal energy introduced to the substrate above 200 °C was sufficient to overcome the potential barrier separating the two forms such that the more thermodynamically stable red polymorph could grow. Below this temperature, the orange polymorph grows and becomes locked into this form. This correlates with observations of the growth habits of Br-FN from the vapour, in which form 2, the polymorph measured to be the more stable of the two, is formed exclusively at a higher temperature than form 1 with a substrate temperature of approximately 170 °C or greater causing form 2 formation. It therefore stands to reason that this substrate temperature is sufficient to overcome the potential barrier between form 1 and 2, leading to a transition of crystal structure from form 1 to form 2 during growth.

3.3 Summary and Impact

Crystals of the molecule bis(4-bromophenyl)fumaronitrile were grown for the first time via PVT. This resulted in the crystallisation of both the conventional crystal structure and a novel polymorph which had been undocumented until this point. Crystals of this new polymorph have a rod-like morphology, in contrast to the block like morphology of the previously known form. The former exhibits weaker, red-shifted fluorescence when compared to the latter, due to possessing greater intermolecular π-π overlap and a conformation which enabled delocalisation of excited states over the entire molecule. DSC data and lattice energy calculations revealed the new form to be more stable than the known form. PVT carried out in a three-zone furnace conclusively proved that the temperature of the substrate that the crystal formed on was determining which polymorph would grow. It was theorised that a higher temperature substrate provides energy to the crystal during growth which will cause it to transition to a more stable form.

This research demonstrates that polymorphic selectivity within crystals grown via PVT is dependent on the thermodynamic stability of each polymorph and the kinetic regime within the growth apparatus. If a more thermodynamically stable structure of a crystal has been theoretically predicted but not grown, PVT may be a route to achieving growth of that structure. This analysis will therefore aid in the fabrication of desired forms of semiconducting crystals for with enhanced charge transport properties and fluorescence efficiencies for optoelectronic devices. This knowledge may also be applied to the growth of pharmaceutical crystals, in which the ability to consistently produce specific structures or produce new structures with desirable properties is highly sought after[89].

4 Chapter 4: The Nanostructural origin of Fluorescence in Karpatite

The work in this chapter was published in part in Nature Scientific Reports on the 29th August 2017[90].

Jason Potticary performed solvent crystallisation of coronene and SEM, pXRD and fluorescence measurements on coronene and karpatite crystals. I performed sublimation recrystallisation, carried out fluorescence measurements on resublimed material and developed the theory to the origins of optical properties of the crystals with assistance from Hall and Potticary.

4.1 Introduction

As has been established in the previous chapter, compositionally similar crystals may exhibit differing optical properties due to differences in the molecular ordering and conformation altering the emission and lifetimes of excited states. However, there is a case in which two crystals of similar composition and crystal structure exhibit visibly different luminescent properties. Crystals of the polyaromatic hydrocarbon coronene which can be readily prepared in the laboratory via standard crystallisation procedures (section 1.3) fluoresce green under excitation from short-wave UV light, whereas naturally forming crystals of coronene which are created as a result of geological processes fluoresce blue under the same conditions. Both are known to possess the γ-herringbone crystal structure of coronene[91], but differences lie in the micro-morphology of each. Whilst previous work has attributed the discrepancies in emissive behaviour to the role of impurities or crystalline defects[92], in this chapter it is established that it is in fact the result of the differences in the micro-morphology between the naturally and artificially formed crystals of coronene. Although it has been observed that crystals of 1,4-bis[2-(4-methylthienyl)]-2,3,5,6-tetra-fluorobenzene will emit differently depending on the direction along which the crystal was cleaved, this phenomenon was attributed to direction-specific emittance from different crystal planes and not to an alteration of the emissive properties of excited states caused by a change in crystal morphology[93]. This is the first reported case of morphology altering the fundamental optical properties of an organic crystal and elucidates previously unexplained emissive behaviour in other similar systems.

4.1.1 Coronene

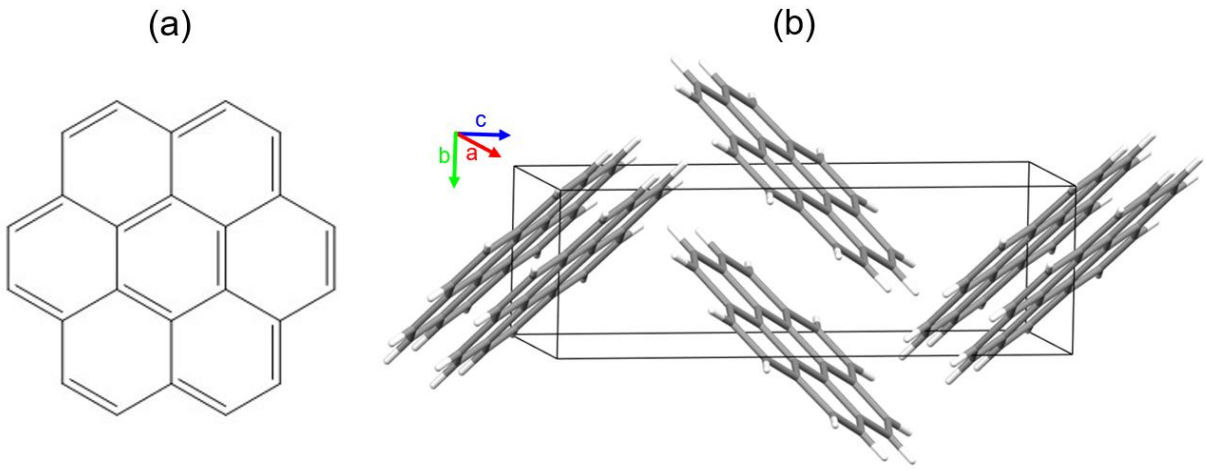

Figure 4.1: a) the chemical structure of coronene. b) the unit cell of γ-coronene

Coronene ($C_{24}H_{12}$) is a planar polyaromatic hydrocarbon composed of six aromatic rings in a hexagonal arrangement, resulting in a seventh ring at its centre (figure 4.1a). Each exposed carbon atom on the periphery of the molecule is bonded to a hydrogen atom. It possesses a fully conjugated π system which delocalises electrons over the entire structure, giving it high stability. As a result, it has been given the secondary title of "superbenzene" although this term is highly debated[94]. It forms naturally in combustion processes, particularly under low-oxygen conditions such as car engines[95], and can be extracted from crude oil deposits[96]. The most common source of coronene for its study is from commercial laboratory synthesis, as it can be synthesised to high purity and yield at large scale[97].

Crystal system	Triclinic
Space group	$P2_1/n$
a/Å	10.122
b/Å	4.694
c/Å	15.718
α/ Å	90
β/°	106.02
γ/°	90
Volume/Å³	702.073
Z	2

Table 4.1: Unit cell parameters of γ coronene

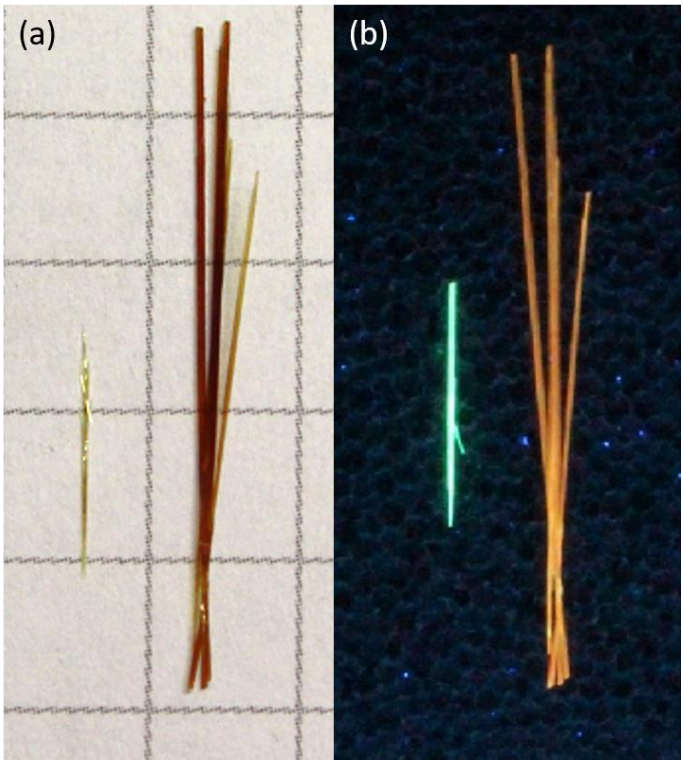

Figure 4.2: γ-coronene (left) and β-coronene (right) crystals under a) laboratory and b) short-wave UV light. Squares are 5 mm^2. Reproduced from ref [98].

Crystals of coronene from commercially available sources can be readily grown in the laboratory via the solvent cooling method from toluene. This produces needle-like crystals which are yellow-green in appearance under standard laboratory light. Similar to other polyaromatic hydrocarbons[99], coronene exhibits bright fluorescence in the crystalline state, appearing green under excitation from short-wave UV light. The unit cell of the crystal structure is comprised of two complete molecules, with molecules arranged in a herringbone structure (figure 4.1b). There is limited π-stacking down the *b*-axis of the unit cell. This structure has been denoted "γ-coronene" due to it falling within the γ-herringbone class of crystal structures according to Desiraju and Gavezzotti's naming conventions[100]. A second polymorph called β-coronene which is of the β-herringbone class has recently been documented and forms when crystals are grown under a 1T magnetic field or via cooling below 158 K (figure 4.2). This new structure is red in appearance and exhibits red-shifted fluorescence as a result of charge-transfer excitons which form due to close molecular packing[98,101].

4.1.2 Karpatite

Figure 4.3: Left: Karpatite crystals (green) within a quartz vein (white). Right: The same crystals under UV illumination.

Karpatite (also known as karpathite, carpatite, and pendletonite) is a rare mineral which is found in three regions globally: The Carpathian Mountains in Eastern Europe, Tamvatnei mercury deposit in far-east Russia and in San Benito County, CA. in the USA. It is found as bright yellow crystalline shards embedded in quartz (figure 4.3). It is an ultrapure form of crystalline coronene and forms due to the transport of coronene molecules by hydrothermal fluids. The high temperature of these fluids causes the depletion of lower-weight hydrocarbons due to their lower thermodynamic stability, purifying the crystals. Coronene in karpatite adopts the γ-herringbone polymorph[91]. However, unlike synthetically produced γ-coronene crystals, karpatite emits blue fluorescence under UV excitation. This distinctive difference in optical properties cannot be explained through positional or conformational differences of molecules in the unit cell. Therefore, an alternative explanation is necessary.

4.2 Composition and morphology of karpatite and lab-grown coronene crystals

4.2.1 X-ray diffraction and crystal structure

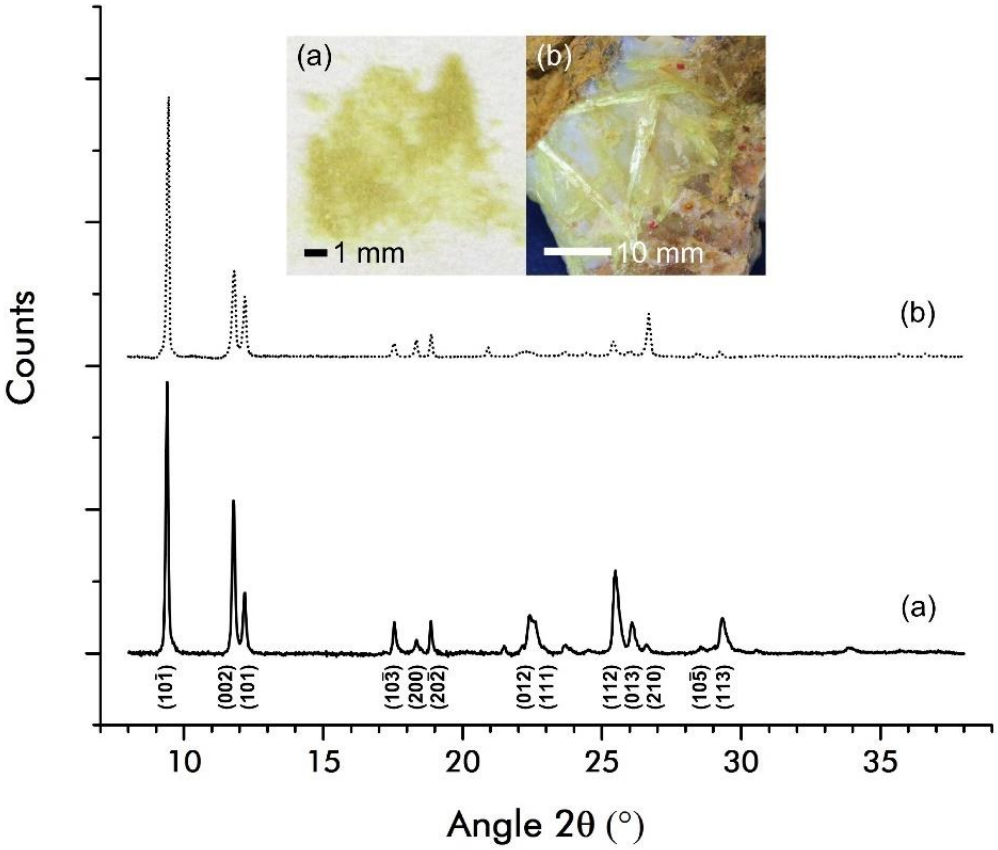

Figure 4.4: pXRD patterns of coronene (solid line) and karpatite (dotted line) crystals, with major reflections labelled. Insets: a) powdered recrystallised coronene and b) karpatite veins imbedded in quartz.

pXRD scans (figure 4.4) definitively show both the lab-grown coronene crystals (made from commercially acquired coronene twice-sublimed to remove impurities) and naturally formed karpatite veins to have a $P2_1/n$ space group, with plane reflection distances matching those of the γ-herringbone polymorph. These results match previous single-crystal data on karpatite crystals[102]. The crystals were crushed before measurement to ensure that all crystal planes were oriented as isotropically as possible. However, some preferential orientation is still present, evident by the overexpression of the peak associated (002) plane, caused by crystal fibres aligning with the sample holder substrate. No peaks associated with the presence of crystalline impurities are present. Furthermore, no wide amorphous bands are present in the pattern, indicating that the sample is entirely crystalline.

4.2.2 Scanning electron microscopy and micro-morphology

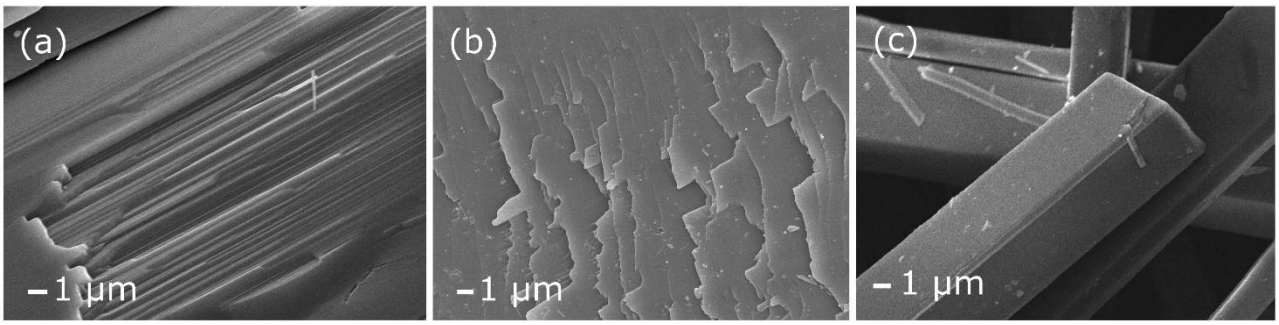

Figure 4.5: SEM images of a) the layered micro-structure on the surface of a karpatite crystal, and b) the exposed layering at the tip of the crystal. c) A lab-grown coronene crystal, taken at the same magnification.

Although compositionally identical, coronene and karpatite crystals possess significantly different micro-structure, which is visible via SEM. Karpatite is formed of layers approximately 100 nm in thickness which permeate through the entire structure (figure 4.5a, b). This is similar to the layers found in mica veins composed of silicate minerals, although these layers are typically much thicker than those found in karpatite, being typically on the order of 100 µm and visible to the naked eye[103].From the over- and under-expressed peaks from the powder pattern of karpatite crystals relative to a perfectly isotropically orientated sample, it was determined that the unit cell *c*-axis is perpendicular to the plane of the layers, and therefore the layers are approximately 60 unit cells thick (figure 4.6). This matches with previous research on karpatite which shows that it cleaves along the (100), (001) and ($\bar{2}$01) planes[104]. Lab-grown coronene crystals are needles approximately 2 µm thick and up to 5 mm long, with well-defined smooth surfaces which correspond to the (100), (010) and (001) planes (figure 4.5c). From SC-XRD data on lab-grown coronene crystals, it was found that the *b*-axis formed the long axis of the needles. The needles are therefore approximately 1200 unit cells along their shortest axis.

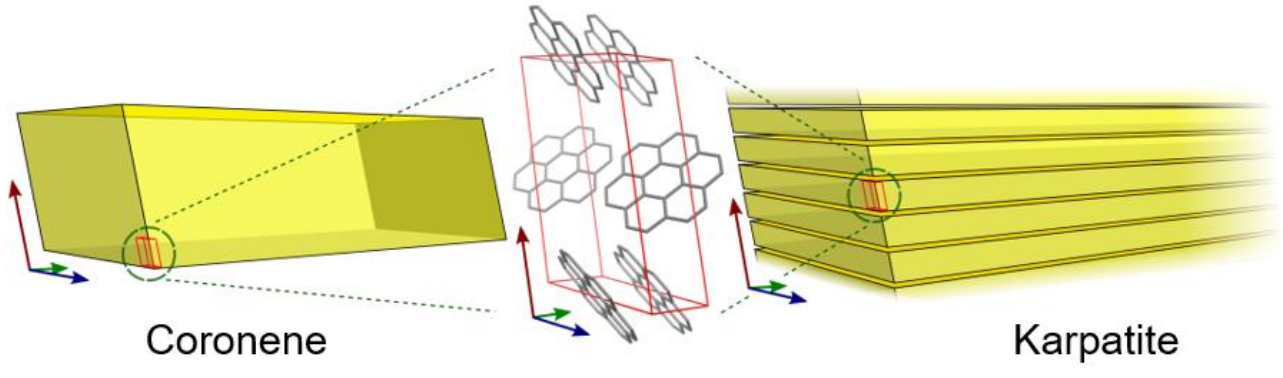

Figure 4.6: Schematic showing the orientation of the coronene unit cell within lab-grown coronene crystals and karpatite. Red, green and blue arrows are the a, b and c axes of the unit cell respectively.

4.3 Optical properties

4.3.1 Absorption and fluorescence of karpatite and lab-grown coronene crystals

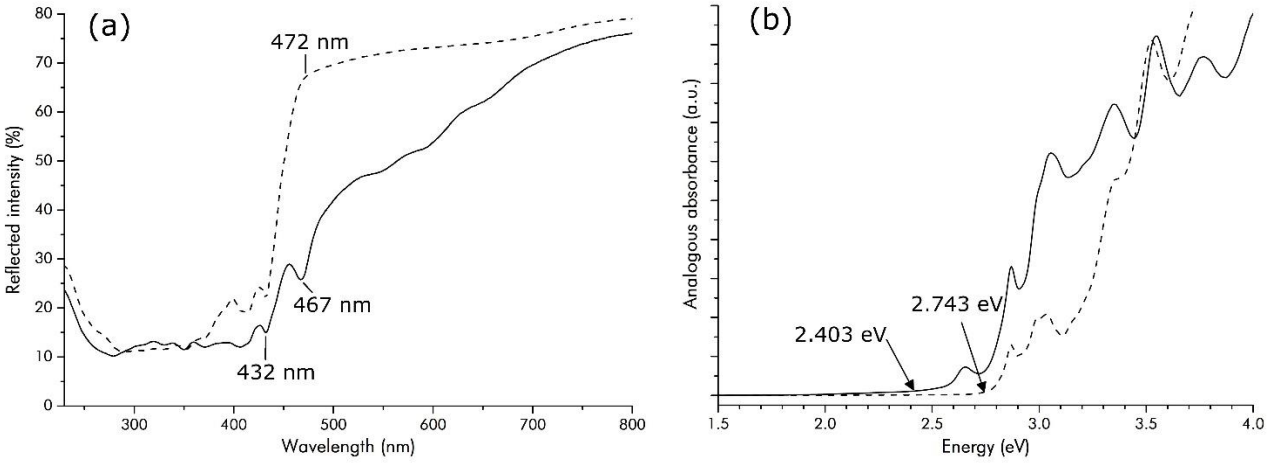

Figure 4.7: a) Diffuse reflectance absorption of lab-grown coronene crystals (solid line) and karpatite (dashed line) as measured by UV-Vis spectroscopy. b) Diffuse reflectance data as processed using the Kubelka-Munk function, showing lowest energy absorption.

The diffuse reflectance from lab-grown coronene crystals and karpatite were measured to determine their absorption spectra (figure 4.7a). The synthetic crystals exhibit a consistent increase in absorption with decreasing light wavelength until peaking at 467 nm and 432 nm, below which approximately 10% of light is reflected. Karpatite absorption increases gradually as wavelength is decreased until 472 nm, after which there is a sharp increase in absorption until 432 nm with a similar profile to lab-grown coronene crystals at lower wavelengths. The bandgap, as calculated from the onset of diffuse reflectance after procession by the Kubelka-Munk function (figure 4.7b), is 2.403 eV for coronene, close to the literature value of 2.41 eV[105]. The value measured for karpatite is higher at 2.743 eV.

Solid state fluorescence and excitation measurements were taken of coronene and karpatite crystals, displaying stark differences in peak positions and intensity profile (figure 4.8). Whilst both absorb to similar intensities from 360 nm to 420 nm, karpatite then peaks at 433 nm before decreasing sharply, with no absorption above 457 nm. Coronene peaks at 440 nm before decreasing in intensity gradually until 457 nm, followed by an intense peak centred at 466 nm and decreasing sharply up to the measurement limit at 500 nm. The fluorescence profiles are entirely dissimilar, with karpatite exhibiting one significant peak at 462.3 nm. Coronene's fluorescence spectrum has two major peaks in close proximity at 501.5 nm and 512.5 nm, with the 501.5 nm peak exhibiting a long tail to higher wavelengths.

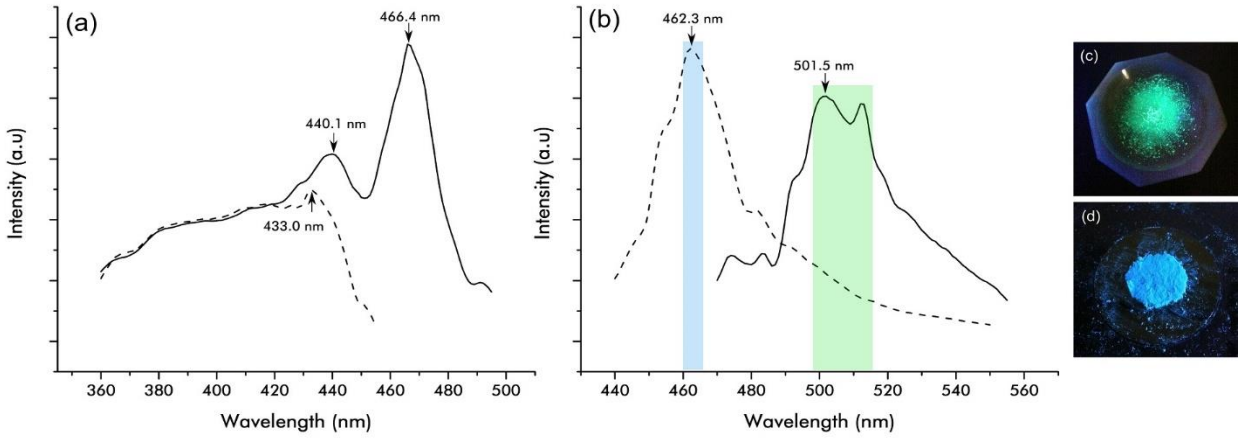

Figure 4.8: a) fluorescence excitation and b) emission spectra of karpatite dashed line) and coronene (solid line). c) Coronene crystals and d) karpatite crystals under 365 nm UV illumination. Coronene emission measurements taken by exciting at 466.4 nm and excitation measurements by measuring emittance at 501.5 nm. Karpatite emission measurements taken with 433 nm excitation, and excitation measurements with 462.3 nm emission.

4.3.2 Recrystallisation of karpatite

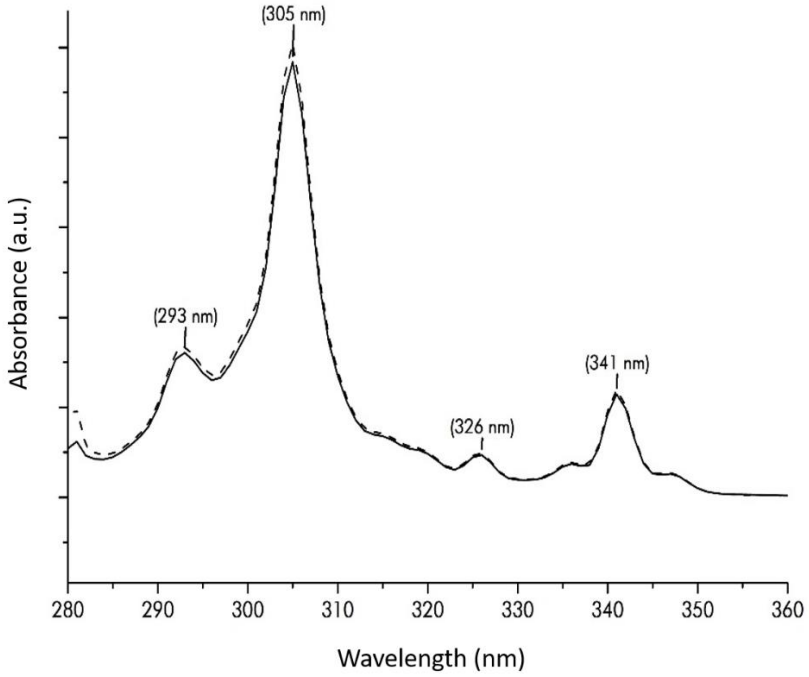

Figure 4.9: Absorption spectra of coronene (solid line) and karpatite (dashed line) dissolved in toluene

To confirm the compositional similarity of coronene and karpatite crystals and rule out the effects of impurities, they were each dissolved in toluene and the absorption spectrum from UV-Vis of the solutions was measured. The spectra are near-identical with peak positions matching those of the literature for coronene[106], exhibiting peaks at 293 nm, 305 nm, 326 nm and 341 nm (figure 4.9). Crystals were then grown from the solutions via slow evaporation. The crystals from the karpatite solution exhibited fluorescence excitation and emission

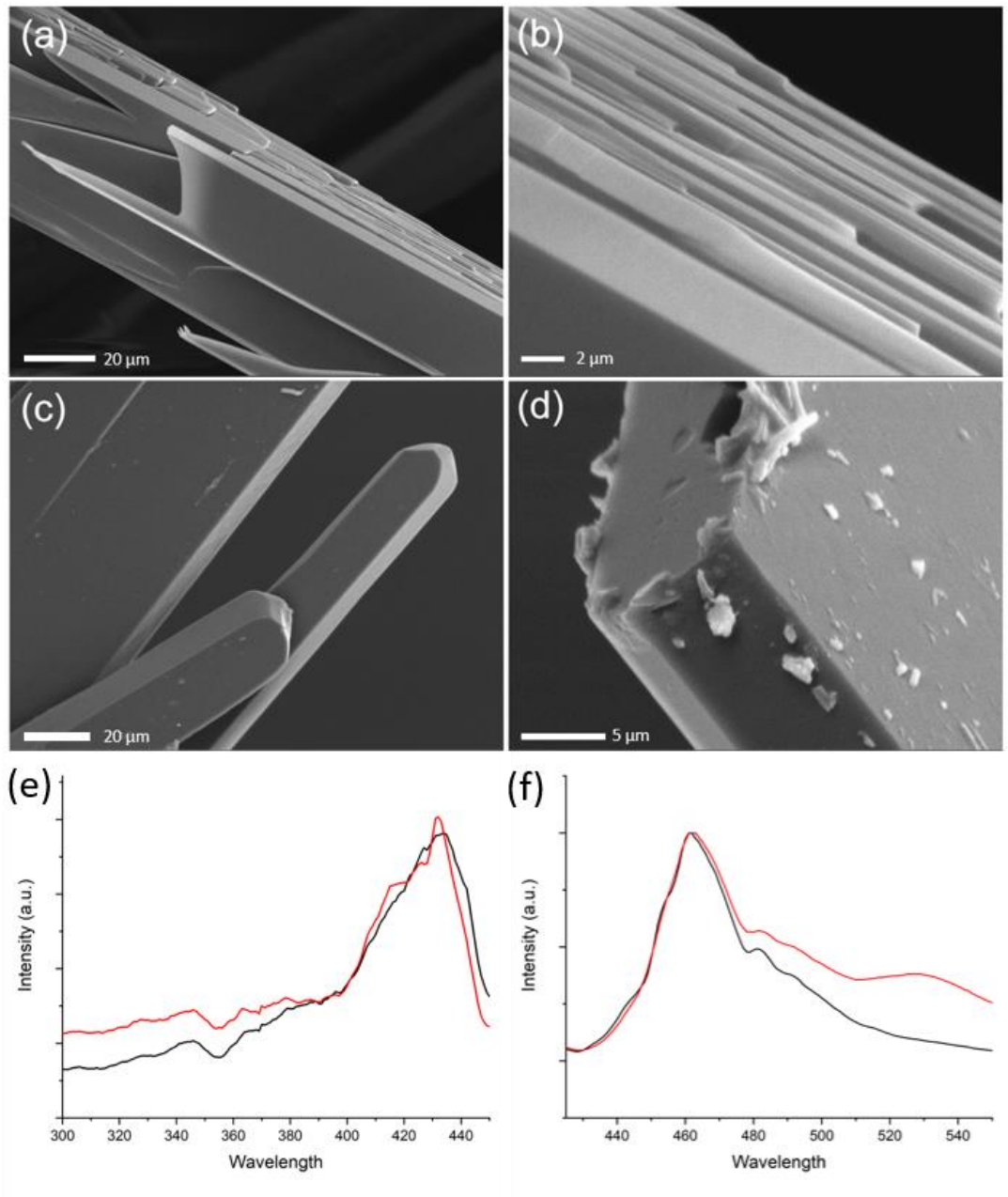

Figure 4.10: SEM images of sublimed karpatite crystals. Images (a) and (b) show texturing of the crystals, whereas (c) and (d) show no texturing. All crystals in this figure are from the same experiment. e) fluorescence excitation and f) emission profile of karpatite crystals before (black line) and after (red line) recrystallisation via sublimation.

spectra indistinguishable from lab-grown coronene. Recrystallisation was also performed via sublimation, which in addition acts as a purification method as impurities crystallise at different regions within the growth apparatus (section 1.3.2). This produced both crystals with a needle-like morphology and those with a layered structure (figure 4.10a-d). This resulted in an excitation (figure 4.10e) and fluorescence (figure 4.10f) spectrum with elements of both coronene and karpatite spectra: a peak at 462.3 nm similar to karpatite and heightened intensity between 480 nm and 550 similar to coronene. This therefore strongly suggests that morphology is the driving factor behind the disparity in optical properties.

4.3.3 Theories to the origins of fluorescence

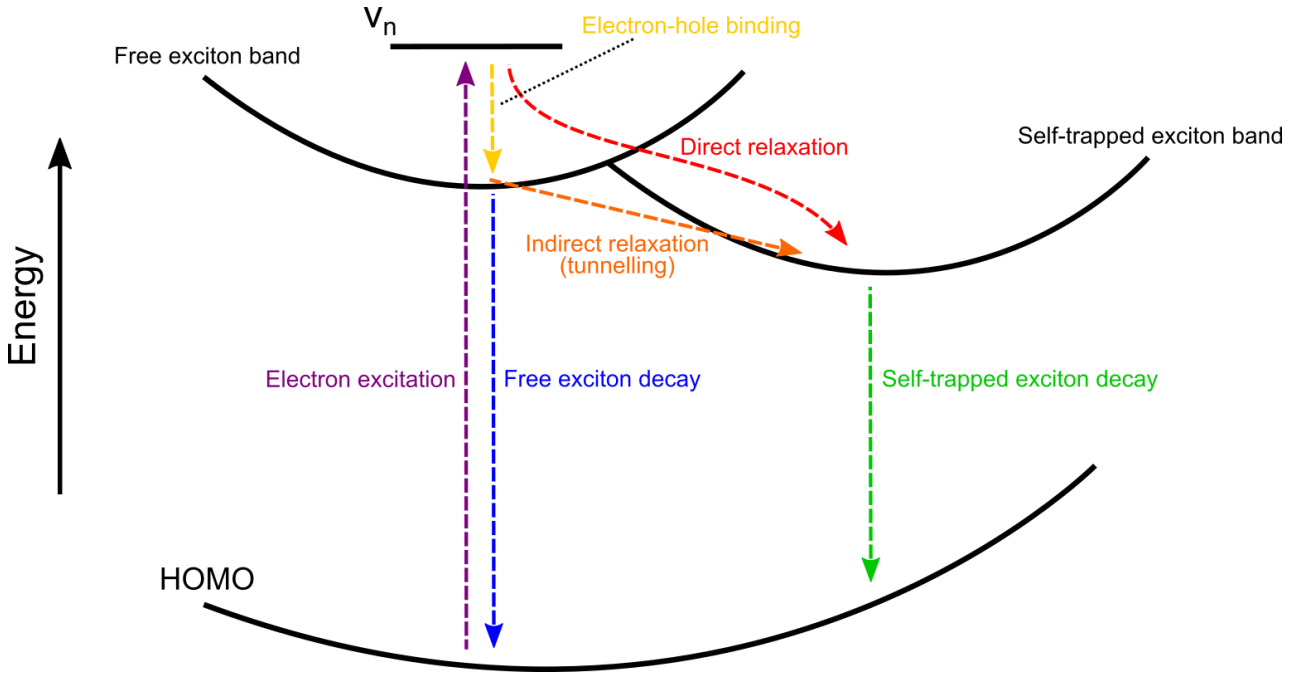

Figure 4.11: Schematic of radiative relaxation pathways for excitons in crystals with strong electron-phonon coupling

Previous fluorescence measurements of coronene crystals had been performed on thin, flake-like crystals of similar dimensions to individual layers of karpatite in order to ensure high crystal quality. These crystals all exhibited fluorescence profiles which match very closely with the fluorescence profile of karpatite[107,108]. In these cases, the dominant peak at 462 nm was attributed to the decay of self-trapped excitons. These excitons are coupled strongly to a distortion of the lattice confined to a single lattice site. This distortion is caused by the coupling of the exciton to the lattice, hence the name "self-trapped". As a result of this strong coupling, the energy of fluorescent photons emitted from the decay of a self-trapped exciton is affected by thermal fluctuations of the crystal lattice, resulting in broad emission bands red-shifted relative to the free exciton state[109]. On formation, an exciton will relax into either a free state uncoupled from the crystal lattice or the strongly coupled self-trapped state (figure 4.11). Emission from the former will cover a narrow range of wavelengths close to the bandgap of the material, as it is less stable than the latter and occupies an energy state nearer to the exciton band of the material. If the material possesses an electron-phonon coupling constant g greater than 1 (as is the case with coronene[110]) the self-trapped state will be more stable. In such systems, excitons may either decay directly to the self-trapped state or indirectly via the free state, tunnelling across the potential barrier. In the indirect case, exciton decay may occur from both states with both emission bands visible in the fluorescence spectrum[110].

The fluorescence profiles of millimetre-size α-perylene and pyrene crystals, both of which possess high electron-phonon coupling constants, exhibit broad, gaussian peaks which is due to the decay of self-trapped excitons. However, for crystals of sizes below 2 μm the self-trapped band is not present and there is a narrower peak at lower wavelength close to the $S_1 - S_0$ transition in its place, corresponding to the decay of free excitons[111]. It is clear that transition to the self-trapped state is suppressed as the crystal thickness is reduced. The minimum thickness of lab-grown coronene crystals is approximately 3.5 μm thick and they exhibit a fluorescence spectrum with a broad peak red-shifted relative to the bandgap. The crystalline layers of karpatite veins are less than 1 μm thick and have a narrow peak at 462 nm, close to the 452 nm wavelength of a photon emitted with equivalent energy to the bandgap measured for karpatite from UV-Vis (figure 4.7). The differences in fluorescence profile between the thinner karpatite layers and thicker lab-grown crystals are similar to those seen between bulk and micro-crystals of α-perylene and pyrene. The 462 nm peak dominant in the karpatite spectrum and in previously studied plate-like coronene crystals may therefore have been misattributed to the self-trapped exciton band due to coronene's high electron-phonon coupling constant[92]. The dependence of the free and self-trapped exciton bands in tetracene and N,N-dimethylaminobenzylidene 1,3-indandione on crystal size have also been demonstrated[112,113]. The reason that transition to the self-trapped states in confined systems is suppressed may be due to the differences in energy required to distort the crystal lattice by coupling to an exciton. In the bulk crystal, this distortion may be dissipated throughout the lattice and the self-trapped state is stable relative to the free state. However, with a limited number of lattice sites, the energy required to distort the lattice by coupling to the exciton may be greater than if it is unbound and thus the exciton will remain in the free state.

The fluorescence spectra of coronene nano-rods and micro-crystals of coronene have peaks at 500 nm, similar to bulk coronene crystals[114,115]. If the theory discussed in the previous paragraph were the origin of the difference in optical properties between lab-grown coronene crystals and karpatite, it would be expected that for crystals with at least one dimension below 1 μm this peak would not be present and only the 460 nm "free exciton" peak would be dominant. However, the only cases in which synthetically produced coronene crystals have featured the 460 nm peak without one at 500 nm are from thin plate-like crystals after extensive purification procedures[107] or from thin films[116]. The influence of impurities has been ruled out by the recrystallisation of karpatite which produced green-fluorescing crystals, so the differences between three-dimensional crystals and plates of thicknesses below 1 μm must be due to the exposed surface area relative to the bulk. The 500 nm peak has been ascribed to the decay of excimers, excitons in which the bound hole and electron occupy adjacent molecules. Excimers are delocalised over a greater area than monomer excitons, so their emission is red- shifted. The peak at 462 nm is thought to be due to excitons localised to a monomer, and so the emission will be higher energy[117] (figure 4.12). Both the dimer and monomer excitons are self-trapped by the lattice, causing red shifts of at least 30 nm from the 0-0 transition of a monomer at 428 nm[118]. From the fluorescence spectra it appears that monomer emission but not dimer emission is occurring from thin or layered structures, with the opposite true of bulk crystals. There are two peaks in the fluorescence excitation spectrum of bulk coronene: one at 440 nm close to

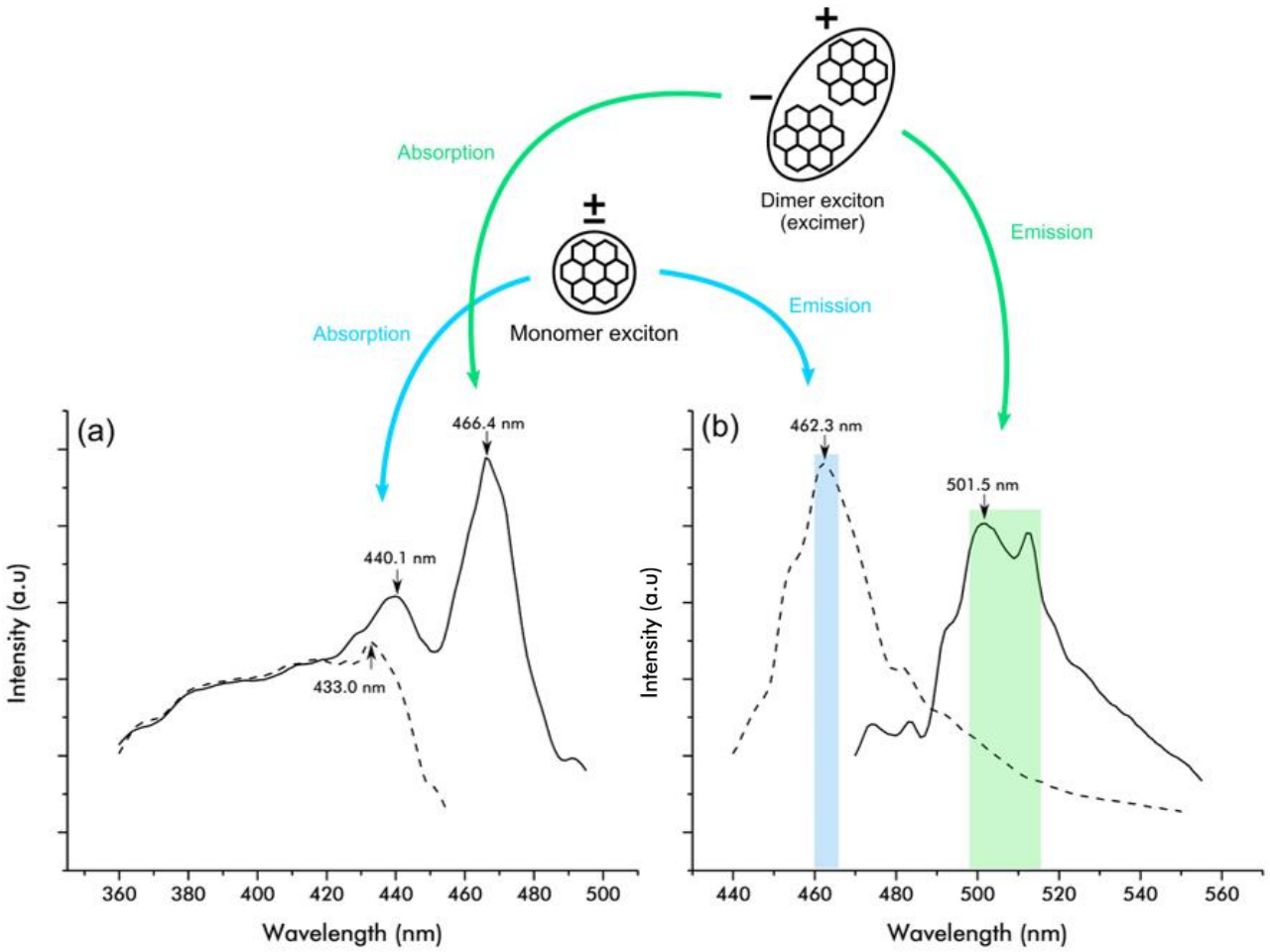

Figure 4.12: Potential origins of fluorescence a) excitation and b) emission peaks of coronene (solid line) and karpatite (dashed line).

the bandgap, and another larger peak at 462 nm. The 462 nm is of lower energy and is therefore likely due to the creation of excimers, with the 440 nm peak due to monomer excitons. However, the monomer emission peak in karpatite which occupies the same wavelength as the excimer excitation peak in bulk coronene implies that all monomer emission in the bulk is reabsorbed, and only excimer emission is observed. This matches with the UV-Vis absorption spectrum in which peaks are present at 432 nm and 467 nm (figure 4.7). The lack of an excimer excitation peak in karpatite from both fluorescence and UV-Vis measurements suggests that no excimers form upon excitation and thus only monomer emission is seen. This therefore indicates that monomer formation happens at the molecules on the surface of the layers where there are no adjacent molecules. Excimer formation is enhanced with π-stacking so it would be expected that excimer dimers would form along the *b*-axis of the unit cell which is the primary route for aromatic stacking (figure 4.6). However, the exposed face of karpatite is perpendicular to the *c*-axis, across which there is minimal intermolecular overlap of π-bonds. Although π-stacking encourages excimer formation, it has been shown in anthracene that this is not unique to a single crystallographic axis and excimers can form between any adjacent molecules[119]. An alternative theory is that excimer formation involves a distortion in the crystal lattice as the two molecules in the dimer are brought closer together[120]. For reasons mentioned for the coupling of excitons to the self-trapped state, this distortion

may only be favourable if there are a sufficient number of surrounding lattice sites. Further research is necessary to determine the nature of excimers in coronene, and the orientation of dimers in the crystal lattice. The origin of the 512.5 nm peak in the fluorescence spectrum of lab-grown coronene crystals is also unknown but is of similar energy to the bandgap measured from these crystals, suggesting this peak may be a result of the decay of non-trapped (free) excimers.

4.4 Summary and Impact

Differences in optical properties between coronene crystals grown in a laboratory and karpatite, a naturally forming mineral comprised of crystalline coronene, were investigated. pXRD showed that both crystal structures were of the γ-herringbone polymorph of coronene, with close agreement in peak positions. SEM revealed differences in the nano-texturing of synthetic coronene crystals and karpatite: the former are rods up to 5 mm in length and approximately 3 μm in height and width, with the latter formed of many crystalline layers between approximately 10 and 100 nm in thickness. UV-vis and fluorescence measurements showed that karpatite absorbs light to a maximum wavelength of 450 nm and emits strongly at 462 nm with no other significant emission peaks, whereas lab-grown coronene crystals absorb strongly at 440 nm and 462 nm, and exhibit two emissive peaks at 501 nm and 512.5 nm. Recrystallisation of karpatite resulted in crystals with both bulk and layered structures, which was reflected in the fluorescence spectra as they possessed features from both karpatite and lab-grown coronene, confirming the differences in optical properties as due to the micro-morphology of each respective crystal. Differences in relaxation pathways of excitons in bulk vs. nano-thick crystals were initially thought of as the origin of this phenomenon, but previous results on the fluorescence profiles of coronene nano-rods rendered this theory unlikely. It was then hypothesised that the answer may lie in the formation of excimers, excitons delocalised over two coronene molecules, which happens exclusively in bulk coronene crystals. This was in good agreement with both the literature and with fluorescence and UV-vis spectra. However, the exact nature of excimers within coronene is not understood and thus requires further investigation.

This is the first case in which morphology has been attributed to the alteration of optical properties in organic crystals, and the theory developed to uncover the reasons behind the differences between synthetic and naturally forming coronene crystals may therefore be applied more widely to other unexplained emissive behaviour in organic materials. Although changes to the excitonic relaxation pathways of lower-dimensional systems is unlikely to be cause of the phenomena observed in coronene, the ideas presented may help to explain why the emission spectra of microcrystals of tetracene and pyrene are unlike those of the bulk[112,111]. In order to elucidate excimer formation in layered and bulk coronene crystals, computational simulations of the electronic orbitals of dimers in the γ-coronene unit cell could be carried out. The formation of excimers in pyrene has been investigated previously, both in isolation and within the crystal structure[120]. The same methods could be applied to coronene, which could then be used to assess the favourability of excited dimer formation.

5 Chapter 5: An Experimental and Computational Study into the Crystallisation Propensity of 2nd Generation Sulflower

The work contained in this chapter has been published in part in the Royal Society of Chemistry journal ChemComm on the 14th November 2019[121].

I wrote the paper used in this chapter. I performed the electrostatic and single-point energy DFT calculations, and all experiments and analysis with assistance from Charlie Hall and Jason Potticary apart from 3D electron diffraction tomography, which was performed and analysed by Dr Iryna Andrusenko and Dr Mauro Gemmi at the Istuto Italiano di Tecnologia, Pisa. Charlie Hall performed force-field multi-molecular optimisations. Dr Hazel Sparkes collected PHENIX XRD data. CSP modelling was performed by Dr Isaac Sugden at Imperial College London. The persulfurated coronene sample was generously provided by Dr Xinliang Feng and Prof Klaus Muellen for this analysis.

5.1 Introduction

5.1.1 Planar Aromatic Molecules

Planar aromatic molecules (PAMs) are a subset of organic molecules comprised of a core of one or more aromatic rings in a coplanar arrangement. Their size can vary from a single ring (benzene) to a theoretical infinite limit of fused rings (sheets of graphene). However, at greater numbers of rings the molecule can begin to contort and cease to be planar. Theoretical studies on coronene, a disc like molecule made up of 6 peri-fused 6 membered rings, and derivatives with peripheral layers of fused rings added to create hexagonal molecules of increasing size, show that planarity is not favourable at approximately 9-12 layers[122]. The most commonly studied PAMs are polyaromatic hydrocarbons composed exclusively of fused aromatic carbon rings, such as the acene series (figure 5.1). They are often formed in the combustion of organic material, and can be extracted from deposits of oil, coal and tar[123]. However, it is possible to create aromatic cycles using heteroatoms, such as combinations of carbon with sulphur or nitrogen. For molecules comprised of only one ring (monocyclic), there must be 4n+2 electrons in π orbitals (satisfying Hückel's rule of aromaticity), necessary for completing the *s* orbital and the four available *p* bonding orbitals in the conjugated system whilst leaving anti-bonding orbitals empty[124]. These heterocyclic molecules or molecular constituents possess uneven charge distribution and therefore differing structural stability and chemical reactivity.

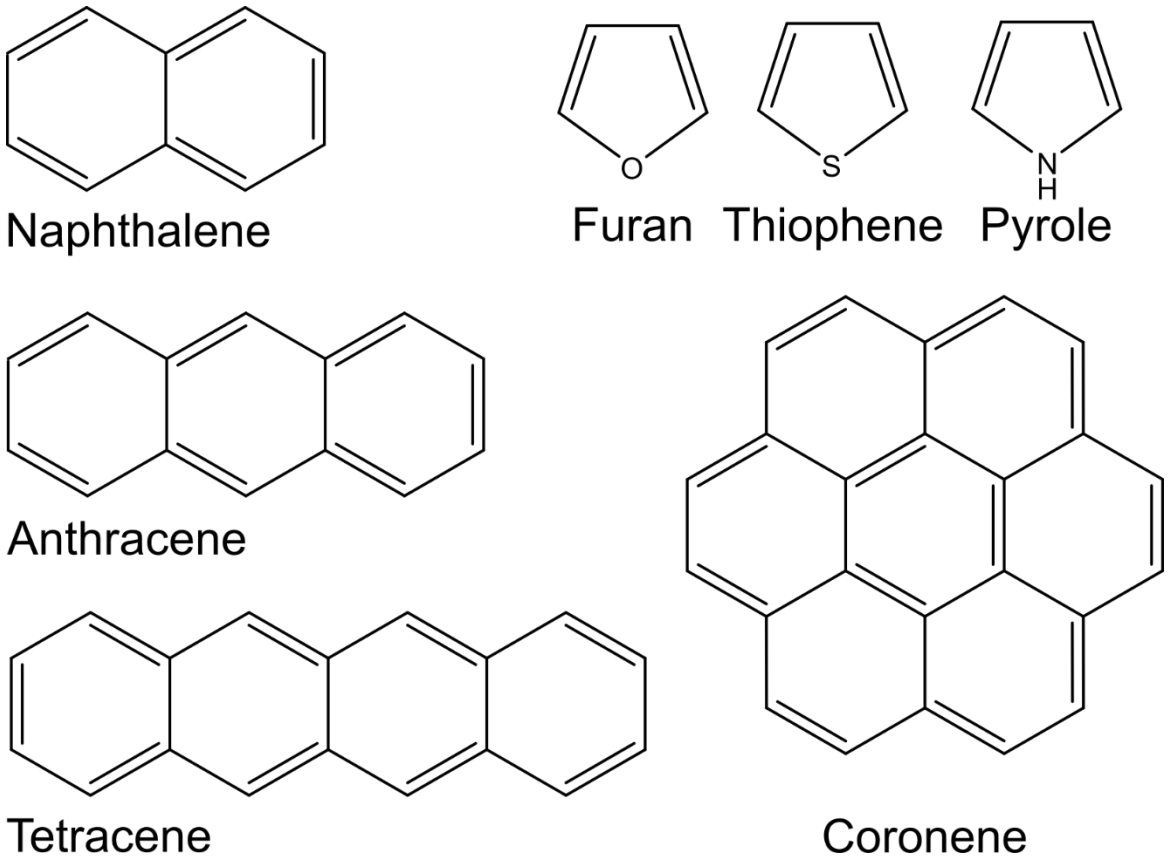

Figure 5.1: Examples of planar aromatic hydrocarbons

The delocalised electronic system of PAMs from their fully conjugated molecular structure allows for transport of charge carriers across the entire molecule and affords high molecular stability, meaning that they are promising materials for use in electronic and optoelectronic devices[125]. In solution, rigidity of PAMs restricts the quenching of excited states which can happen in non-rigid molecules[29]. In the solid state, large PAMs can be functionalised to self-assemble into co-facial arrangements due to strong intermolecular dispersion forces, leading to substantial overlap of electron wavefunctions in π bonds between neighbouring molecules and allowing for unhindered electronic transport. This property is utilised in the creation of liquid crystals, with potential uses in displays, field effect transistors and light emitting diodes[126]. PAMs are widely studied, as their relative simplicity and rigidity makes them computationally inexpensive to simulate, allowing for *a priori* calculations of intermolecular interactions and electronic behaviour without having to account for the complexity of rotating bonds which result in different molecular conformations within crystal structures[127]. They thus provide a gateway to the study of more complex organic systems both in the gaseous/ liquid and the solid state. For example, coronene has been used as a model for larger aromatic complexes such as sheets of graphene[55]. The crystal structures of planar aromatics also provide insight into the nature of interactions between aromatic groups, which aid in the understanding of bonding within biological structures such as DNA[128].

5.1.2 Aromaticity and Aromatic Molecules

The exact definition of "aromaticity" remains unclear, despite decades of experimental and theoretical research on molecules considered "aromatic". It is, broadly speaking, a property of particular conjugated cyclic organic molecules that arises due to the formation of electron clouds above and below the plane of the ring from the delocalisation of electrons in π orbitals. This affords it greater stability than would be found in a molecule of similar composition and conjugation. The simplest aromatic unit is benzene, with six carbon atoms each bonded to a single hydrogen in a hexagonal formation. Four conditions for aromaticity have been generally established:

- Alternating single and double bonds, constituting a conjugated system.
- All contributing atoms sit on the same plane
- Cyclic structure
- Contain 4n+2 electrons in π orbitals

Despite these efforts to clearly define aromaticity many exceptions exist to these rules. Molecules comprised of rings that extend over multiple monocycles, such as coronene and kekulene (so-called "superbenzene"), do not obey Hückel's rule but were thought to be "superaromatics" with electron delocalisation over the entire macrocycle. However, it has been shown recently that electrons in the latter instead group into isolated aromatic sextets[129]. Furthermore, molecules such as the spherical fullerene series which deviate exceptionally from planarity exhibit aromatic properties if they contain $2n^2+2n+1$ π electrons[130]

The electron cloud possessed by aromatic molecules is distorted if the latter are functionalised with groups that either donate charge to the conjugated system (electron donating groups) or remove electron density (electron withdrawing groups). The alteration of aromaticity via electron withdrawing groups results in increased electron affinities and ionisation energies of the molecule, with red-shifted absorption due to extension of the delocalised region[131], with the opposite true of electron donating groups[132]. By altering the electronic distribution of an aromatic molecule via functionalisation, the electrostatic potential is altered as a consequence with the creation of new permanent dipoles which alter intermolecular interactions which can lead to radically different crystal structures. The strength of dispersion forces also increases with local electron density, with electron-rich groups such as iodine resulting in the formation of stronger instantaneous dipoles.

The addition of functional groups may also change the physical profile of the molecule such that the unit cell is greatly affected, particularly for large groups, that can also sterically affect packing. This may be used to encourage greater intermolecular π-π overlap for greater charge transfer in the crystal structure. The overall effect of aromaticity in the context of intermolecular interactions is to concentrate charge into specific benzenoid or heterocyclic substituents within molecules, leading to exacerbated electrostatic dipoles, and creating extended delocalised regions that encourage dispersive interactions with other aromatic or polar molecules in the vicinity.

5.1.3 Crystallisation of Planar Aromatic Molecules

As mentioned in section 1.2.4, the crystalline state is an ideal model with which to experimentally probe the fundamental interactions that take place between molecules as their continuous order provides a direct link between the macro- and micro-scale. An understanding of such interactions has made the prospect of predicting the crystal structures of molecules feasible, which is of high importance to the pharmaceutical industry as it would allow for the prediction of physical properties of crystals before the base molecules have even been synthesised, or in identifying forms of known drugs with higher dissolution rates so that routes can be found toward their crystallisation[133].

In 1989, in an effort towards predicting the crystal structures of aromatic molecules, Desiraju and Gavezzotti measured the unit cell parameters of 32 planar aromatic molecules, chosen for their well-defined crystal packing motifs and rigidity which eschewed the complication of undefined molecular profiles from non-rigid molecules. They realised that the structures could be classified into distinct categories when grouped according to the shortest axis of their unit cell and the angle between the planes of neighbouring molecules[100]. Whilst the classification of crystal structures via these parameters may appear arbitrary, it may be justified when considering the intermolecular forces which bind neighbouring molecules in the structures. The magnitude of each parameter is dependent on the relative contribution of two intermolecular bonding mechanisms. The first is electrostatic interactions: the electron density in the π system results in a partial negative charge above and below the plane of the ring, with positive charge at the periphery (Table 5.1). The resulting permanent dipole causes attraction between the edges and faces of neighbouring molecules, which encourages perpendicular molecular arrangements and therefore greater interplanar angles, with shorter unit cell axis lengths. The second is dispersion interactions, caused by the overlap of wavefunctions in the rings of neighbouring molecules. This results in the creation of instantaneous dipoles which act against electrostatic repulsion to attract electron-rich molecular substituents together. Stacking is then encouraged between the faces of aromatic ring structures and leads to unit cells with lesser interplanar angles and short axis lengths where these forces are dominant. The combination of these two forces results in structures with slipped stacks of two or more molecules and oblique edge-face interactions (Figure 5.2). in the gamma (γ) and beta (β) herringbone structures, the slipped stacks permeate through the entire crystal lattice, with the stacks linked through edge-face interactions between the exposed substituents of the molecules. In the Herringbone (HB) structure, the nearest neighbouring molecules are non-parallel. The sandwich herringbone (SHB) structure is similar, but with sandwich-like diads in place of single molecules.

Whilst this work exclusively covered polyaromatic hydrocarbons, Desiraju and Gavezzotti later speculated that the effect on crystal structure should be the same whenever similar molecular shapes are found in organic compounds which are not exclusively composed of carbon and hydrogen[134]. The nearest neighbour angle and

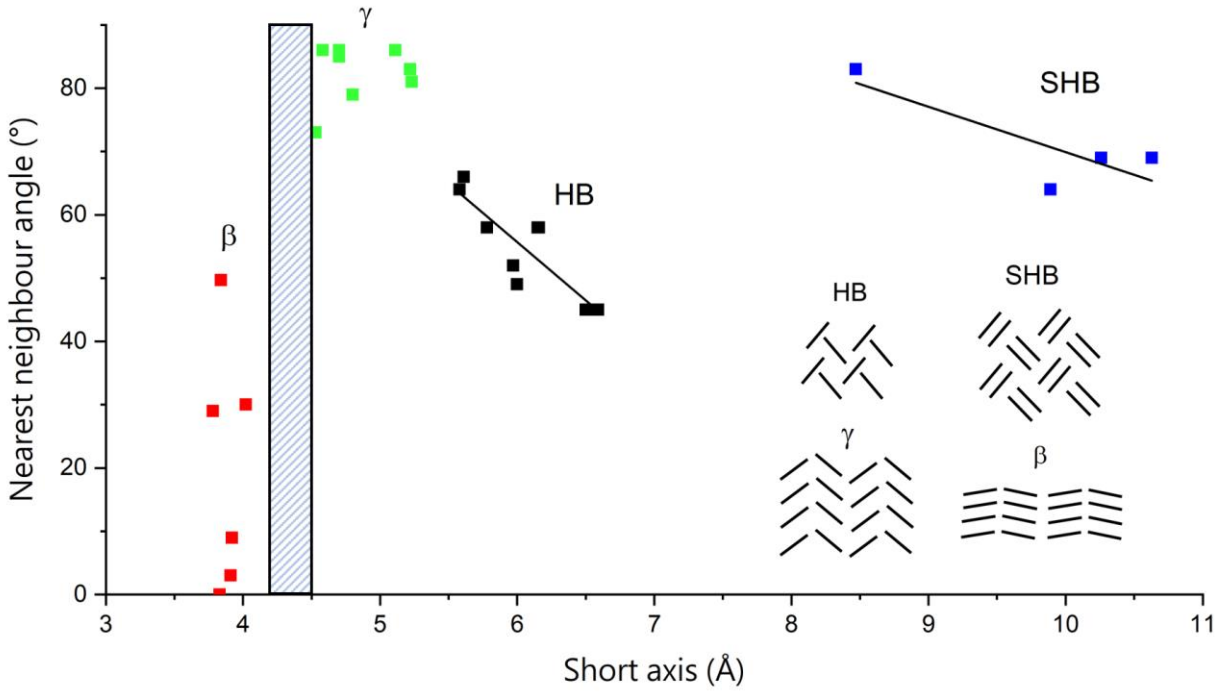

Figure 5.2: The four types of molecular packing in crystals of planar aromatics and their short axis lengths and interplanar angles. a) Herringbone b) sandwich herringbone c) gamma d) beta. Adapted from Fig. 3 in ref[100].

short axis length of crystal structures of a number of heterocyclic planar molecules were tested (Table 5.1), with all falling within one of the four motif categories, demonstrating that this statement likely holds true. Although the work suggests that it may be possible to predict which structure a PAM will adopt purely based on its molecular structure, it does not take into account polymorphism and the possibility that multiple conformations may arise from a single molecule. For example, coronene has both a gamma herringbone polymorph (Figure 5.3) and a recently discovered beta herringbone form when grown under an applied magnetic field[98]. Therefore, while the existence of discrete structure groups of this class of molecule appears likely, the molecular structure alone is not enough to accurately predict which category a molecule will form on crystallisation, and the form taken depends on numerous experimental conditions during growth. In 1994, Gavezzotti famously opened an article entitled "Are Crystal Structures Predictable?" with a single word sentence: "No."[135] However, as understanding of nucleation and intermolecular interactions has developed and molecular simulations have become more powerful and accurate, crystal structure prediction (CSP) may now be used complementarily to empirical crystal screening methods to identify potential stable crystal structures that may be formed under untested conditions[136].

Whilst crystallisation is a common trait amongst small organic molecules, there are many cases where molecules are seemingly unable to form an ordered crystalline state under experimental conditions, and instead form disordered glass phases. A recent machine-learning study identified two important factors of a molecule's propensity to crystallise: the number of rotatable bonds, and the zero-order molecular valence connectivity

Name	Formula	Interplanar Angle (°)	Short Axis (Å)	Crystal Structure type	Ref	Max. charge density (e/Å^3)	Electrostatic Potential
Benzene	C_6H_6	88	6.92	HB	[137]	0.025	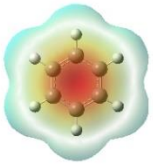
Naphthalene	$C_{10}H_8$	52	5.97	HB	[137]	0.022	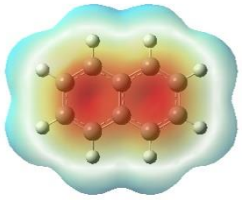
Anthracene	$C_{14}H_{10}$	49	6.00	HB	[137]	0.021	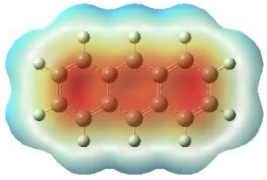
Phenanthrene	$C_{14}H_{10}$	58	6.16	HB	[137]	0.022	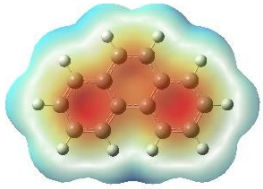
Carbazole	$C_{12}H_9N$	55.59	5.66	HB	[138]	0.055	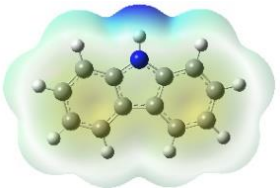
dibenzo[b,d]thiophene	$C_{12}H_8S$	55.42	5.96	HB	[139]	0.021	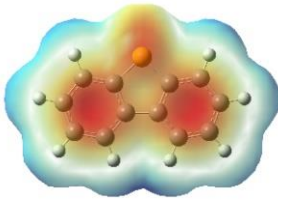
Indigo	$C_{16}H_{10}N_2O_2$	71.37	5.77	γ	[140]	0.047	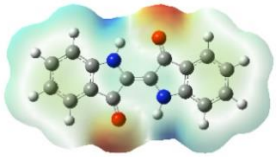
Pentathienoacene	$C_{12}H_4S_5$	50.27	3.89	β	[141]	0.020	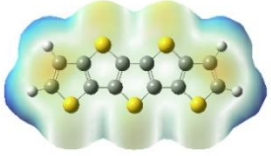

Coronene	$C_{24}H_{12}$	85	4.70	γ	[137]	0.024	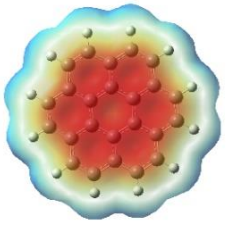
Perfluorinated coronene	$C_{24}F_{12}$	--	--	[unknown]	--	0.032	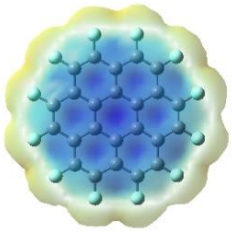
Hexabenzocoronene	$C_{42}H_{18}$	86	5.11	γ	[137]	0.021	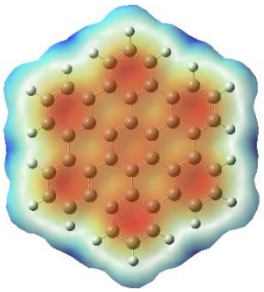
Cyclosexithiophene	$C_{16}H_4S_6$	71.80	10.42	SHB	[142]	0.025	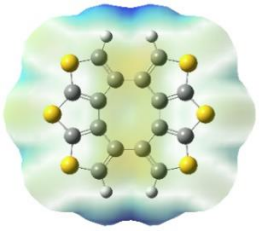
Sulflower	$C_{16}S_8$	47.51	3.89	β	[143]	0.040	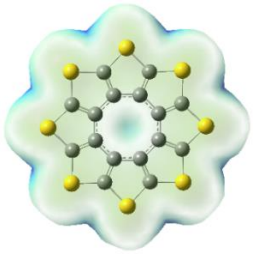
Persulfurated coronene	$C_{24}S_{12}$	--	--	--	--	0.028	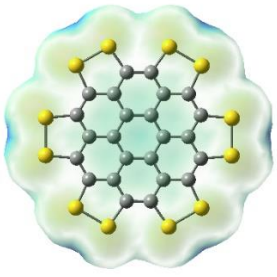

Table 5.1: Crystal structure motifs of the most widely studied polymorph of a range of different PAMs, and their electrostatic potential surfaces. Red (blue) indicates negative (positive) charge density. Grey atoms = carbon, white = hydrogen, blue = nitrogen, red = oxygen, yellow = sulphur.

index, which is correlated with the molecular weight. A greater magnitude for both these parameters was found to be associated with a reduced likelihood of crystal formation[144]. PAMs by definition must contain no rotatable bonds, and their combination of rigid structure and free-moving charge over large delocalised π-systems means that they are pre-disposed toward crystallisation. Indeed, even chlorinated PAMs with close to 100 carbon atoms (so-called "nano-graphenes") have been crystallised[145]. Thus far, there are no known cases where a PAM has been proven to be unable to crystallise.

This chapter covers how a recently synthesised PAM, persulfurated coronene, cannot feasibly crystallise under normal experimental conditions, owing to the electrostatic charge distribution across the molecule, breaking with conventions of crystallisation that have held true for all like molecules.

5.1.4 Coronene and Functionalised Derivatives

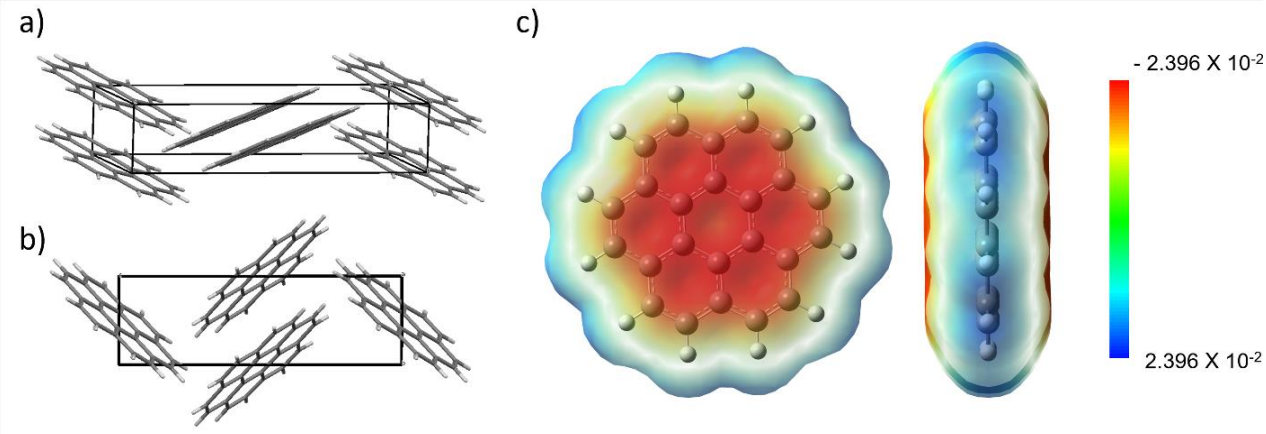

Figure 5.3: a) beta and b) gamma polymorphs of coronene, viewed slightly offset from the a and c axes and down the *a*-axis respectively. c) Electrostatic potential map of a coronene molecule. Units in eV.

As mentioned in section 4.1, coronene ($C_{24}H_{12}$) is a planar aromatic hydrocarbon comprised of six aromatic rings in a hexagonal arrangement, with hydrogen atoms around the edge of the disc. The molecule has a delocalised π-system of 24 electrons, allowing for dispersion interactions between neighbouring molecules. A simulation of the electrostatic potential (ESP) of a coronene molecule reveals a concentration of charge around the rings, with the peripheral hydrogen atoms highly electropositive (figure 5.3), enabling electrostatic edge-face interactions. The difference in charge density between the centre and edge is up to 0.042 e/ Å^3. As There are two known crystal structures of coronene: a gamma form, with a nearest neighbour angle of 95.86 ° and a short axis length of 4.67 Å, and a recently discovered beta form, with a nearest neighbour angle of 49.71 ° and a short axis length of 3.84 Å[98]. In the gamma form, the electrostatic interactions between the positively charged hydrogens and negative aromatic core are the dominant bonding mechanism, with minimal π-π overlap down the π-stacks along the unit cell *b*-axis. In the beta form, dispersion forces are the dominant mechanism, leading

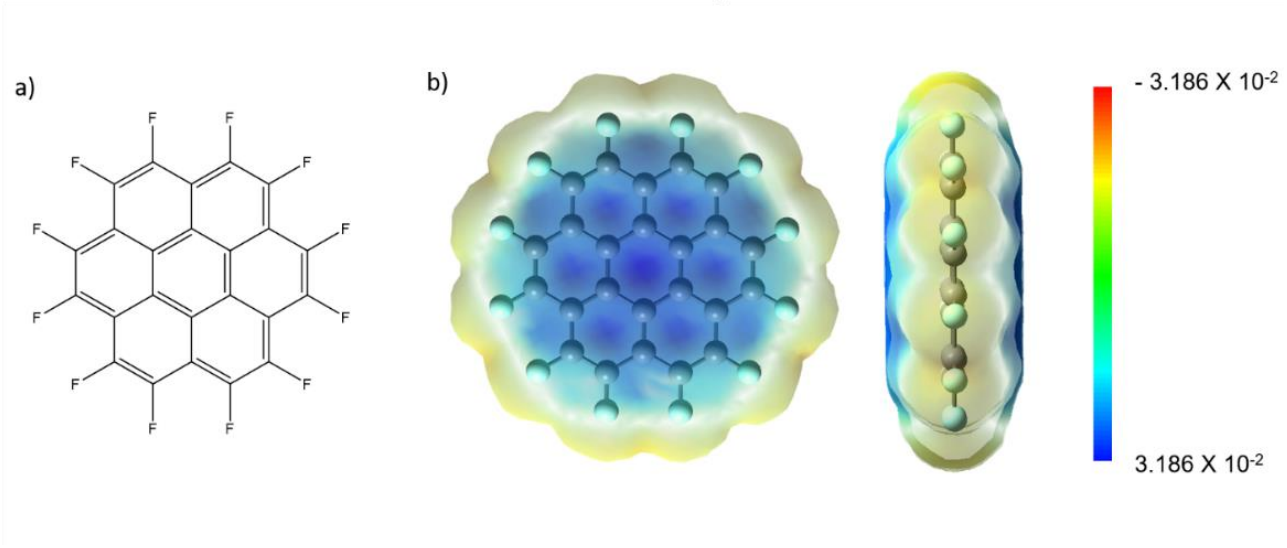

Figure 5.4: a) Molecular structure and b) ESP surface of perfluorinated coronene. Units in eV.

to tight molecular packing down the *b*-axis near-perpendicular to the plane of the molecules, with C-H binding between stacks of lesser strength compared to the gamma form. After performing DFT-D optimisation of two coronene molecules at 0 K, the molecules stack in a near-cofacial arrangement, with an offset of 1.61 Å[146] .This closely matches with the stacking observed in the beta form, found via low-temperature pXRD to be the most stable form below 100 K [101].

Coronene has been widely functionalised in order to alter its electronic properties[147]. One such way this could be done is by substituting the hydrogen atoms with highly electronegative fluorine to create perfluorinated coronene (PFC). Although this molecule has not yet been synthesised, structure optimisation calculations on the molecule reveals that it would be planar like coronene[148]. However, the ESP surface is reversed, with charge pulled toward the fluorine atoms leaving the aromatic core electropositive (figure 5.4). The polarisation between the centre and edge is also enhanced, with a difference in charge density of up to 0.049 e/ Å^3.

5.1.5 Persulfurated Coronene

Persulfurated coronene (PSC, $C_{24}S_{12}$) is a recently synthesised variant of coronene in which the hydrogen atoms have been substituted for sulphurs. It has been considered the next generation of "sulflower" ($C_{16}S_8$), a similarly rotationally symmetrical planar molecule with a delocalised π-system at its core and periphery of sulphur atoms, hence its alternative name "2nd generation sulflower". It has potential use as a cathode material in lithium-sulphur batteries owing to its high capacity and stability after multiple cycles. It is planar like coronene, but its calculated ESP surface shows a broadly homogeneous distribution of charge, with a charge density near 0 e/Å^3 around the aromatic core and at the edge of the molecule, apart from positive regions of up to 2.809 e/Å^3 above each of the S-S bonds (figure 5.5). This appears to be unique case for PAMs, with many others displaying far greater

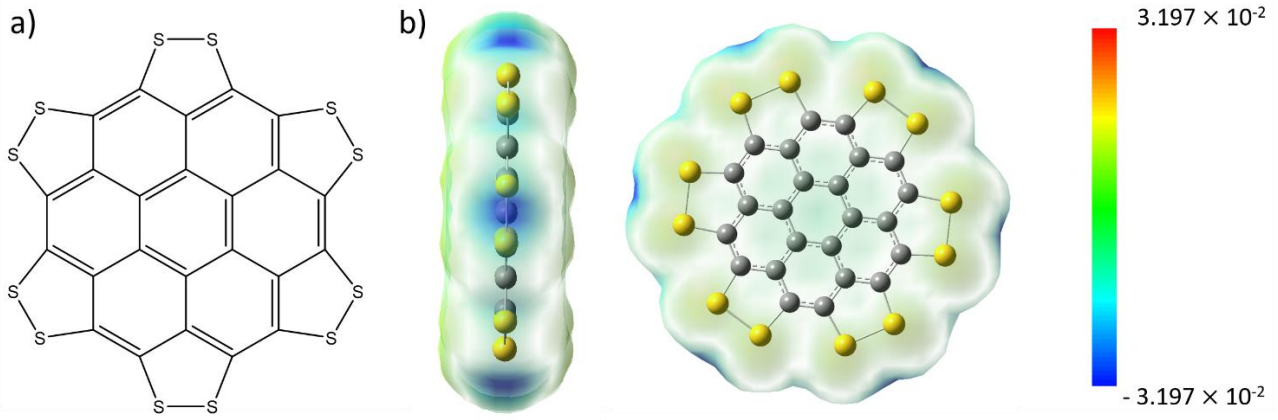

Figure 5.5: a) Molecular structure and b) ESP surface of persulfurated coronene. Units in eV.

polarisation between their centre and edge (Table 5.1). Previous attempts at crystallisation were unsuccessful, attributed to its low solubility in the solvents tested[59]. The following experimental and computational work covers the attempted crystallisation of this molecule and explores the reasons as to why such a molecule is not able to form into an ordered crystalline state as a result of its unique electronic distribution.

5.2 Experimental Results

5.2.1 Crystallisation attempts

it was initially thought that PSC would almost certainly adopt a crystalline form. This is due to its symmetry and rigidity, and its similarity in structural form and dimensions to hexabenzocoronene which crystallises into the gamma herringbone structure (Table 5.1). Any resulting crystal was thought to possess interesting electronic properties due to the visible-range light absorption and enhanced conductivity afforded in the solid state by sulphur functionalisation[149]. Numerous attempts at crystallisation via established methods were therefore attempted.

Of the solvents tested for solvent crystallisation (section 2.2.1.2) PSC was only found to be soluble in N-Methyl-2-Pyrrolidone (NMP) to greater than 2 mg per ml, making it the only potential solvent with which to attempt crystal growth. However, under cooling of a saturated solution at 60 °C to -10 °C, all material remained in solution. Evaporation was not feasible due to the high boiling point of NMP, resulting in a dense brown liquid after one month with no solid aggregation. Dropcasting onto a cooled microscope slide resulted in aggregates up to approximately 2 mm^3 in size forming (figure 5.6).

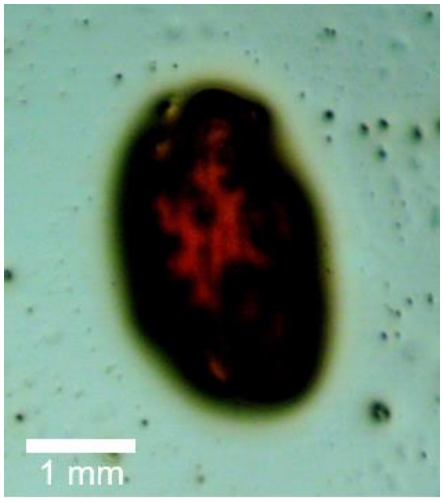

Figure 5.6: An aggregate formed from the dropcasting of saturated PSC solution in NMP

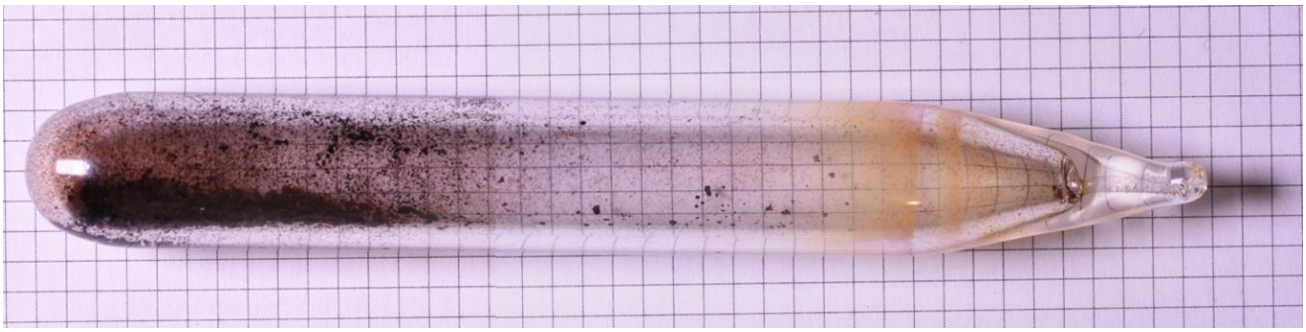

Figure 5.7: A sealed glass ampoule used in the attempt of PSC growth (composite image). Squares are 5 mm^2.

PVT in an open-air system with a continuous flow of nitrogen gas resulted in a black residue at the point of sublimation, and a brown lining on the glass 10 cm from the sublimation point, which was unable to be extracted for XRD analysis. This was repeated in a vacuum sealed ampoule, similarly producing a black residue indicating decomposition of the PSC, with deposition of sublimated material forming a brown lining on the opposite end of the ampoule (figure 5.7). The ampoule was observed under a microscope with light polarised at 90° to the microscope lens in order to see whether the lining exhibited birefringence characteristic of organic crystals. No birefringence was observed, confirming the amorphous nature of the deposited material.

Powder XRD was utilised to establish the crystallinity of the as-provided PSC powder (figure 5.8). These data were collected with a chromium-plated copper sample holder over 5-50° 2θ. The pattern exhibits features attributable to the sample holder, as well as two wide peaks at 8.31° and 25.55°. In order to examine whether these peaks would change in intensity at lower temperature, XRD scans were taken at 12 K and again at 300 K after warming (figure 5.9). All scans produced similar patterns to within experimental error. XRD data was collected on the aggregates produced from dropcasting on a silicon sample holder at 300 K over 5-50° 2θ, a range sufficient to identify any planes of reflection present in an organic crystal unit cell. The pattern shows no differences to a scan performed on the same sample holder with no material present, meaning the aggregates are completely amorphous.

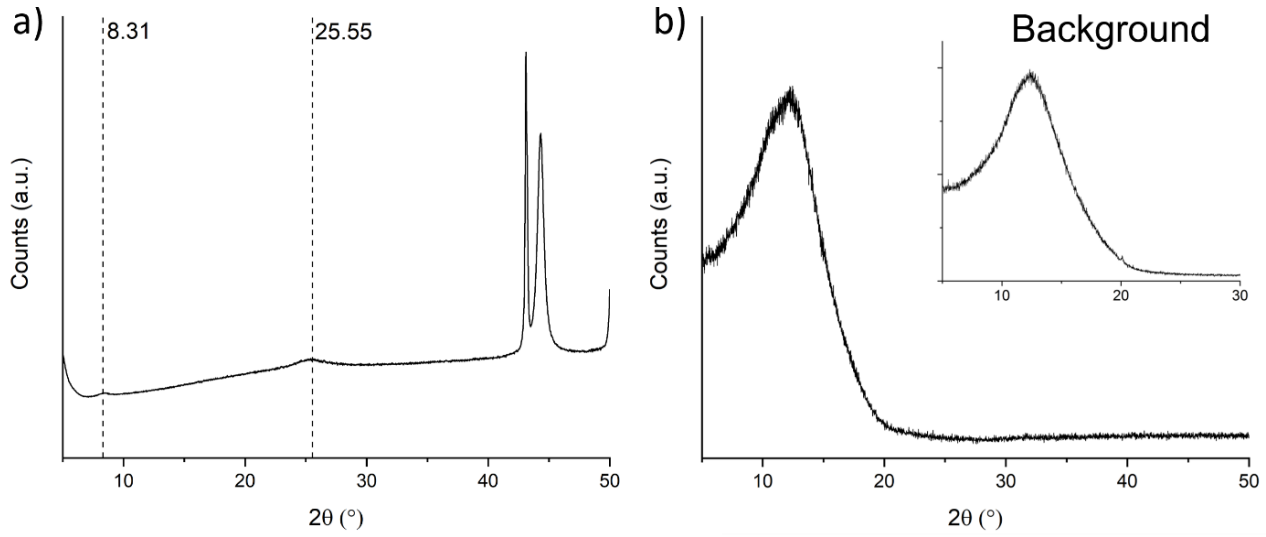

Figure 5.8: a) Powder XRD data from raw persulfurated coronene powder. Peaks at <7°, 43.20°, 44.30° and >49° due to sample holder. b) Powder XRD data from dropcast persulfurated coronene aggregates. Inset: Pattern of sample holder with no sample.

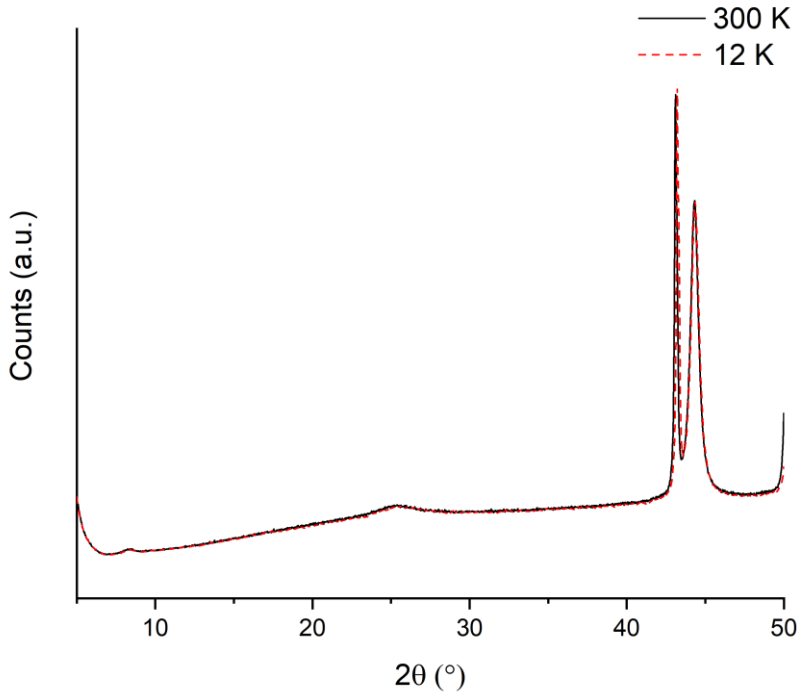

Figure 5.9: pXRD scans of as-received PSC powder at 300K and 12K. Peaks at <7°, 43.20°, 44.30° and >49° due to sample holder.

5.2.2 3D Electron Diffraction Tomography

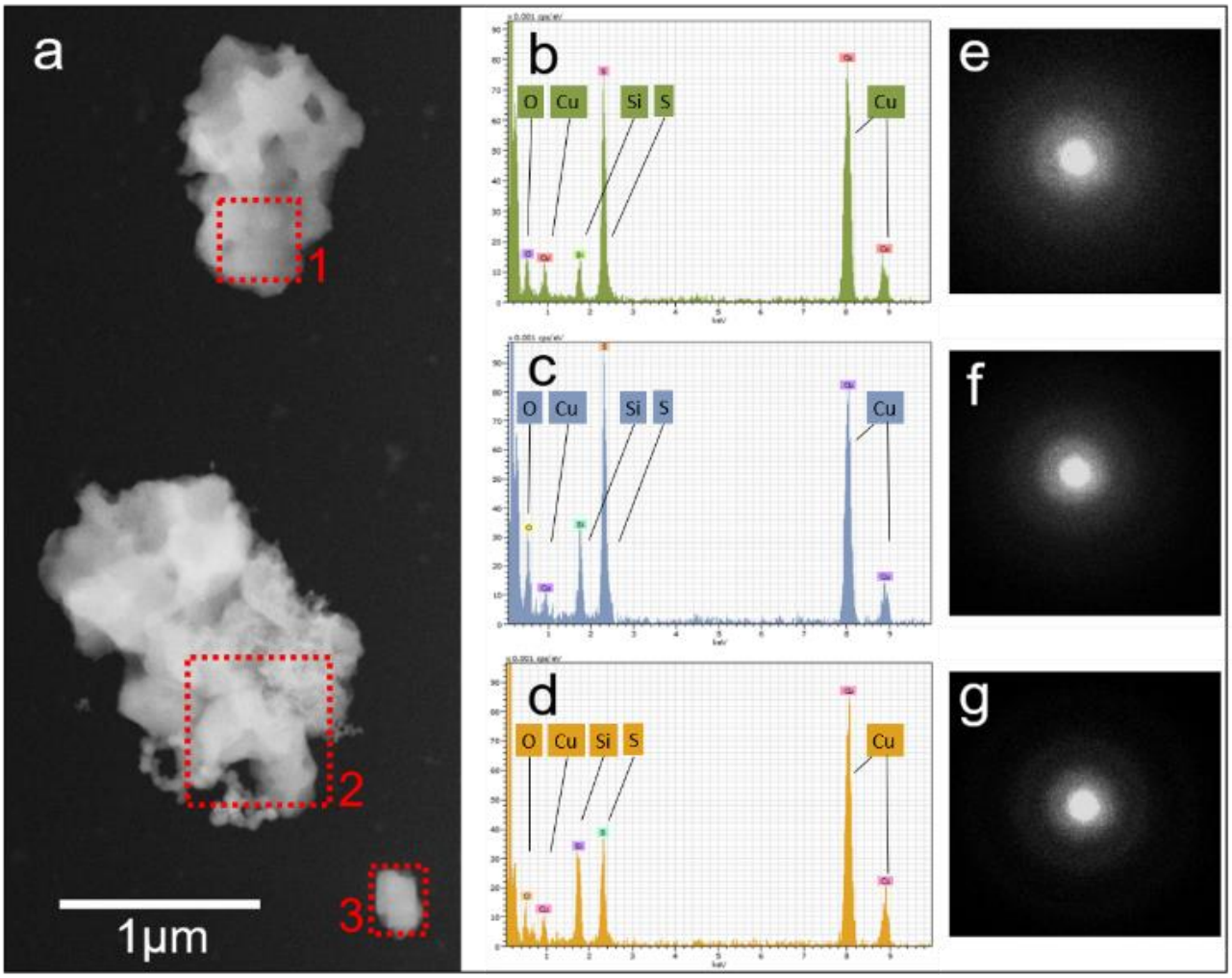

Figure 5.10: (a) STEM overview. (b, c, d) EDS spectra from areas 1, 2, 3 in (a). Cu, Si, O signals come from grid and detector. (e, f, g) ED patterns from areas 1, 2, 3 in (a).

3D ED-TEM has been used to obtain full structure solutions to the unit cells of micro-sized crystals several orders of magnitude smaller than could be solved via SC-XRD, and can be carried out using low-dose electron beams to ensure that any destruction of sample is minimal[150]. It was therefore applied to powder of PSC in order to investigate whether any crystalline material was present at all. Energy dispersive X-ray spectroscopy (EDS) spectra were collected from selected areas on three different aggregates between approximately 0.25 and 2 μm^3 in size (figure 5.10 b-d). In all cases, EDS spectroscopy revealed the presence of sulphur (S), confirming that these aggregates were of PSC. The S:C ratio could not be measured as the carbon (C) signal could not be quantified. ED data collected via TEM from these areas did not exhibit any diffraction spots which would be expected from crystalline material. Instead, the sample gave diffuse rings which show complete uniformity in electron scattering angle, consistent with an entirely amorphous state of matter (figure 5.10 e-g).

5.2.3 Differential Scanning Calorimetry

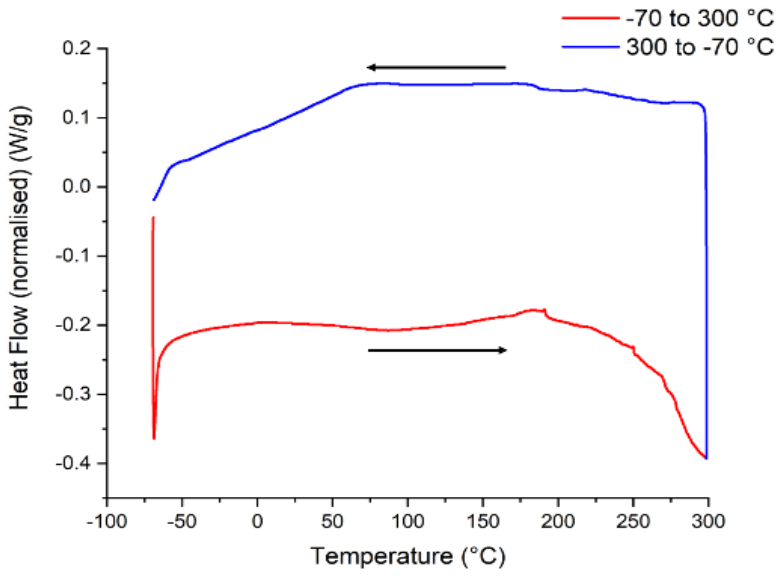

Figure 5.11: DSC data on as-supplied PSC powder. Arrows indicate direction of heating/ cooling.

In order to identify whether the PSC powder exhibited any crystalline phases at temperatures beyond the range tested via solvent growth, DSC was carried out on the powder (figure 5.11). A hermetically sealed pan containing 2.8 mg of PSC was subjected to a heating and cooling cycle between -70 °C and 300 °C, and from 300 °C to -70 °C at a rate of 10 °C/min. The measured relative heat flow in or out of the material as a function of temperature clearly shows no crystallisation events over the run, which would be indicated by a sharp uptake in heat flow at the onset and typically have enthalpies to the order of 100 J/g[151]. The only features present are a broad endothermic valley between 200 °C and 300 °C as a result of partial sublimation of the material and a linear endothermic transition during cooling which is likely due to the amorphous solidification of PSC aggregates.

5.3 Computational Results

The combination of various growth methods, ED-TEM and DSC strongly suggest that, in spite of its planarity and structural similarity to hydrocarbon molecules which can be crystallised with relative ease, PSC does not possess a readily accessible crystalline state. As the shape of the molecule is not detrimental toward crystal growth, the reason must lie within its electronic structure. The isotropy of charge across PSC arises from the electron-withdrawing effect of the peripheral sulphur atoms. Comparisons with the ESPs of coronene and PFC (Figure 5.12) show that there is far greater variation in charge between the molecular centre and edge. In the case of PFC, the electron density that concentrates around the aromatic core of a non-functionalised PAM is

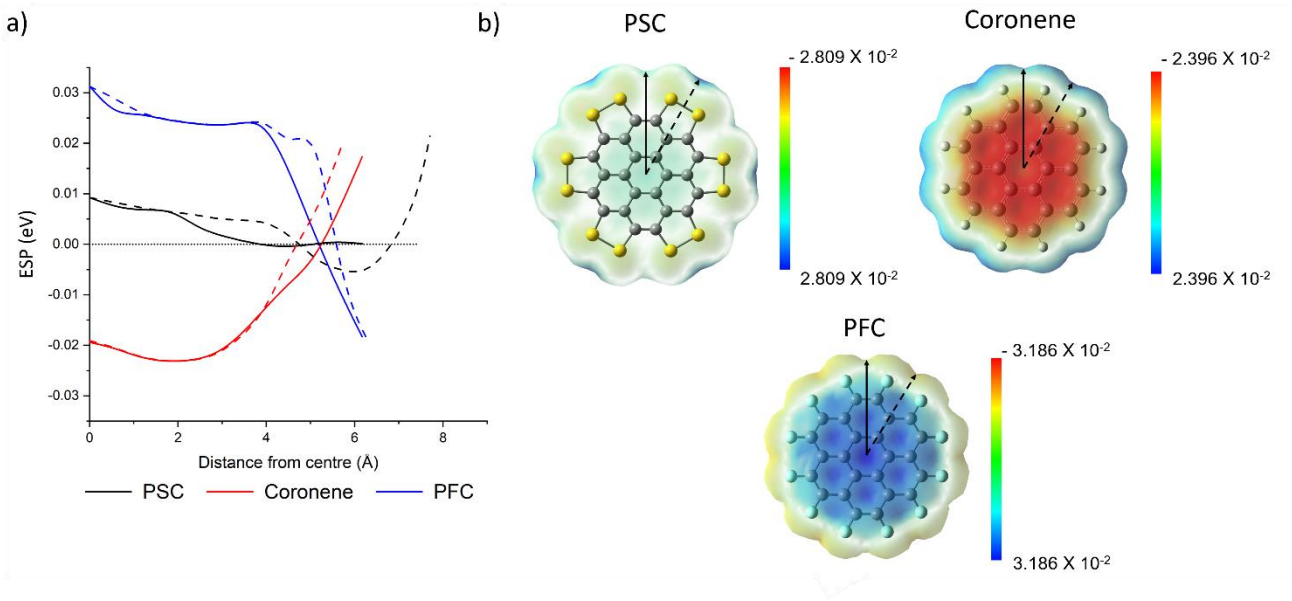

Figure 5.12: Calculated electrostatic potential across perfluorinated coronene, coronene and persulfurated coronene in a line from the centre of the molecule to the edge down the centre of the anthracene constituent (solid) and along the radial carbon-carbon bond (dashed). b) Full electrostatic potential map of i) persulfurated coronene, ii) coronene and iii) perfluorinated coronene. Units in eV.

pulled toward the edge due to the electronegativity of the fluorine atoms, resulting in a reversal of charge distribution when compared to the base molecule. The effect is the same in PSC, however the electronegative pull of the sulphur atoms appears to balance with that of the core such that there is little charge variation across the entire molecule. Although there are positive regions above each S-S bond, these cannot interact attractively with the weakly positive core of neighbouring molecules to form the kind of edge-face interactions seen in the crystal structures of coronene (figure 5.3).

The ESP of sulflower (figure 5.13) is similar in many ways to that of PSC: it is broadly isotropic, with little variation in charge density between the centre and edge with the exception of positive regions near which appear due to charge being pulled toward the sulphur atoms. However, a crystal structure of sulflower has been obtained via a combination of experimental data and theoretical fitting[143]. The molecular geometry is such that sulphur atoms in adjacent thiophenes contribute to the positive regions in the ESP, giving them a greater magnitude in positive charge density compared to PSC and therefore encouraging interactions with positively charged sulphur atoms in adjacent molecules. This bonding motif is weak compared to the dominant C-C interactions down the stacks, resulting in a short axis of 3.89 Å and a nearest neighbour angle of 47.51°, placing it within the β family of crystal structures (Table 5.1). The sulphurs in PSC are not positioned in a similar manner, leading to less positively charged external regions that cover a greater area on the potential surface. Thus, both the elemental composition and molecular geometry of PSC, and the resulting electronic distribution, appear to make it unable to readily form into an ordered crystalline state. This is further explored in the following theoretical study into the interaction between PSC molecules.

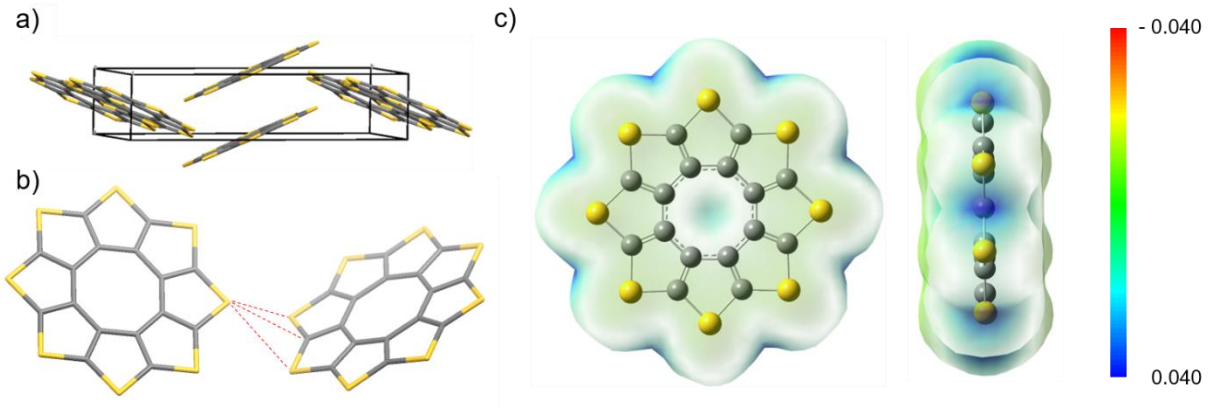

Figure 5.13: a) Crystal structure of sulflower viewed slightly offset from the b and c axes. b) interaction between sulflower molecules in neighbouring π-stacks. c) ESP map of a sulflower molecule. Units in eV.

Electrostatic attraction between molecules due to the anisotropy of their ESPs is the dominant driving force for crystallisation in PAMs[152]. However, the homogeneity of the ESP surface of PSC means that it is non-trivial to imagine how two molecules would likely interact. To this end, a series of 100 two-molecule rigid body optimisations were performed via force-field-based calculations in the ORIENT software package [153] (figure 5.14). Two molecules were placed in randomised differing positions with respect to each other, and their positional energy minimum calculated. This resulted in two optimised configurations corresponding to energy minima in the interaction potential between the dimers: an offset stacking mode in which the molecules are aligned, and a direct stacking mode with the molecules twisted by a specific torsion angle (known as the "twisted sandwich" mode[154]). When repeated with dimers of coronene and sulflower, the same motifs are present. Table 5.2 summarises the stacking motifs and their associated potentials, with a more negative potential indicating greater thermodynamic stability. The twisted stacking mode is more stable than the offset stack for PSC and sulflower, with the greatest difference in energy between PSC modes (4.3 kJ mol^{-1} for sulflower and 7.7 kJ mol^{-1} for PSC). For coronene, the offset stack is more stable by 0.6 kJ mol^{-1}, suggesting that thermal effects would be sufficient for the dimers to transition between the two forms, given that *RT* (the product of the gas constant and the temperature) at 298 K is 2.479 kJ mol^{-1}. PSC is the only case in which the electrostatic interaction contributes constructively to the stability of the conformations, owing to the overlap of oppositely charged regions in the electrostatic potential in the PSC dimers. The broad peaks in the XRD pattern of the raw PSC powder (Figure 5.8) at 25.55° and 8.31° correspond to d-spacings of 3.48 Å and 10.63 Å respectively, which match closely with the optimised distance between two and four stacked PSC molecules. This would suggest that π-stacks of at least four molecules are present throughout the material. The presence of direct stacks rather than offset stacks is more likely due to their enhanced stability. Low temperature XRD data was collected to determine whether reduced thermal fluctuation would encourage greater stack formation and therefore lead to increased peak intensity. However, the peaks remained the same height at 12 K and at 300 K after reheating (figure 5.9).

100 three-molecule optimisations were examined for PSC and coronene, resulting in several different modes with various combinations of face-face and edge-face interactions (figure 5.15). The direct stacking mode in

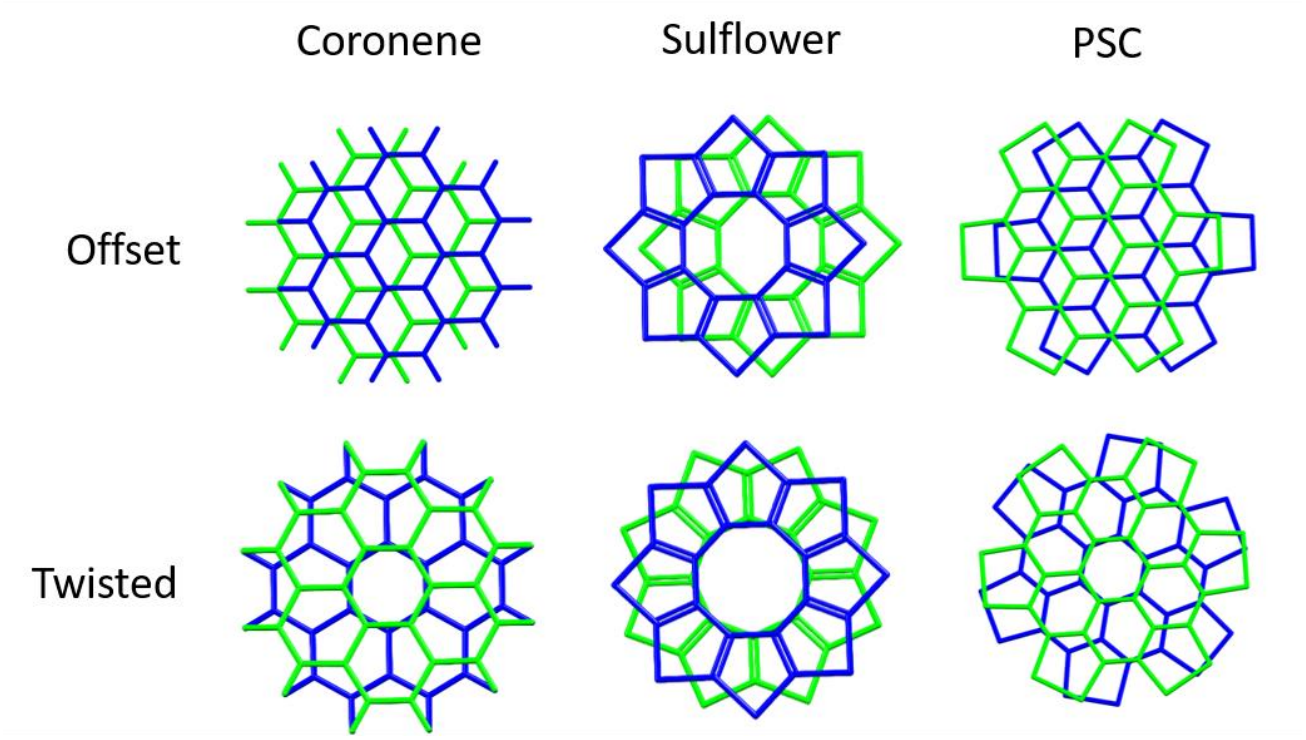

Figure 5.14: Simulated dimer conformations of coronene, sulflower and PSC from ORIENT, with both offset (top row) and twisted (bottom row) stacking modes.

Dimer	Mode	Distance (Å)	Offset (Å)	Torsion (°)	Energy (kJ.mol^{-1})			
					E.S.	Rep.	Disp.	Total
Coronene	Offset	3.499	1.376	0	8.8	60.7	-162.2	-92.8
	Twisted	3.538	0	30	12.8	69.2	-164.2	-92.2
Sulflower	Offset	3.538	1.231	0	2.5	61.5	-158.3	-94.3
	Twisted	3.569	0	22.5	2.2	65.8	-166.6	-98.6
PSC	Offset	3.535	1.293	0	-2.1	105.2	-267.4	-164.3
	Twisted	3.538	0	16.25	-5.7	108.8	-257.4	-172.0

Table 5.2: Parameters of the two dimer conformations of coronene, sulflower and PSC with their associated potentials and the electrostatic, repulsion and dispersion contributions.

PSC is the most favourable for all numbers of molecules tested, with conformations featuring edge-face interaction approximately 0.65 times as stable and with a difference of 125 kJ mol^{-1}. The coronene trimers all formed into two configurations: all three offset-stacked, and two offset-stacked with the face of the third molecule interacting with the edge similar to the gamma polymorph. Over 100 calculations of each number of molecules, no direct stacking between coronene molecules was observed, suggesting that this mode is at least unlikely to manifest in pre-nucleation clusters.

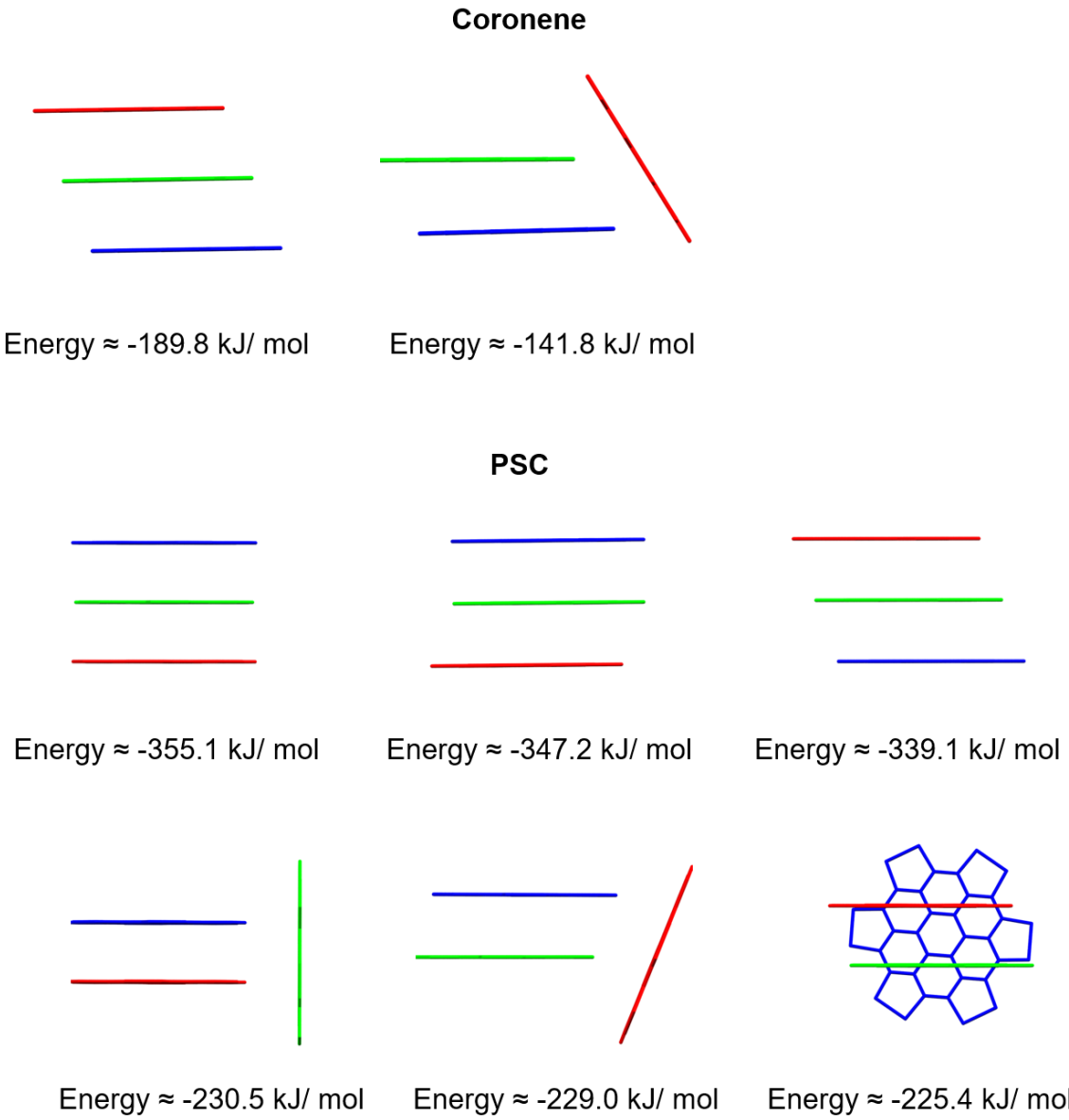

Figure 5.15: Three-molecule stacking modes adopted by coronene and PSC and their associated potentials. Coronene adopted two distinct conformations over 100 simulations, compared to PSC's six.

The interaction potential landscapes of dimers of PSC, coronene and sulflower in the x-y plane were calculated at constant optimised z-axis separation, for molecules in a cofacial and perpendicular arrangement (figure 5.16). The coordinates of the minima in the potential landscapes of the face-face dimers correspond to the positional offsets in the offset stacks. The interaction potential landscapes of two molecules arranged cofacially and rotated at constant z-separation were calculated between rotationally symmetric isomers. Similarly, the angles of the interaction potential minima match with the torsion angles of the direct molecular stacks. The differences in the interaction potential calculated from the Gaussian energy landscapes and ORIENT two-molecule optimisations are due to the method of calculation, with ORIENT simulations assuming a static potential field around each molecule and Gaussian iteratively adjusting the potentials based on the relative positions of each molecule (section 1.5). The positions of the minima in both the offset and twisted stack dimers match closely. The results

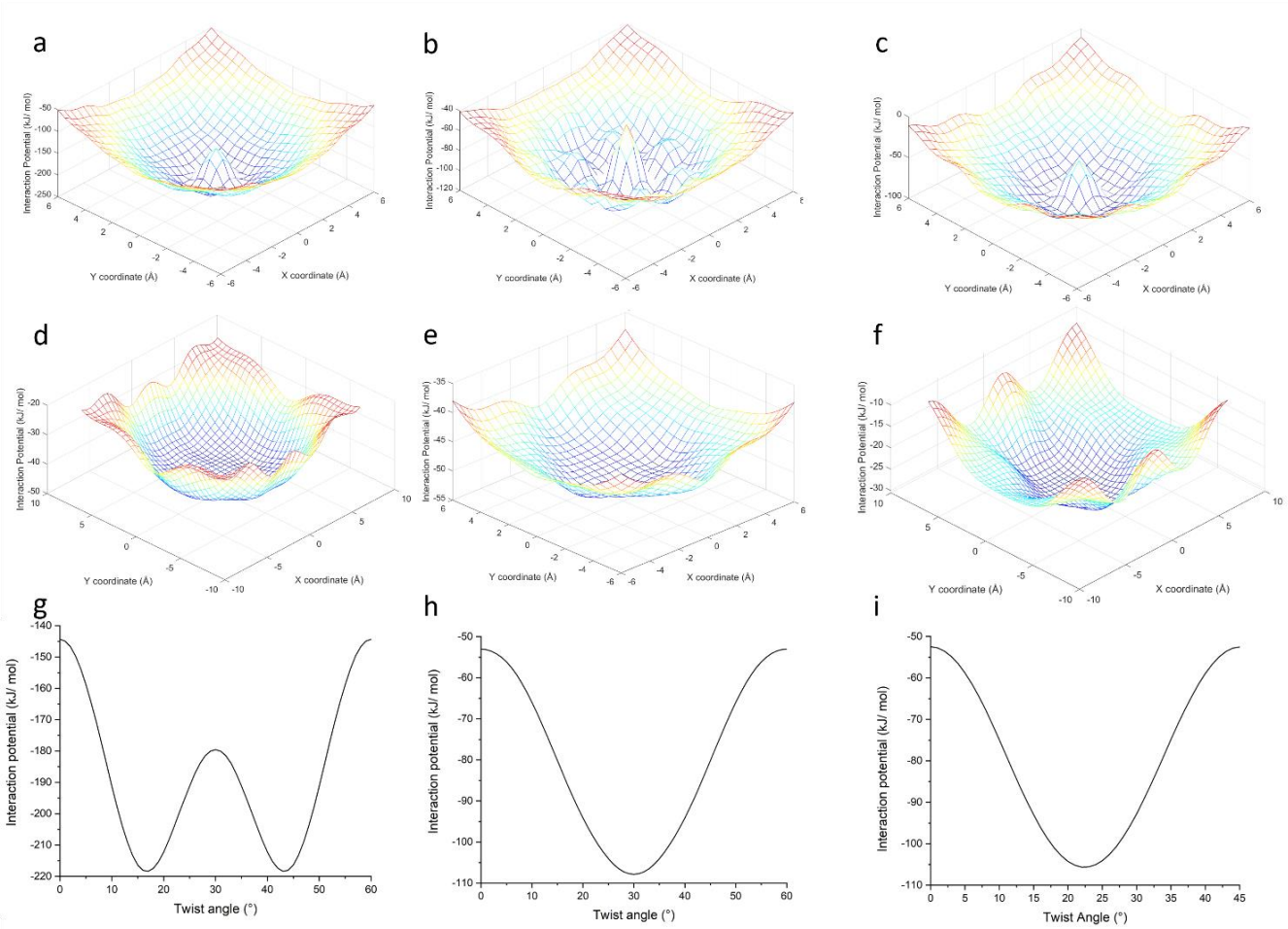

Figure 5.16: Dimer interaction potential landscapes of PSC, coronene and sulflower. a, b, c: Two molecules arranged in an aligned face-face configuration with one moved over a grid in the x-y plane at constant optimal z-value separation. d, e, f: Two molecules perpendicular to each other with one moved over a grid in the x-y plane at constant optimal z-value separation. g, h, i: Two molecules arranged in an aligned face-face configuration with one twisted about the centre in the x-y plane at constant optimal z-value separation. Calculations performed with a b97d functional and 6-31g basis set in the Gaussian software package.

show that face-face stacked PSC dimers are approximately five times as stable as T-shaped dimers, with the latter possessing a far broader potential well such that no one configuration is preferred within a lateral radius of approximately 3.5 Å from the centre. The interaction potential for the face-face dimer of coronene is approximately twice as strong as that of its T-shaped dimer, suggesting that molecules would be more likely to adopt this conformation pre-nucleation which would be conducive toward crystal structure formation. For PSC however, it is likely that clusters of direct-stacked molecules would form which would be unable to then transition to a configuration that would then allow for crystal growth.

CSP modelling was used to test whether any stable crystal structures of PSC could exist. The computational methodology was first tested for its applicability in predicting the crystal structures of large, sulphur-decorated organic cyclic molecules by investigating sulflower. The known experimental form was identified as the fifth lowest energy structure, <1.0 kJ/mol from the global minimum. The Root mean squared deviation of a cluster of 15 molecules (RMSD15) from the known experimental structure is 0.56 Å. The polymorphic landscape, indicating all possible polymorphs which may exist according to the simulation, is given in figure 5.17. Given

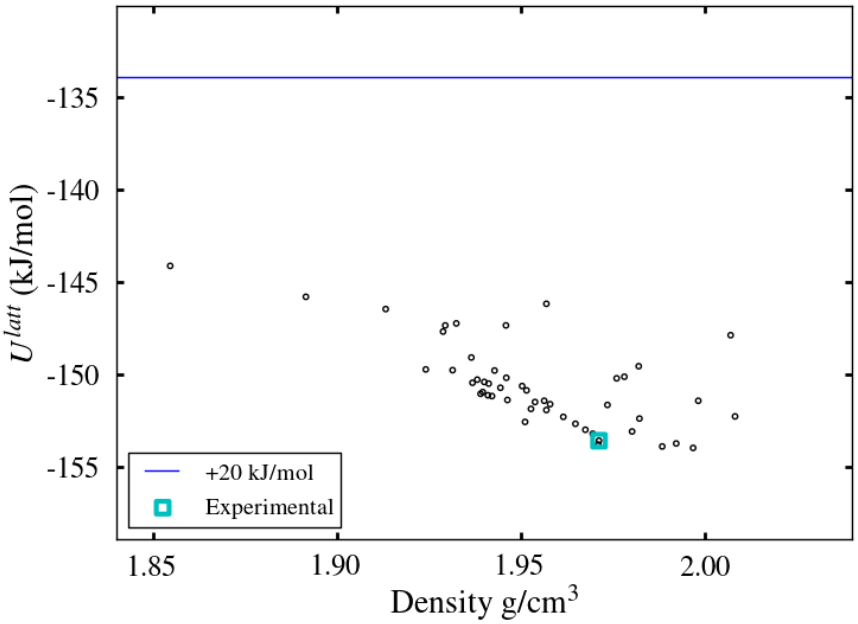

Figure 5.17: polymorphic landscape of sulflower, with each polymorph indicated by circle with position indicated by its density and lattice energy. Blue line indicates "stability threshold" under which a structure may feasibly be stable.

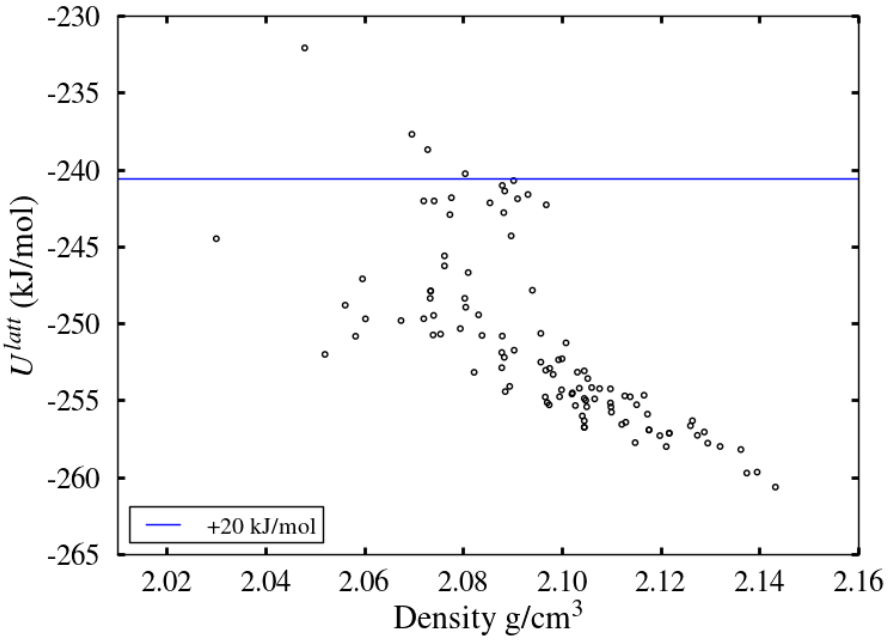

Figure 5.18: Polymorphic landscape of PSC with potential stability threshold marked.

the success in predicting the structure of sulflower, PSC was investigated using these methods (figure 5.18). The resulting structures all possess offset stacks of PSC molecules down the shortest (*b*) axis, with stacks held together via interactions between peripheral atoms on adjacent PSC molecules along the long (*c*) axis (figure 5.19). For nearest neighbouring molecules up the stacks, the separation and offset distances are 3.499 Å and

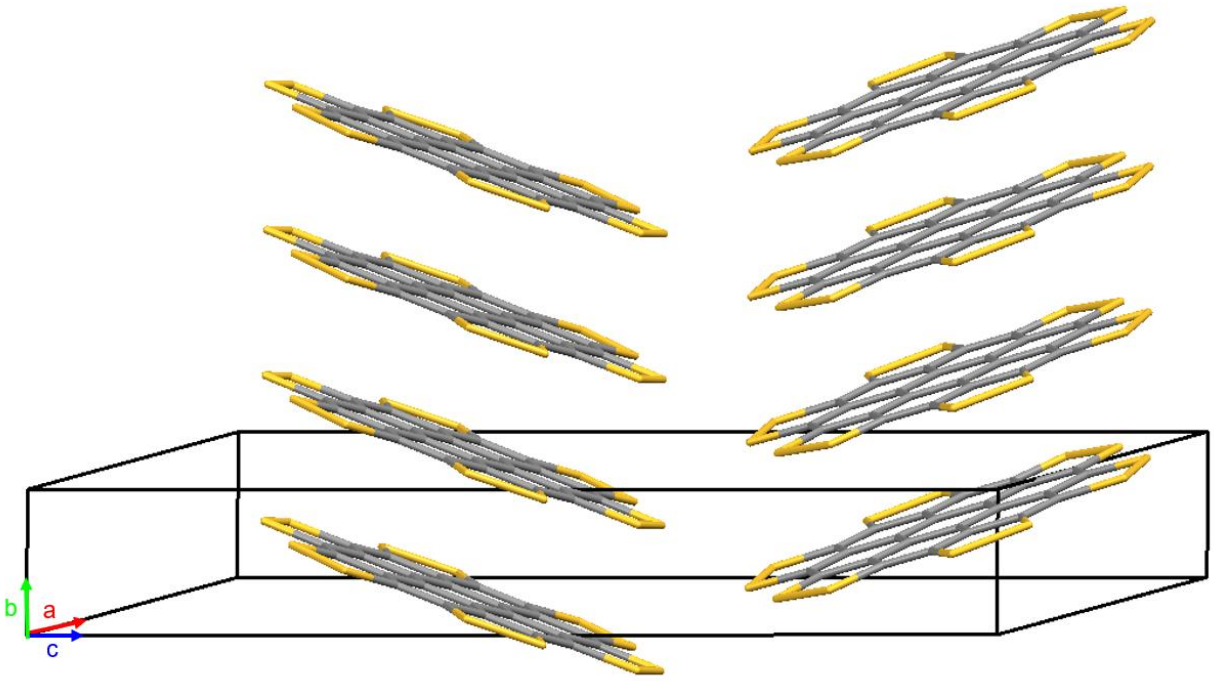

Figure 5.19: The most stable predicted crystal structure of PSC. Unit cell indicated by black lines, with additional molecules shown along the *b*-axis to demonstrate the offset stacking present in the structure.

1.253 Å respectively, matching closely to the values of 3.535 Å and 1.293 Å for offset dimers predicted in force-field calculations (table 5.2). The structure is extremely anisotropic, with a long-to-short axis ratio of 6.63 calculated from the lattice parameters of the unit cell (table 5.3), in comparison to sulflower's 4.26 and β-coronene's 4.50. The inter-stack interactions are long-distance and therefore appear to be far weaker than interactions along the stacks. Therefore, whilst the structures are potentially stable according to their calculated lattice energies, the formation of such structures would be highly unfeasible and would be unlikely to form under experimental growth conditions. Results from both the ORIENT simulations and the Gaussian potential landscape calculations would suggest that PSC molecules would show preference for direct face-face stacked formations, however this is at least highly uncommon (if not entirely absent) in the crystal structures of aromatic molecules[155], with any potential unit cells containing more than two direct-stacked aromatic molecules unable to be categorised into any of Desiraju and Gavezzotti's structure groups[137]. However, it may still be possible to induce crystallisation via methods which achieve high degrees of supersaturation over extended periods of time, which would allow for molecules to adopt kinetically stable conformations which could feasibly form a unit cell over a sufficient time that crystal growth occurred. Epitaxial growth may be another method with which to realise the theoretically predicted stable crystal structure of PSC, if a suitable substrate with similar lattice parameters is identified. Such structures formed from either of these methods may only be metastable though, given the weak inter-stack interactions.

Crystal system	Monoclinic
Space group	P c
a/Å	12.98
b/Å	3.71
c/Å	24.6
α/ Å	90
β/°	61.7
γ/°	90
Volume/Å^3	1043
Z	2

Table 5.3: Lattice parameters of the predicted most stable form of PSC.

5.4 Summary and Impact

In this chapter, crystal growth of persulfurated coronene was attempted via solvent growth, PVT under both ambient and vacuum conditions, and dropcasting, with each method resulting in either amorphous aggregates or disintegration of the molecule. DSC data on as-supplied PSC powder exhibited no crystallisation events over heating from -70 °C to 300 °C and cooling back to -70 °C at a rate of 10 °C per min. Electron diffraction data collected via TEM on raw PSC aggregates confirmed that they are amorphous, with no crystal domains at the nanoscale. DFT calculations reveal that the electrostatic potential map of PSC is broadly homogeneous with no strong permanent dipoles, making the kind of edge-face interactions seen in the crystal structures of other planar aromatic molecules at least highly unfavourable relative to direct cofacial stacking. This was further investigated with optimisations of two and three molecules, which revealed that the direct cofacial stacking conformation of PSC was more favourable than offset stacking. Furthermore, single-point energy calculations of PSC molecules in face-face and edge-face arrangements revealed that the face-face conformation is far more stable. CSP models predict that there are stable crystal structures of PSC formed of weakly linked offset molecular stacks, although it appears unlikely that such structures could be grown due to the anisotropy of the unit cell. The XRD pattern of raw PSC powder contains a broad peak at a 2θ value that corresponds to a d-spacing which matches closely with the calculated intermolecular separation of direct stacks of PSC molecules, meaning that such stacks are likely present in the aggregates.

This is the first reported PAM which does not follow the conventions of crystallisation proposed by Desiraju and Gavezzotti, due to its unique atomic arrangement resulting in an electronic distribution which does not facilitate one of the fundamental molecular interactions required for crystal formation. It may therefore provide an interesting model for further computational study and could aid in the design of molecules in which crystallisation is directed toward specific interactions, for example in liquid crystals in which face-face stacking is desired. Liquid crystals with aromatic cores have been shown to exhibit high carrier mobilities[156], however these molecules require the addition of bulky chains in order to force them to adopt the ideal conformation for charge transfer. Were a molecule to be found that could self-organise into such configurations and did not require bulky constituents, the density of stacks could be increased leading to greater charge mobilities of

aggregates if the columns can be arranged toward the same direction. Much research has also been done on molecular glasses which could potentially combine the processability and quick preparation of polymers with the ease of purification and the high carrier mobilities of single crystals. The encouragement of glass formation is usually achieved via the addition of bulky substituents to a base molecule[157], however the research in this chapter demonstrates that the prevention of crystallisation may also be achieved in smaller molecules if the molecular charge distribution is carefully considered.

6 Chapter 6: Conclusions and Future Work

The work presented in this thesis demonstrates how the crystallisation and optical properties of organic crystals may be related to the fundamental quantum behaviour of electrons through both experimental methods and computational simulations. The work contained in each of the results chapters and their associated publications elucidate previously unexplained phenomena within organic crystal systems and will help in developing crystals with desired optoelectronic properties for use in devices such as LEDs, solar cells and lasers. Furthermore, the research into predicting and realising different polymorphic forms could be applied more widely to areas such as pharmaceuticals and aggro-chemicals.

In chapter 3, crystals of the molecule Br-FN were grown for the first time via PVT, resulting in crystals of both the previously known polymorph (form 1) which had been formed from solution growth methods and a new, undocumented form which grew in higher temperature regions of the growth apparatus (form 2). Form 2 has a rod-like morphology, in comparison to the block-like morphology of form 1 crystals. Form 2 exhibits weaker, red-shifted fluorescence emission relative to form 1 owing to greater intermolecular π-π overlap and a conformation that enables conjugation over the entire molecular structure. DSC and lattice energy calculations indicated that form 2 is more thermodynamically stable than form 1, with no transitions between forms as the crystals are cooled or heated. Further crystal growth experiments in a three-zone furnace indicate that a higher temperature substrate was causing the more stable polymorph to grow, with this likely being due to the energy provided by the substrate to the crystal at high temperature causing it to overcome the potential barrier separating the two forms, therefore allowing relaxation to a more stable configuration. A more detailed analysis of the relationship between crystal structure and substrate temperature is necessary for a wide number of different molecules to achieve a full understanding of crystal growth from the vapour. This could be done using a setup in which the sample is vaporised and the temperature of the substrate on which the crystals grow is more precisely controlled, allowing for an exact determination of the temperature necessary to grow a particular structure. Such a setup could then be applied more widely to molecules with predicted crystal structures that are more thermodynamically stable than experimentally produced forms but that have not yet been realised. This growth technique could then potentially be a route toward growing these undocumented structures.

In chapter 4, the differences in fluorescence between the mineral karpatite and lab-grown coronene crystals was investigated. pXRD and recrystallisation experiments revealed both to be composed purely of coronene in the same γ-herringbone crystal structure. SEM showed stark differences in the micro-morphology of each, with karpatite having nano-thin crystalline layers and lab-grown crystals being needles several microns thick. The differences in optical behaviour were quantified via UV-Vis and fluorescence spectroscopy measurements, with lab-grown crystals being strongly excited by a wavelength of 460 nm and emitting at 500 nm, whereas karpatite is exclusively excited by wavelengths below below 430 nm and emits at 460 nm. The differences were attributed to the presence of excimers, excitons delocalised over two molecules, which emit at lower wavelengths to monomer excitons but are only formed in bulk crystals rather than thin flakes, resulting in red-shifted emission

for the thicker lab-grown crystals. This is the first reported instance of crystal morphology altering the optical behaviour of an organic crystal. Experiments to determine the optical properties of nano-thick coronene crystals must be carried out to confirm that the crystal thickness is influencing their fluorescence profiles. These could potentially be produced via PVT or deposition methods in which the thickness could be controlled more finely. Detailed simulations of excimer formation in coronene crystals would provide answers as to whether excimers would form if particular crystal planes are exposed, which could then be related to the surface of the layers present in karpatite. Crystals of similar molecules could also be investigated in a similar manner to determine whether the theories developed in this work could be applied more widely to elucidate unexplained optical phenomena in other systems such as tetracene and pyrene.

In chapter 5, crystallisation of the large planar aromatic molecule PSC was attempted via solvent growth, dropcasting, PVT in an open system and PVT in a vacuum. No crystals could be formed through any of these means, with pXRD on as-supplied powder showing it to be amorphous. 3D electron diffraction tomography showed that the powder had no crystallinity even at the nanoscale. DSC data collected from a temperature ramp from -70 to 300 °C and back to -70 °C exhibited no features associated with crystal formation. Computational methods were used to examine why PSC showed such reticence toward crystallisation, with the calculated electrostatic potential displaying a homogeneous distribution of charge across the entire molecule, which would not be conducive toward crystal formation as no edge-face intermolecular interactions could occur. Simulations of two and three molecule interactions predict that PSC would likely form into strongly bonded face-face stacks, confirmed with energy landscape calculations which demonstrated PSC's preference for face-face rather than edge-face stacking. Broad peaks in pXRD patterns of PSC powder suggest that molecular stacks are present within the material. CSP identified a number of potential stable crystal structures, all of which possess stacks similar to those predicted by multi-molecular optimisations. However, the extreme anisotropy of these structures renders them unlikely to be grown under standard experimental conditions. Nevertheless, the predicted structures may still be realised under conditions in which high degrees of supersaturation are sustained over long periods of time such as gel-based diffusion methods. Crystal could also possibly be grown epitaxially from a surface with similar lattice parameters to the predicted structures. Providing direct proof of the existence of the molecular stacks would be an important next step. This may be achieved via techniques such as atomic force microscopy or scanning tunnelling microscopy. If the stacks are proven to be stable, PSC (or a molecule with similar charge distribution) could potentially be used as the base of self-organising liquid crystal molecules with high charge carrier mobilities, an important property within the field of molecular electronics.

7 Bibliography

1. Podzorov V. Organic single crystals: Addressing the fundamentals of organic electronics. *MRS Bull*. 2013;38(01):15-24. doi:10.1557/mrs.2012.306

2. Forrest SR. The path to ubiquitous and low-cost organic electronic appliances on plastic. *Nature*. 2004;428(6986):911-918. doi:10.1038/nature02498

3. Desiraju GR. *The Crystal as a Supramolecular Entity*. Vol 2. Chichester: John Wiley & Sons, Ltd; 2007. doi:10.1002/9780470511459

4. Forget, Sébastien, Chénais S. *Organic Solid-State Lasers*. Atlanta: Springer; 2013. doi:10.1007/978-3-642-36705-2

5. Kelly A, Knowles KM. *Crystallography and Crystal Defects*. 2nd ed. Chichester: Wiley; 2012.

6. International Union of Crystallography. The 230 Space Groups. *Int Tables Crystallogr*. 2006;A(7.1):112-717. doi:10.1107/97809553602060000513

7. Ashcroft NW, Mermin ND. *Solid State Physics*. New York: Holt, Rinehart and Winston; 1976.

8. Atkins P, de Paula J. *Physical Chemistry for the Life Sciences*. W. H. Freeman Company; 2006.

9. Stone A. *The Theory of Intermolecular Forces*. Oxford University Press; 2013. doi:10.1093/acprof:oso/9780199672394.001.0001

10. Ewing GE. Intermolecular Interactions: van der Waals Molecules. *Angew Chemie Int Ed English*. 1972;11(6):486-495. doi:10.1002/anie.197204861

11. Vekilov PG. The two-step mechanism of nucleation of crystals in solution. *Nanoscale*. 2010;2(11):2346-2357. doi:10.1039/c0nr00628a

12. Frank FC. kinematic theory of crystal growth and dissolution processes. In: *Growth and Perfection of Crystals*. New York: Wiley; 1958:411-420.

13. Hwang J, Yan R, Oschatz M, Schmidt BVKJ. Solvent mediated morphology control of zinc MOFs as carbon templates for application in supercapacitors. *J Mater Chem A*. 2018;6(46):23521-23530. doi:10.1039/C8TA07700B

14. Stahly GP. Diversity in single- and multiple-component crystals. the search for and prevalence of polymorphs and cocrystals. *Cryst Growth Des*. 2007;7(6):1007-1026. doi:10.1021/cg060838j

15. Fox D, Labes MM, Weissberger A. *Physics and Chemistry of the Organic Solid State, Volume II*. First

Edit. New York: John Wiley & Sons, Ltd; 1965. https://www.biblio.com/book/physics-chemistry-organic-solid-state-volume/d/365428062. Accessed January 16, 2020.

16. Thomas SP, Spackman MA. The Polymorphs of ROY: A Computational Study of Lattice Energies and Conformational Energy Differences. *Aust J Chem*. 2018;71(4):279. doi:10.1071/CH17620

17. Abdul Mudalip SK, Abu Bakar MR, Jamal P, et al. Effects of Solvents on Polymorphism and Shape of Mefenamic Acid Crystals. Aljunid SA, Mohd Salleh MAA, Rashidi CBM, Soh PJ, Ku Azir KNF, eds. *MATEC Web Conf*. 2018;150:02004. doi:10.1051/matecconf/201815002004

18. Ostwald W. Studien über die Bildung und Umwandlung fester Körper. 1. Abhandlung: Übersättigung und Überkaltung. *Zeitschrift für Phys Chemie*. 1897;22:289-330.

19. Sun W, Ceder G. Induction time of a polymorphic transformation. *CrystEngComm*. 2017;19(31):4576-4585. doi:10.1039/c7ce00766c

20. Beckmann PA, Rablen PR, Schmink J, Szewczyk ST, Rheingold AL. Concomitant Polymorphism in an Organic Solid: Molecular and Crystal Structure and Intra- and Intermolecular Potential Contributions to *tert* -Butyl and Methyl Group Rotation. *ChemPhysChem*. 2019;20(21):2887-2894. doi:10.1002/cphc.201900436

21. Bonafede SJ, Ward MD. Selective Nucleation and Growth of an Organic Polymorph by Ledge-Directed Epitaxy on a Molecular Crystal Substrate. *J Am Chem Soc*. 1995;117(30):7853-7861. doi:10.1021/ja00135a001

22. Arlin JB, Price LS, Price SL, Florence AJ. A strategy for producing predicted polymorphs: Catemeric carbamazepine form v. *Chem Commun*. 2011;47(25):7074-7076. doi:10.1039/c1cc11634g

23. Parambil J V., Poornachary SK, Heng JYY, Tan RBH. Template-induced nucleation for controlling crystal polymorphism: From molecular mechanisms to applications in pharmaceutical processing. *CrystEngComm*. 2019;21(28):4122-4135. doi:10.1039/c9ce00404a

24. Červinka C, Beran GJO. Ab initio prediction of the polymorph phase diagram for crystalline methanol. *Chem Sci*. 2018;9(20):4622-4629. doi:10.1039/c8sc01237g

25. Noller C, Zumdahl S, Usselman M, Norman R. Chemical compound. In: *Encyclopaedia Brittanica*. ; 1999. https://www.britannica.com/science/chemical-compound.

26. Meunier M, Quirke N. Molecular modeling of electron trapping in polymer insulators. *J Chem Phys*. 2000;113(1):369-376. doi:10.1063/1.481802

27. Ouellette RJ, Rawn JD. *Organic Chemistry: Structure, Mechanism, Synthesis*. Cambridge: Academic Press; 2019.

28. Petty MC. *Molecular Electronics : From Principles to Practice*. Chichester: John Wiley & Sons, Ltd; 2007.

29. Varughese S. Non-covalent routes to tune the optical properties of molecular materials. *J Mater Chem C*. 2014;2(18):3499. doi:10.1039/c3tc32414a

30. Katoh R, Katoh S, Furube A, Tokumaru K, Kotani M. Fluorescence quantum yield of aromatic hydrocarbon crystals. *J Phys Chem C*. 2009;113(7):2961-2965. doi:10.1021/jp807684m

31. Siliņš E. *Organic Molecular Crystals: Their Electronic States*. Berlin: Springer-Verlag; 1980.

32. Hong Y, Lam JWY, Tang BZ. Aggregation-induced emission. *Chem Soc Rev*. 2011;40(11):5361. doi:10.1039/c1cs15113d

33. Benz K-W, Neumann W. *Introduction to Crystal Growth and Characterization*. New York: Wiley; 2014.

34. Reese C, Bao Z. Organic single-crystal field-effect transistors. *Mater Today*. 2007;10(3):20-27. doi:10.1016/S1369-7021(07)70016-0

35. Jiang H, Kloc C. Single-crystal growth of organic semiconductors. *MRS Bull*. 2013;38(01):28-33. doi:10.1557/mrs.2012.308

36. Giacovazzo C, International Union of Crystallography. *Fundamentals of Crystallography*. 3rd ed. Oxford: Oxford University Press; 2011.

37. Rohrer GS. *Structure and Bonding in Crystalline Materials*. Cambridge: Cambridge University Press; 2001.

38. Glazer AM. *Crystallography : A Very Short Introduction*. Oxford: Oxford University Press; 2016.

39. Altomare A, Camalli M, Cuocci C, Giacovazzo C, Moliterni A, Rizzi R. EXPO2009: Structure solution by powder data in direct and reciprocal space. *J Appl Crystallogr*. 2009;42(6):1197-1202. doi:10.1107/S0021889809042915

40. Gemmi M, Mugnaioli E, Gorelik TE, et al. 3D electron diffraction: The nanocrystallography revolution. *ACS Cent Sci*. 2019;5(8):1315-1329. doi:10.1021/acscentsci.9b00394

41. Russ JC. *Fundamentals of Energy Dispersive X-Ray Analysis*. London: Butterworths; 1984.

42. Sommer L. *Analytical Absorption Spectrophotometry in the Visible and Ultraviolet : The Principles*. Amsterdam: Elsevier; 1989.

43. Kubelka P. Ein Beitrag zur Optik der Farbanstriche. *Zeitschrift fur Tech Phys*. 1931;12:593-601.

44. Sedgwick AC, Wu L, Han HH, et al. Excited-state intramolecular proton-transfer (ESIPT) based

fluorescence sensors and imaging agents. *Chem Soc Rev*. 2018;47(23):8842-8880. doi:10.1039/c8cs00185e

45. Tissue BM. Ultraviolet and Visible Absorption Spectroscopy. In: *Characterization of Materials*. Hoboken, NJ, USA: John Wiley & Sons, Inc.; 2012:1-13. doi:10.1002/0471266965.com059.pub2

46. Perrenot B, Widmann G. Polymorphism by differential scanning calorimetry. *Thermochim Acta*. 1994;234(C):31-39. doi:10.1016/0040-6031(94)85133-6

47. Thornton PR. *Scanning Electron Microscopy: Applications to Materials and Device Science*. London: Chapman & Hill; 1968.

48. Kohn W, Sham LJ. Self-consistent equations including exchange and correlation effects. *Phys Rev*. 1965;140(4A):A1133. doi:10.1103/PhysRev.140.A1133

49. Fuller J, Fortunelli A, Goddard WA, An Q. Reaction mechanism and kinetics for ammonia synthesis on the Fe(211) reconstructed surface. *Phys Chem Chem Phys*. 2019;21(21):11444-11454. doi:10.1039/c9cp01611b

50. Militzer B, Hubbard WB, Vorberger J, Tamblyn I, Bonev SA. *A Massive Core in Jupiter Predicted From First-Principles Simulations*.

51. St.-Amant A, Cornell WD, Kollman PA, Halgren TA. Calculation of molecular geometries, relative conformational energies, dipole moments, and molecular electrostatic potential fitted charges of small organic molecules of biochemical interest by density functional theory. *J Comput Chem*. 1995;16(12):1483-1506. doi:10.1002/jcc.540161206

52. Salzillo T, Della Valle RG, Venuti E, et al. Two new polymorphs of the organic semiconductor 9,10-diphenylanthracene: Raman and X-ray analysis. *J Phys Chem C*. 2016;120(3):1831-1840. doi:10.1021/acs.jpcc.5b11115

53. Murray JS, Politzer P. The electrostatic potential: an overview. *Wiley Interdiscip Rev Comput Mol Sci*. 2011;1(2):153-163. doi:10.1002/wcms.19

54. Cox EG. The Crystalline Structure of Benzene. *Proc R Soc London Ser A, Contain Pap a Math Phys Character*. 1932;135:491-498.

55. Zhao Y, Truhlar DG. A Prototype for graphene material simulation: Structures and interaction potentials of coronene dimers. *J Phys Chem C*. 2008. doi:10.1021/jp710918f

56. Price SL. The computational prediction of pharmaceutical crystal structures and polymorphism. *Adv Drug Deliv Rev*. 2004;56(3):301-319. doi:10.1016/j.addr.2003.10.006

57. Stone AJ. Distributed polarizabilities. *Mol Phys*. 1985;56(5):1065-1082.

doi:10.1080/00268978500102901

58. Yeh HC, Wu WC, Wen YS, Dai DC, Wang JK, Chen CT. Derivative of α,β-dicyanostilbene: Convenient precursor for the synthesis of diphenylmaleimide compounds, E-Z isomerization, crystal structure, and solid-state fluorescence. *J Org Chem*. 2004;69(19):6455-6462. doi:10.1021/jo049512c

59. Dong R, Pfeffermann M, Skidin D, et al. Persulfurated Coronene: A New Generation of "Sulflower." *J Am Chem Soc*. 2017;139(6):2168-2171. doi:10.1021/jacs.6b12630

60. Sheldrick GM. A short history of SHELX. *Acta Crystallogr Sect A Found Crystallogr*. 2007;64(1):112-122. doi:10.1107/S0108767307043930

61. Dolomanov O V., Bourhis LJ, Gildea RJ, Howard JAK, Puschmann H. OLEX2: A complete structure solution, refinement and analysis program. *J Appl Crystallogr*. 2009;42(2):339-341. doi:10.1107/S0021889808042726

62. Dovesi R, Orlando R, Erba A, et al. CRYSTAL14 : A program for the ab initio investigation of crystalline solids. *Int J Quantum Chem*. 2014;114(19):1287-1317. doi:10.1002/qua.24658

63. Brandenburg JG, Caldeweyher E, Grimme S, et al. Screened exchange hybrid density functional for accurate and efficient structures and interaction energies. *Phys Chem Chem Phys*. 2016;18(23):15519-15523. doi:10.1039/C6CP01697A

64. Frisch, M. J.; Trucks, G. W.; Schlegel, H. B.; Scuseria, G. E.; Robb, M. A.; Cheeseman, J. R.; Scalmani, G.; Barone, V.; Petersson, G. A.; Nakatsuji, H.; Li, X.; Caricato, M.; Marenich, A. V.; Bloino, J.; Janesko, B. G.; Gomperts, R.; Mennucci, B.; Hratch 2016. Gaussian 16, Revision C.01. 2016.

65. Habgood M, Sugden IJ, Kazantsev A V., Adjiman CS, Pantelides CC. Efficient handling of molecular flexibility in ab initio generation of crystal structures. *J Chem Theory Comput*. 2015;11(4):1957-1969. doi:10.1021/ct500621v

66. Williams DE, Cox SR. Nonbonded potentials for azahydrocarbons: the importance of the Coulombic interaction. *Acta Crystallogr Sect B*. 1984;40(4):404-417. doi:10.1107/S010876818400238X

67. UCL Chemistry Department. Control and Prediction of the Organic Solid State. http://www.chem.ucl.ac.uk/cposs/index.htm. Published 2004. Accessed March 12, 2020.

68. Price SL, Leslie M, Welch GWA, et al. Modelling organic crystal structures using distributed multipole and polarizability-based model intermolecular potentials. *Phys Chem Chem Phys*. 2010;12(30):8478-8490. doi:10.1039/c004164e

69. Jensen TT, Potticary J, Terry LR, Bruce Macdonald HE, Brandenburg JG, Hall SR. Polymorphism in crystals of bis(4-bromophenyl)fumaronitrile through vapour phase growth. *CrystEngComm*.

2017;19(48):7223-7228. doi:10.1039/C7CE01543G

70. Karl N. Growth and electrical properties of high purity organic molecular crystals. *J Cryst Growth*. 1990;99(1-4):1009-1016. doi:10.1016/S0022-0248(08)80072-3

71. Lee T, Chang SC. Sublimation Point Depression of Small-Molecule Semiconductors by Sonocrystallization. *Cryst Growth Des*. 2009;9(6):2674-2684. doi:10.1021/cg801305r

72. Liu Z, Zhong L, Ying P, Feng Z, Li C. Crystallization of metastable β glycine from gas phase via the sublimation of α or γ form in vacuum. *Biophys Chem*. 2008;132(1):18-22. doi:10.1016/j.bpc.2007.10.003

73. Saeki A, Seki S, Takenobu T, Iwasa Y, Tagawa S. Mobility and Dynamics of Charge Carriers in Rubrene Single Crystals Studied by Flash-Photolysis Microwave Conductivity and Optical Spectroscopy. *Adv Mater*. 2008;20(5):920-923. doi:10.1002/adma.200702463

74. Zhang P, Zeng X, Deng J, et al. Growth mechanism of large-size rubrene single crystals grown by a solution technique. *Jpn J Appl Phys*. 2010;49(9 PART 1). doi:10.1143/JJAP.49.095501

75. Stevens LA, Goetz KP, Fonari A, et al. Temperature-mediated polymorphism in molecular crystals: The impact on crystal packing and charge transport. *Chem Mater*. 2015;27(1):112-118. doi:10.1021/cm503439r

76. Laudise R., Kloc C, Simpkins P., Siegrist T. Physical vapor growth of organic semiconductors. *J Cryst Growth*. 1998;187(3-4):449-454. doi:10.1016/S0022-0248(98)00034-7

77. Wang H, Zhao Y, Xie Z, Wang H, Wang B, Ma Y. The thermodynamic characteristics of organic crystal growth by physical vapor transport: towards high-quality and color-tunable crystal preparation. *CrystEngComm*. 2014;16(21):4539-4545. doi:10.1039/C3CE42367K

78. Pieniazek PA, Krylov AI, Bradforth SE. Electronic structure of the benzene dimer cation. *J Chem Phys*. 2007;127(4). doi:10.1063/1.2749506

79. Han X, Bai Q, Yao L, et al. Highly Efficient Solid-State Near-Infrared Emitting Material Based on Triphenylamine and Diphenylfumaronitrile with an EQE of 2.58% in Nondoped Organic Light-Emitting Diode. *Adv Funct Mater*. 2015;25(48):7521-7529. doi:10.1002/adfm.201503344

80. Perdew JP, Burke K, Ernzerhof M. Generalized Gradient Approximation Made Simple. *Phys Rev Lett*. 1996;77(18):3865-3868. doi:10.1103/PhysRevLett.77.3865

81. Grimme S, Antony J, Ehrlich S, Krieg H. A consistent and accurate *ab initio* parametrization of density functional dispersion correction (DFT-D) for the 94 elements H-Pu. *J Chem Phys*. 2010;132(15):154104. doi:10.1063/1.3382344

82. Kresse G, Furthmüller J. Efficiency of ab-initio total energy calculations for metals and semiconductors using a plane-wave basis set. *Comput Mater Sci*. 1996;6(1):15-50. doi:10.1016/0927-0256(96)00008-0

83. Hartman P, Perdok WG. An interpretation of the law of donnay and harker. *Am Mineral*. 1956;41(5-6):449-459.

84. Bravais A. *Études Crystallographiques*. Paris: Academie des Sciences; 1913.

85. Donnay JDH, Harker D. A new law of crystal morphology extending the Law of Bravais. *Am Mineral*. 1937;22(5):446-467.

86. Schneider JA, Black H, Lin HP, Perepichka DF. Polymorphism in new thienothiophene-thiazolothiazole organic semiconductors. *ChemPhysChem*. 2015;16(6):1173-1178. doi:10.1002/cphc.201500066

87. Wang H, Zhao Y, Xie Z, Wang H, Wang B, Ma Y. The thermodynamic characteristics of organic crystal growth by physical vapor transport: towards high-quality and color-tunable crystal preparation. *CrystEngComm*. 2014;16(21):4539-4545. doi:10.1039/C3CE42367K

88. Shen S, Xia G, Jiang Z, Shao Q, Shan W, Wang H. Temperature Controlling Polymorphism and Polymorphic Interconversion in Sublimation Crystallization of 5-Methoxy-salicylaldhyde Azine. *Cryst Growth Des*. 2019;19(1):320-327. doi:10.1021/acs.cgd.8b01429

89. Lee EH. A practical guide to pharmaceutical polymorph screening & selection. *Asian J Pharm Sci*. 2014;9(4):163-175. doi:10.1016/j.ajps.2014.05.002

90. Potticary J, Jensen TT, Hall SR. Nanostructural origin of blue fluorescence in the mineral karpatite. *Sci Rep*. 2017;7(1):9867. doi:10.1038/s41598-017-10261-w

91. Echigo T, Kimata M, Maruoka T. Crystal-chemical and carbon-isotopic characteristics of karpatite (C24H12) from the Picacho Peak Area, San Benito County, California: Evidences for the hydrothermal formation. *Am Mineral*. 2007;92(8-9):1262-1269. doi:10.2138/am.2007.2509

92. Matsui AH, Mizuno K. Crystallization and excitonic luminescence of coronene crystals. *J Phys D Appl Phys*. 1999;26(8B):B242-B244. doi:10.1088/0022-3727/26/8B/042

93. Hayashi S, Koizumi T. Direction-specific fluorescence of an engineered organic crystal and the appearance of a new face caused by mechanically induced shaping. *CrystEngComm*. 2019;21(40):5990-5994. doi:10.1039/c9ce01002e

94. Dobrowolski MA, Ciesielski A, Cyrański MK. On the aromatic stabilization of corannulene and coronene. *Phys Chem Chem Phys*. 2011;13(46):20557-20563. doi:10.1039/c1cp21994d

95. Shen G, Chen Y, Wei S, et al. Can Coronene and/or Benzo(a)pyrene/Coronene ratio act as unique markers for vehicle emission? *Environ Pollut*. 2014. doi:10.1016/j.envpol.2013.08.020

96. National Research Council. *Polycyclic Aromatic Hydrocarbons: Evaluation of Sources and Effects*. Washington, DC: The National Academies Press; 1983.

97. van Dijk JTM, Hartwijk A, Bleeker AC, Lugtenburg J, Cornelisse J. Gram Scale Synthesis of Benzo[*ghi*]perylene and Coronene †. *J Org Chem*. 1996;61(3):1136-1139. doi:10.1021/jo951555t

98. Potticary J, Terry LR, Bell C, et al. An unforeseen polymorph of coronene by the application of magnetic fields during crystal growth. *Nat Commun*. 2016;7(May):11555. doi:10.1038/ncomms11555

99. Itoh T. Fluorescence and phosphorescence from higher excited states of organic molecules. *Chem Rev*. 2012;112(8):4541-4568. doi:10.1021/cr200166m

100. Desiraju GR, Gavezzotti A. Crystal structures of polynuclear aromatic hydrocarbons. Classification, rationalization and prediction from molecular structure. *Acta Crystallogr Sect B*. 1989;45(5):473-482. doi:10.1107/S0108768189003794

101. Potticary J, Boston R, Vella-Zarb L, Few A, Bell C, Hall SR. Low temperature magneto-morphological characterisation of coronene and the resolution of previously observed unexplained phenomena. *Sci Rep*. 2016. doi:10.1038/srep38696

102. Echigo T, Kimata M, Maruoka T. Crystal-chemical and carbon-isotopic characteristics of karpatite (C24H12) from the Picacho Peak Area, San Benito County, California: Evidences for the hydrothermal formation. *Am Mineral*. 2007;92(8-9). http://ammin.geoscienceworld.org/content/92/8-9/1262. Accessed May 31, 2017.

103. Jahns RH, Lancaster FW. *Physical Characteristics of Commercial Sheet Muscovite in the Southeastern United States*. Washington DC: United States Government Printing Office; 1950.

104. Anthony JW, Bideaux RA, Bladh KW, Nichols MC. *Handbook of Mineralogy*. Washington DC: Mineral Data Publishing; 2003.

105. Chen ECM, Wentworth WE. A comparison of experimental determinations of electron affinities of pi charge transfer complex acceptors. *J Chem Phys J Chem Phys J Chem Physics464913 Hydrocarb J Chem Phys J Chem Phys*. 1975;63(71):1184-1506. doi:10.1063/1.438420

106. Fetzer JC. The chemistry and analysis of large PAHs. *Polycycl Aromat Compd*. 2007;27(2):143-162. doi:10.1080/10406630701268255

107. Matsui AH, Mizuno KI. Crystallization and Excitonic Luminescence of Coronene Crystals. *J Phys D Appl Phys*. 1993;26(8):B242-B244. doi:10.1088/0022-3727/26/8B/042

108. Yamamoto T, Nakatani S, Nakamura T. Exciton - phonon coupling and pressure-induced structural phase changes in coronene crystals. *Chem Phys*. 1994;184:247-254. http://www.sciencedirect.com/science/article/pii/0301010494000840.

109. Williams RT, Song KS. The self-trapped exciton. *J Phys Chem Solids*. 1990;51(7):679-716. doi:10.1016/0022-3697(90)90144-5

110. Matsui AH. Excitonic processes in aromatic molecular crystals of strong exciton-phonon coupling. *Pure Appl Chem*. 1995;67(3):429-436. doi:10.1351/pac199567030429

111. Mizuno K ichi, Matsui A. Quantum confinement of translational motion of excitons in α-perylene and pyrene microcrystals. *Mol Cryst Liq Cryst Sci Technol Sect A Mol Cryst Liq Cryst*. 1992;218(1):49-54. doi:10.1080/10587259208047014

112. Yoshikawa H, Sasaki K, Masuhara H. Near-field fluorescence microspectroscopy of tetracene microcrystals. *Mol Cryst Liq Cryst Sci Technol Sect A Mol Cryst Liq Cryst*. 1998;314:203-208. doi:10.1080/10587259808042479

113. Jursenas S, Gruodis a., Kodis G, et al. Free and Self-Trapped Charge-Transfer Excitons in Crystals of Dipolar Molecules of N , N -Dimethylaminobenzylidene 1,3-Indandione. *J Phys Chem B*. 1998;102(7):1086-1094. doi:10.1021/jp971991e

114. Takazawa K, Inoue JI, Mitsuishi K. Self-assembled coronene nanofibers: Optical waveguide effect and magnetic alignment. *Nanoscale*. 2014;6(8):4174-4181. doi:10.1039/c3nr06760b

115. Wang H, Xu X-H, Ji H-F. Nano/microwires of coronene for sensing electron-deficient aromatics. *Nanotechnol Dev*. 2011;2(1):1. doi:10.4081/nd.2012.e1

116. Kajiwara T, Ohno K, Iwashima S, Inokuchi H. Fluorescence Spectra of High-purity Coronene Thin Film. *Bull Chem Soc Jpn*. 1969;42(9):2734-2734. doi:10.1246/bcsj.42.2734

117. Seko T, Ogura K, Kawakami Y, Sugino H, Toyotama H, Tanaka J. Excimer emission of anthracene, perylene, coronene and pyrene microcrystals dispersed in water. *Chem Phys Lett*. 1998;291(3-4):438-444. doi:10.1016/S0009-2614(98)00629-0

118. Kosugi T, Miyake T, Ishibashi S, Arita R, Aoki H. Ab initio electronic structure of solid coronene: Differences from and commonalities to picene. *Phys Rev B - Condens Matter Mater Phys*. 2011;84(2):020507. doi:10.1103/PhysRevB.84.020507

119. Gao Y, Liu H, Zhang S, et al. Excimer formation and evolution of excited state properties in discrete dimeric stacking of an anthracene derivative: A computational investigation. *Phys Chem Chem Phys*. 2018;20(17):12129-12137. doi:10.1039/c8cp00834e

120. Hoche J, Schmitt HC, Humeniuk A, Fischer I, Mitrić R, Röhr MIS. The mechanism of excimer

formation: An experimental and theoretical study on the pyrene dimer. *Phys Chem Chem Phys*. 2017;19(36):25002-25015. doi:10.1039/c7cp03990e

121. Jensen TT, Hall CL, Potticary J, Andrusenko I, Gemmi M, Hall SR. An experimental and computational study into the crystallisation propensity of 2nd generation sulflower. *Chem Commun*. 2019. doi:10.1039/C9CC08346D

122. Karadakov PB. Do large polycyclic aromatic hydrocarbons and graphene bend? How popular theoretical methods complicate finding the answer to this question. *Chem Phys Lett*. 2016;646:190-196. doi:10.1016/j.cplett.2015.12.068

123. Marinov NM, Pitz WJ, Westbrook CK, Castaldi MJ, Senkan SM. Modeling of aromatic and polycyclic aromatic hydrocarbon formation in premixed methane and ethane flames. *Combust Sci Technol*. 1996;116-117(1-6):211-287. doi:10.1080/00102209608935550

124. Hückel E. Quantentheoretische Beiträge zum Benzolproblem - I. Die Elektronenkonfiguration des Benzols und verwandter Verbindungen. *Zeitschrift für Phys*. 1931;70(3-4):204-286. doi:10.1007/BF01339530

125. Cohen R, Stokbro K, Martin JML, Ratner MA. Charge transport in conjugated aromatic molecular junctions: Molecular conjugation and molecule-electrode coupling. *J Phys Chem C*. 2007;111(40):14893-14902. doi:10.1021/jp0795309

126. Wöhrle T, Wurzbach I, Kirres J, et al. Discotic Liquid Crystals. *Chem Rev*. 2016;116(3):1139-1241. doi:10.1021/acs.chemrev.5b00190

127. Yu L. Polymorphism in molecular solids: An extraordinary system of red, orange, and yellow crystals. *Acc Chem Res*. 2010;43(9):1257-1266. doi:10.1021/ar100040r

128. Wheeler SE, Bloom JWG. Toward a more complete understanding of noncovalent interactions involving aromatic rings. *J Phys Chem A*. 2014;118(32):6133-6147. doi:10.1021/jp504415p

129. Pozo I, Majzik Z, Pavliček N, et al. Revisiting Kekulene: Synthesis and Single-Molecule Imaging. *J Am Chem Soc*. 2019;141(39):15488-15493. doi:10.1021/jacs.9b07926

130. Poater J, Solà M. Open-shell spherical aromaticity: The 2N2 + 2N + 1 (with S = N + 1/2) rule. *Chem Commun*. 2011;47(42):11647-11649. doi:10.1039/c1cc14958j

131. Cardia R, Malloci G, Serra G, Bosin A, Cappellini G. Electronic and optical properties of functionalized polyaromatic hydrocarbons: a computational investigation on perfluorinated circumacenes. In: Cheyns D, Beaujuge PM, van Elsbergen V, Ribierre J-C, eds. ; 2016:98950D. doi:10.1117/12.2229744

132. Tucker SA, Griffin JM, Acree WE, et al. Effect that Various Electron Donating and Electron

Withdrawing Functional Groups have Regarding Nitromethane's Ability to Selectively Quench Fluorescence Emission of Alternant Polycyclic Aromatic Hydrocarbons. *Polycycl Aromat Compd*. 1994;4(3):141-160. doi:10.1080/10406639408014699

133. Jose KVJ, van Eijck BP, Pal R, et al. Towards crystal structure prediction of complex organic compounds – a report on the fifth blind test. *Acta Crystallogr Sect B Struct Sci*. 2011;67(6):535-551. doi:10.1107/s0108768111042868

134. Desiraju GR, Gavezzotti A. From molecular to crystal structure; polynuclear aromatic hydrocarbons. *J Chem Soc Chem Commun*. 1989;(10):621. doi:10.1039/c39890000621

135. Gavezzotti A. Are Crystal Structures Predictable? *Acc Chem Res*. 1994;27(10):309-314. doi:10.1021/ar00046a004

136. Price SL. Predicting crystal structures of organic compounds. *Chem Soc Rev*. 2014;43(7):2098-2111. doi:10.1039/c3cs60279f

137. Desiraju GR, Gavezzotti A, IUCr. Crystal structures of polynuclear aromatic hydrocarbons. Classification, rationalization and prediction from molecular structure. *Acta Crystallogr Sect B Struct Sci*. 1989;45(5):473-482. doi:10.1107/S0108768189003794

138. Gerkin RE, Reppart WJ. The structure of carbazole at 168 K. *Acta Crystallogr Sect C Cryst Struct Commun*. 1986;42(4):480-482. doi:10.1107/S0108270186095720

139. Yamazaki D, Nishinaga T, Komatsu K. Radical Cation of Dibenzothiophene Fully Annelated with Bicyclo[2.2.2]octene Units: X-ray Crystal Structure and Electronic Properties. *Org Lett*. 2007. doi:10.1021/ol0483605

140. Süsse P, Steins M, Kupcik V. Indigo: Crystal structure refinement based on synchrotron data. *Zeitschrift für Krist - Cryst Mater*. 1988;184(1-4). doi:10.1524/zkri.1988.184.14.269

141. Zhang X, Côté AP, Matzger AJ. Synthesis and structure of fused α-oligothiophenes with up to seven rings. *J Am Chem Soc*. 2005. doi:10.1021/ja053326m

142. Li L, Zhao S, Li B, et al. From Saddle-Shaped to Planar Cyclic Oligothienoacenes: Stepped-Cyclization and Their Applications in OFETs. *Org Lett*. 2018. doi:10.1021/acs.orglett.8b00482

143. Chernichenko KY, Sumerin V V., Shpanchenko R V., Balenkova ES, Nenajdenko VG. "Sulflower": A New Form of Carbon Sulfide. *Angew Chemie*. 2006;118(44):7527-7530. doi:10.1002/ange.200602190

144. Wicker JGP, Cooper RI. Will it crystallise? Predicting crystallinity of molecular materials. *CrystEngComm*. 2015;17(9):1927-1934. doi:10.1039/C4CE01912A

145. Tan YZ, Yang B, Parvez K, et al. Atomically precise edge chlorination of nanographenes and its

application in graphene nanoribbons. *Nat Commun*. 2013;4. doi:10.1038/ncomms3646

146. Li J, Liu Y, Qian Y, et al. Describing curved-planar π-π Interactions: Modeled by corannulene, pyrene and coronene. *Phys Chem Chem Phys*. 2013;15(30):12694-12701. doi:10.1039/c3cp51095f

147. Hirayama S, Sakai H, Araki Y, et al. Systematic control of the excited-state dynamics and carrier-transport properties of functionalized benzo[ghi]perylene and coronene derivatives. *Chem - A Eur J*. 2014;20(29):9081-9093. doi:10.1002/chem.201304679

148. Sancho-García JC, Pérez-Jiménez AJ. Theoretical study of stability and charge-transport properties of coronene molecule and some of its halogenated derivatives: A path to ambipolar organic-based materials? *J Chem Phys*. 2014. doi:10.1063/1.4897205

149. Gingras M, Raimundo J-M, Chabre YM. Persulfurated Aromatic Compounds. *Angew Chemie Int Ed*. 2006;45(11):1686-1712. doi:10.1002/anie.200500032

150. Andrusenko I, Hamilton V, Mugnaioli E, et al. The Crystal Structure of Orthocetamol Solved by 3D Electron Diffraction. *Angew Chemie*. 2019;131(32):11035-11038. doi:10.1002/ange.201904564

151. Borisenko E. *Crystallization and Materials Science of Modern Artificial and Natural Crystals*. Moscow: IntechOpen; 2012.

152. Cozzi F, Siegel JS. Interaction between stacked aryl groups in 1,8-diarylnaphthalenes: Dominance of polar/π over charge-transfer effects. *Pure Appl Chem*. 2007;67(5):683-689. doi:10.1351/pac199567050683

153. Stone, A. J., Dullweber, A., Engkvist, O., Fraschini, E., Hodges, M. P., Meredith, A. W., Nutt DR, Popelier, P. L. A., Wales DJ. Orient: a program for studying interactions between molecules, version 5.0. 2018.

154. Obolensky OI, Semenikhina V V., Solov'yov A V., Greiner W. Interplay of electrostatic and van der Waals forces in coronene dimer. *Int J Quantum Chem*. 2007;107(6):1335-1343. doi:10.1002/qua.21253

155. Sinnokrot MO, Sherrill CD. High-accuracy quantum mechanical studies of π-π interactions in benzene dimers. *J Phys Chem A*. 2006;110(37):10656-10668. doi:10.1021/jp0610416

156. Feng X, Marcon V, Pisula W, et al. Towards high charge-carrier mobilities by rational design of the shape and periphery of discotics. *Nat Mater*. 2009;8(5):421-426. doi:10.1038/nmat2427

157. Strohriegl P, Grazulevicius JV. Charge-Transporting Molecular Glasses. *Adv Mater*. 2002;14(20):1439-1452. doi:10.1002/1521-4095(20021016)14:20<1439::AID-ADMA1439>3.0.CO;2-H